A CubeSat Docking Module Prototype

by

Robert James Waller

Thesis presented in partial fulfilment of the requirements for the degree of Master of Engineering (Electrical and Electronic) in the Faculty of Engineering at Stellenbosch University

Supervisor: Dr. L. Visagie

April 2022

Declaration

By submitting this thesis electronically, I declare that the entirety of the work contained therein is my own, original work, that I am the sole author thereof (save to the extent explicitly otherwise stated), that reproduction and publication thereof by Stellenbosch University will not infringe any third party rights and that I have not previously in its entirety or in part submitted it for obtaining any qualification.

Date: ..... April 2022. .....

Publications

Parts of the work done in thesis have been accepted by Control Conference Africa 2021 (CCA2021) for publication.

R. J. Waller and L. Visagie, "Pose Estimation for Cubesat Docking," *IFAC-PapersOnLine*, vol. 54, no.21, pp. 216-221, 2021, Control Conference Africa CCA 2021. [1]

Abstract

A CubeSat Docking Module Prototype

R.J. Waller

Department of Electrical and Electronic Engineering,
University of Stellenbosch,
Private Bag X1, Matieland 7602, South Africa.

Thesis: MEng (EE)

April 2022

The ability to dock cubesats on orbit opens up a large range of possibilities for mission designers and planners. This thesis describes the development of parts of a cubesat sized docking module. Specifically, t he p ose e stimation system and docking interface.

The pose estimation system was designed using a camera and marker system. The software of the system included blob detection, distortion correction and pose calculations. The individual elements of the system were tested followed by a full system test. The system was found to be relatively accurate, however, when the marker was not in the image centre, the accuracy of the system decreased massively.

The design of the docking interface included the investigation of 3 different concept mechanisms. Two of the three mechanism were pursued to a docking module concept phase and one of these was then prototyped. It was found that the prototype showed promised in terms of the docking ability and provided many insights into its manufacturability.

The feasibility of the two system as space-ready solutions was investigated. The systems were found to not require major changes to convert them to space-ready options.

The complete system seems to show much promise for a docking module however more development is required to find a complete s olution. A few suggestions were made into what needs to be done and some recommendations about improvements to the system were made.

Uittreksel

A CubeSat Docking Module Prototype

("A CubeSat Docking Module Prototype")

R.J. Waller

Departement Elektries en Elektroniese Ingenieurswese,
Universiteit van Stellenbosch,
Privaatsak X1, Matieland 7602, Suid Afrika.

Tesis: MIng (EE)

April 2022

Die vermoë om twee Cubesats in-vlug te koppel aan mekaar maak 'n reeks toepassings beskikbaar wat vantevore nie moontlik was nie. Hierdie proefskrif beskryf die ontwikkeling van 'n prototipe cubesat koppelingsmodule. Daar word spesifiek g efokus o p d ie o rientasie a fskatting e n m eganiese koppelvlak elemente.

Die orientasie afskattingsstelsel maak gebruik van 'n kamera met 'n merker op die teiken. Die sagteware wat dit instaatstel identifiseer helder kolle op die kamera beeld, pas distorsie korreksie toe en bereken dan die orientasie van die teiken relatief tot die kamera. Die elemente van hierdie substelsel is afsonderlik getoets, gevolg deur 'n volledige toets van die orientasie afskattingstelsel. Die orientasie afskatting toon genoegsame akkuraatheid, maar groter foute kom voor wanneer die teiken ver van die middel van die beeld voorkom.

Die ontwerp van die meganiese koppelvlak het behels om drie verskillende konsepte te ondersoek. Twee van hierdie konsepte is verder geanaliseer, en slegs 'n enkele konstep is verder ontwikkel tot 'n fisiese p rototipe. Hierdie prototipe bevestig die vermoë om meganies te koppel en het ook insig verskaf in die vervaardiging van so 'n module.

Die gebruik van hierdie twee elemente - die orientasie afskatting en meganiese koppelvlak - as boublokke van 'n volledige, vlug-gereed, koppelingstelsel vir 'n satelliet is ook verder ondersoek met aanbevelings.

Acknowledgements

I would like to express my most sincere thanks to the following people:

- To Dr Lourens Visagie for the guidance and support he has given me over the past 3 years.
- To my parents, Charmaine Waller and Kevin Waller, for supporting me in my dreams and making them possible through numerous sacrifices and for all the love and support you have given me.
- To my sister, Hayley Waller, for keeping me motivated, being a voice to speak to when times got tough and for love and support.
- To my friends from the ESL, Pieter Goos, Welri Botes and Daniel Lourens. You have made the last 2 years, 2 of the best of my life.

Dedications

This thesis is dedicated to my mother and father. Without their numerous sacrifices I would have never have had the opportunity to pursue my dreams this far.

Contents

List of Figures

List of Tables

List of Acronyms

AAReST Autonomous Assembly of a Reconfigurable Space Telescope

APAS Androgynous Peripheral Attachment System

ARCADE Autonomous Rendzvous Control and Docking Experiment

ArUco Augmented Reality University of Cordoba

ASDS Autonomous Satellite Docking System

ATV Autonomous Transfer Vehicle

BJT Bipolar Junction Transistor

CAD Computer Aided Design

CMOS Complimentary Metal Oxide Semiconductor

CNC Computer Numeric Control

CoM Centre of Mass

CPOD Cubesat Proximity Operations Demonstration

CSI Camera Serial Interface

CUDA Compute Unified Device Architechture

DART Demonstration of Autonomous Rendezvous Technology

DOF Degree of Freedom

EKF Extended Kahlman Filter

ESA European Space Agency

ESL Electronic Systems Laboratory

EVA Extravehicular Activity

FDM Fused Deposition Modelling

FOV Field of View

FPGA Filed-Programmable Gate Array

FPS Frames per Second

GPIO General Purpose Input Output

GPU Graphics Processing Unit

IDSS International Docking System Standard

ISS Interantional Space Station

LED Light Emitting Diode

LEO Low-Earth Orbit

LIDAR Light Detection and Ranging

MEV Mission Extension Vehicle

MUBLCOM Multiple Paths, Beyond-Line-of-Sight Communications

NASA National Aeronautics and Space Administration

NDS NASA Docking Adapter

OBC On-Board Computer

PCB Printed Circuit Board

PLA Polylactic Acid

PMA Pressurised Mating Adapter

PROXBOX Proximity Box

RC Radio Controlled

RMS Root Mean Squared

SLA Stereolithography

SLS Selective Laser Sintering

SMAV Small Vehicle

SPHERES Synchronized Position Hold Engage and Reorient Experimental Satellite

STF Satellite Test Facility

TID Total Ionizing Dose

UDP Universal Docking Port

USB Universal Serial Bus

Chapter 1

Introduction

1.1 Background

Docking is the process of flying two spacecraft on a controlled collision trajectory such that the interface mechanisms of the spacecraft align and ultimately join the two spacecraft together [2]. This process has largely remained exclusive to larger spacecraft, however, the ability for cubesats, nanosatelites based on a 10 cm unit cube, to dock opens a large field of possibilities for mission applications such as reconfigurable spacecraft, on-orbit servicing and deorbiting of inoperable spacecraft.

The Electronic Systems Laboratory (ESL) at Stellenbosch University is in the process of developing a cubesat mission (Docksat) to demonstrate the docking capabilities of cubesats. As a precursor to this mission, this project includes the design of a prototype docking system for cubesats to demonstrate the feasibility of docking for cubesats. The prototype will be demonstrated on an existing air-bearing satellite test facility, developed by Jansen [3], at the ESL. The satellite test facility (STF) uses multiple carts that float on planar air bearings, on a glass bed, to simulate the low friction environment of space. The carts are propelled by a set of four cold gas thrusters that permit translation in one axis and rotation around a second.

This project will focus on the development of parts of a docking module. The purpose of this module is to prove the feasibility of developing such a module for actual space missions. As such, the module will include all the components necessary, excluding propulsion, to give a cubesat the ability to dock to another cubesat or larger spacecraft. A space ready module would allow mission planners the ability to give their cubesats docking capabilities with minimal development time.

1.2 Motivation

Below are some mission possibilities that such a module could permit:

The most obvious mission type would be the construction of larger satellites from multiple cubesats. This on-orbit construction could reduce the cost of launch of various satellites as cubesats are much cheaper to launch and a large number of cubesats could be launched in place of a larger, monolithic satellite. A perfect example of this would be a reconfigurable space telescope, such as the AAReST mission [4], or a synthetic aperture radar. Such a mission would use multiple cubesats with focussing mirrors to focus light to a central collector cubesat. After the imaging, the cubesats could then re-dock, or change current docking configuration, to make station keeping easier.

Another possible mission type could include a reconfigurable and reusable research satellite. This would make use of a standardised docking mechanism thus allowing new satellites to dock to the older servicing satellites. The idea of this research satellite would include the launch of a singular monolithic satellite platform that would have numerous docking positions for various cubesats. This monolithic satellite would contain all the infrastructure needed to support space experimentation. This could include large solar panels for power generation, a high bandwidth up/downlink for reletively fast data transfer, station keeping capabilities and possibly even refuelling of cubesats. Cubesats would then be launched that contain a specific experiment that an organisation would like performed. The cubesat would then manoeuvre and dock to the monolithic satellite. The cubesat can then perform its experiment where it would have more power available and larger data up/downlink capabilities. At the end of the experiment, the cubesat can then be un-docked and de-orbited and another cubesat with a different experiment can be launch to take its place. This could potentially facilitate more scientific research for cheaper as a dedicated satellite does not need to be launched for each experiment. This could also improve the research space aboard the International Space Station (ISS) as autonomous experiments would not need to be sent to the ISS and installed by an astronaut.

The ability for cubesats to dock to other satellites could also permit the use of small cubesats to de-orbit satellites that have lost the ability to control themselves or can no longer de-orbit by itself. A small cubesat can thus be launched with some de-orbiting technology, such as a drag sail or electronic propulsion, that can dock to the old satellite, deploy the technology and thus de-orbit the satellite. This could greatly reduce the amount of space debris left in orbit.

Small cubesats can also be sent up with larger satellites to facilitate on orbit maintenance and inspection. Such a cubesat would be docked to the larger satellite. This cubesat can then un-dock from the mother satellite, circumnavigate the satellite inspecting the entire satellite exterior and then re-dock. Small cubesats could also facilitate basic maintenance functions for such satellites such as replacement of small parts using small robotic manipulators.

Finally, a cubesat could also be used to aid astronauts on Extravehicular Activities (EVAs). The cubesat could be docked to the side of the ISS and during an EVA, the cubesat could bring tools or parts to the astronauts allowing them to move to the site of the repair or installation rather than first needing to go collect the part to be installed or replaced from another part of the ISS. This could improve the effectiveness of EVA missions as EVA missions can be very strenuous for the astronauts.

1.3 Objectives

The objective of this project is to contribute to the design and development of a docking module to be used on the satellite test facility in the ESL. As such, the system does not need to be space-ready but should approximate what would be possible on a space-ready solution. The focus of this project is the physical docking mechanism used to join the two test carts together and a pose estimation system used for manoeuvre planning and control for the docking procedure.

The aim of this project is, thus, to:

1. Design and develop parts of a cubesat docking module including:
   - a mechanical docking interface.
   - a pose estimation system.
2. Determine the accuracy of the pose estimation system.
3. Analyse and comment on the feasibility and required changes needed to adapt the prototype experiment to a flight solution.

1.4 Thesis Outline

Chapter 2 is a review of the literature use in this thesis. It covers a brief history of autonomous rendezvous and docking followed by a brief look at various docking mechanisms for large and small spacecraft. Following this is a brief discussion of pose estimation techniques in use and from literature. Finally, the satellite test facility on which the module will eventually be tested is briefly

described.

Chapter 3 covers the high level system overview of the module. In this section, the specifications governing the design of the docking module and pose estimator is outlined as well as some of the system level design choices.

Chapter 4 is an in-depth look at the complete imaging system used for pose estimation. The section starts with a discussion on the hardware chosen. The various software elements that make up the pose estimator are then discussed. Finally, the testing of the pose estimator from initial functionality testing through to complete system accuracy tests are discussed.

Chapter 5 details the design of the physical docking interface. Three different concepts explored are discussed and the initial results from the prototype development are discussed.

Chapter 6 covers the steps that would be necessary to turn the elements described in previous chapters into a space-ready solution.

Chapter 7 is a conclusion of this thesis. This chapter provides an overview of the previous chapters followed by recommendations to complete the prototype docking module as well as for future work that could improve the prototype.

Chapter 2

Literature Review

The chapter summarizes the most notable literature and background for satellite docking. Section 2.1 gives a brief overview of the history of autonomous docking missions. Section 2.2 focusses on the mechanisms used in various manned and autonomous docking missions. This section looks at both large scale docking mechanism in Section 2.2.1, and mechanisms designed for micro- and nanosatellites in Section 2.2.2. This chapter then goes on to explain some of the pose estimation methods proposed for spacecraft in Section 2.3. Finally, a brief overview of the satellite test facility, where the module will eventually be tested, is given in Section 2.4.

2.1 A History of Autonomous Rendezvous and Docking

The first fully autonomous rendezvous and docking mission was performed by the USSR in October, 1967. During the mission, two modified Soyuz spacecraft, designated Kosmos-186 and Kosmos-188, performed seeking, rendezvous and docking operations. This technology became an integral part of the Salyut and Mir space stations and remains in practice on the Russian segment of the ISS. [5]

The Demonstration of Autonomous Rendezvous Technology (DART) mission was the first attempt at a fully autonomous rendezvous and docking manoeuvre performed by the United States in April, 2005. The rendezvous operations were performed successfully, however, during proximity operations, the DART spacecraft collided with the Multiple Paths, Beyond-Line-of-Sight Communications (MUBLCOM) satellite, the target satellite, ending the mission prematurely. [6, 7]

More advancements in automated rendezvous and docking technology lead to the advent of automated resupply spacecraft for the ISS. These spacecraft include Progress, the Automated Transfer Vehicle (ATV) and Cargo Dragon [8, 9]. Other spacecraft such as the Cygnus spacecraft also resupply the ISS however these are berthed to the station rather than docking autonomously [10].

Current state-of-the-art for autonomous docking includes the Cargo Dragon spacecraft which first flew in 2020. This spacecraft was designed to resupply the ISS. Unlike the previous generation of Dragon spacecraft, Cargo Dragon (or Dragon 2) is able to autonomously dock to the ISS [9]. Further state-of-the-art missions includes the Mission Extension Vehicle (MEV), developed by Northrop Grumman, which was launched in October 2019. This spacecraft was designed to autonomously dock to retired satellites in order to bring them back into service. This is done without the need for a dedicated docking port [11]. Finally, a smaller scale docking mission includes the SPHERES spacecraft. These nanosatellites fly on-board the ISS as a robotic operations test platform where they are used to perform various experiments including autonomous docking [12].

2.2 Docking Mechanisms

2.2.1 Traditional Docking Mechanisms

The first mission to achieve spacecraft docking in orbit was the Gemini VIII mission in March, 1966. During this mission the Gemini spacecraft successfully docked to the Agena spacecraft. This docking mechanism made use of a cup and cone interface. This mechanism can be seen in Figure 2.1. This mechanism had the male interface on the Gemini spacecraft and female interface on the Agena spacecraft. This interface simply held the two spacecraft together with an electrical connection which gave the Gemini astronauts control over Agena's systems. Crew transfer was not possible however.[13]

Both the Apollo and Soyuz spacecraft made use of a probe and drogue design. A diagram of the Soyuz mechanism can be seen in Figure 2.2 and a diagram of the Apollo mechanism can be seen in Figure 2.3. Similar to the Gemini mechanism, this mechanism made use of a male probe that was inserted into the female drogue. Soft capture was achieved when the capture latches were activated that held the probe and drogue together. The probe was then retracted and a series of hard capture latches created a structural seal between the two spacecraft. Both the Apollo and later Soyuz mechanisms allowed crew to be transfered. An updated Soyuz mechanism is still in use

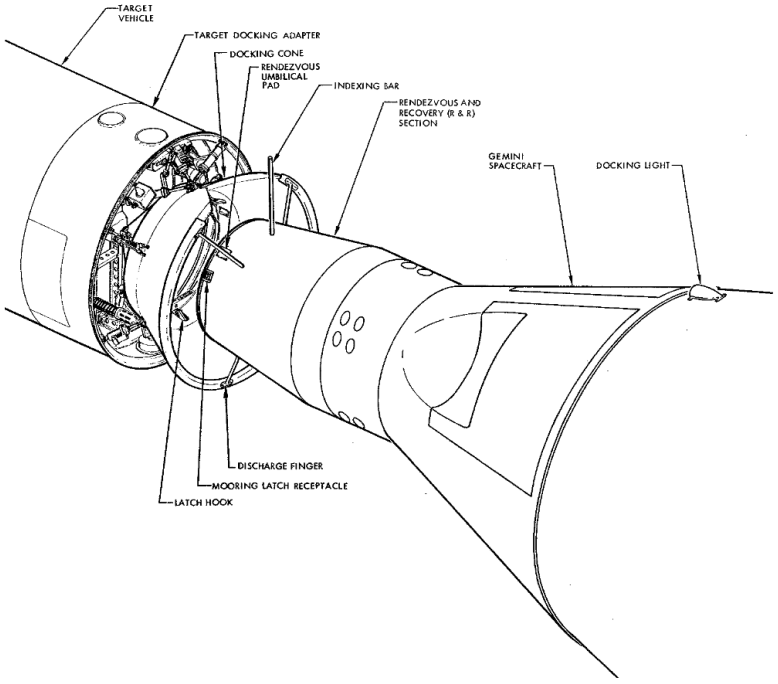

Figure 2.1: The probe and cone mechanism used on the Gemini VIII mission.[13]

today aboard the ISS. [14]

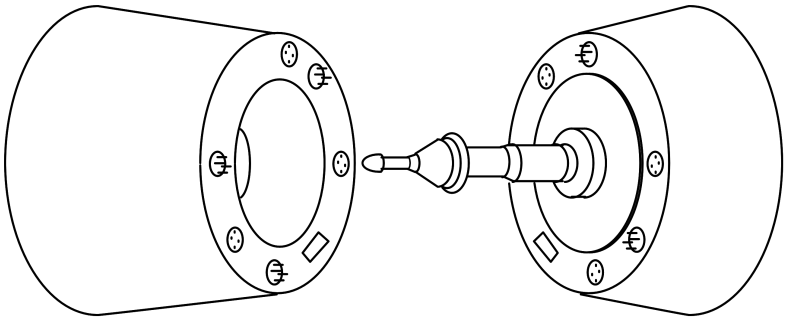

Figure 2.2: The original Soyuz docking mechanism.[15]

The first androgynous docking adapter, an adapter where both interfaces use the same mechanism, was developed for the Apollo/Soyuz project. This mechanism was named the Androgynous Peripheral Attachment System (APAS-75). This mechanism made use of 3 outward facing guide petals that would guide the two spacecraft together on contact. Unlike the probe and drogue style mechanisms, the guide ring on the APAS could be used in the active, extended state or the passive, retracted state. This meant that either spacecraft could be used as the active spacecraft and thus the adapters were not gendered

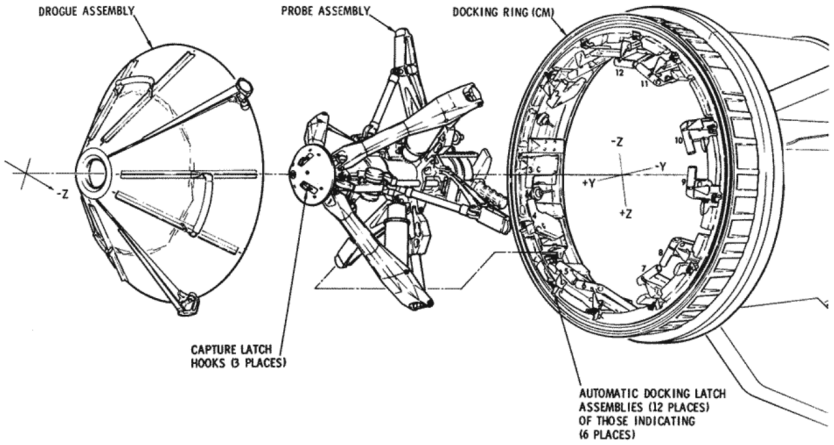

Figure 2.3: The probe and drogue mechanism used on the Apollo missions.[16]

hence it being androgynous [17]. A diagram of the APAS-75 mechanism can be seen in Figure 2.4. This mechanism later evolved into the APAS-89 that was used on the Mir/Shuttle program [15]. The main difference between the two mechanisms was that the guide petals were moved to the interior of the guide ring. This mechanism was used aboard the ISS in the form of the Pressurised Mating Adapter (PMA) during the Shuttle program. This adapter is no longer fully androgynous, however, as the station side adapter is fixed in the passive state and thus docking spacecraft are assumed to always take the active role [14].

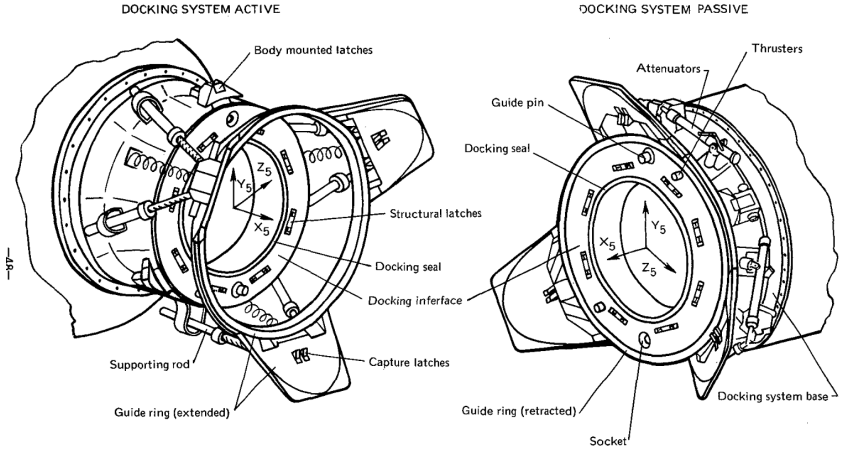

Figure 2.4: The APAS-75 mechanism used in the Apollo/Soyuz project.[17]

The most recent docking adapter is the NASA Docking System (NDS) which conforms to the International Docking System Standard (IDSS) [18].

This standard was released in October, 2010. This adapter looks similar to the APAS-89 and APAS-95 mechanisms with 3 interior guide petals and a retractable guide ring. A diagram of the NDS mechanism can be seen in Figure 2.5. The NDS was placed on the two PMA's on-board the ISS to convert them to the new IDSS [19].

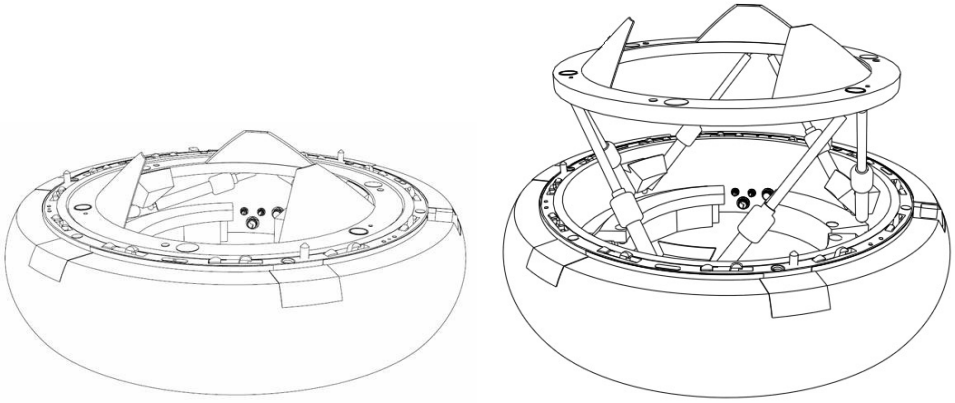

Figure 2.5: The NASA Docking System in the retracted and extended positions. [20]

2.2.2 Docking Mechanisms for Micro- and Nanosatellites

The use of miniturised docking mechanisms for micro- and nanosatellites is a fairly recent advancement in the satellite field. A few of such mechanisms have been designed but very few have been flight-tested.

A small probe and cone mechanism was proposed by Underwood et al. [4] for use on the proposed AAReST mission. This mission involves the use of a 15U cubesat with two 3U cubesats that can be un-docked and re-docked to form a space telescope. This mechanism is based off the Kelvin Clamp principle. Small permanent magnets are used to hold the docked spacecraft together and electromagnets are used to separate the spacecraft. This mechanism can be seen in Figure 2.6.

The Autonomous Satellite Docking System (ASDS), proposed by Ritter et al. [22], is also a probe and cone mechanism. This mechanism makes use of a soft-docking cable that is extended into the cone. The cable is then retracted to seat the head of the probe into the cone for the hard-docking operation.

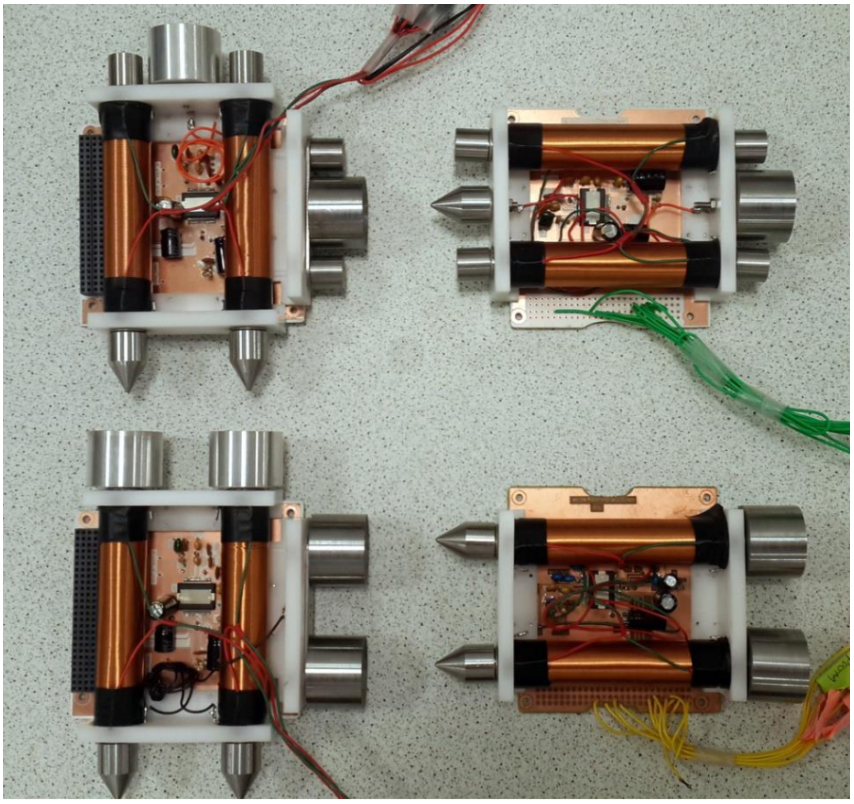

Figure 2.6: The CoreSat (Left) and MirrorSat (Right) docking units for the AAReST mission. [21]

Another probe and cone mechanism, proposed by Boesso and Francesconi [23] and improved upon by Barbetta et al. [24], is the ARCADE and ARCADE-R2 respectively. This mechanism used a spring loaded probe and electromagnet as the soft-docking mechanism and 3 locking solenoids for the hard-dock. A CAD diagram of the docking module can be seen in Figure 2.7. Both these docking mechanisms were tested on-board a BEXUS high-altitude balloon.

A semi-androgynous docking adapter is proposed by Olivieri and Francesconi [25]. This mechanism uses eight movable petals that that allow one mechanism to fit within the other mating the two spacecraft. A CAD model of the docking adapter can be seen in Figure 2.8.

The Universal Docking Port (UDP), proposed by Rodgers et al. [26], is an androgynous docking mechanism that places both a probe and a socket on a single mechanism. The probe is inserted into the socket where a pair of rotating disks locks the probe in place preventing the spacecraft from separating. A CAD diagram of the UDP can be seen in Figure 2.9. The UDP was tested on-board the ISS on the SPHERES test platform [27].

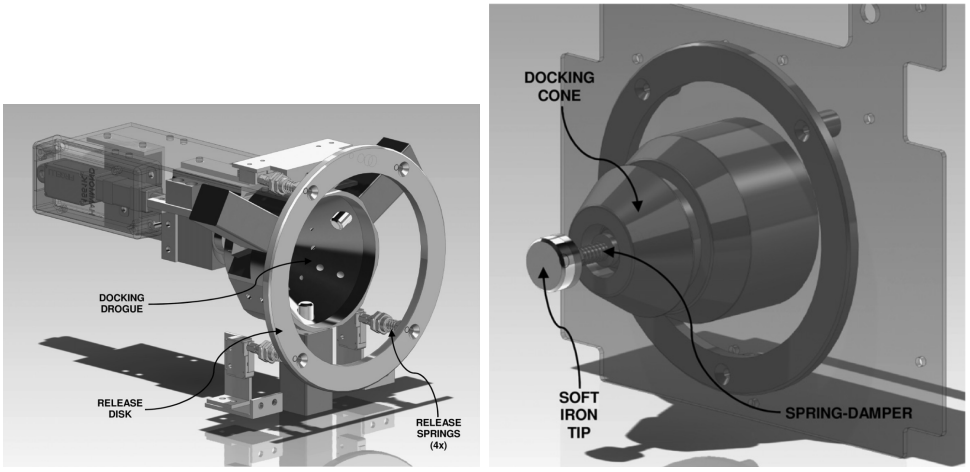

Figure 2.7: The PROXBOX (Left) and SMAV (Right) docking interfaces for the target and chaser satellites for the ARCADE mission. [23]

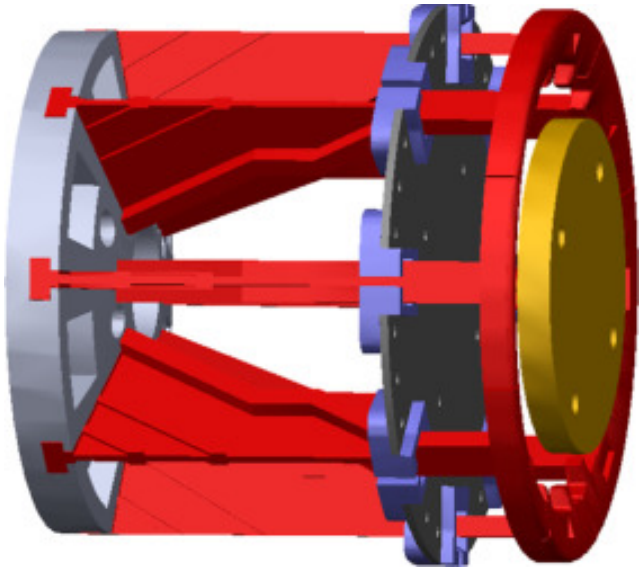

Figure 2.8: The Semiandrogynous docking adapter proposed by Olivieri and Francesconi. [25]

The Cubesat Proximity Operations Demonstration (CPOD) is a free flying cubesat mission to demonstrate docking operations on cubesats [28]. The free flying nature of the mission adds far more complexity than that of the SPHERES mission. This is because orbital manoeuvres need to be passively safe as well as all guidance and navigation has to come from the satellite itself.

Of all the docking mechanism mentioned in Section 2.2.2, only the UDP has flight heritage and only in the confides of the ISS. None of these mechanism have ever been used on a free flying mission however many of them have

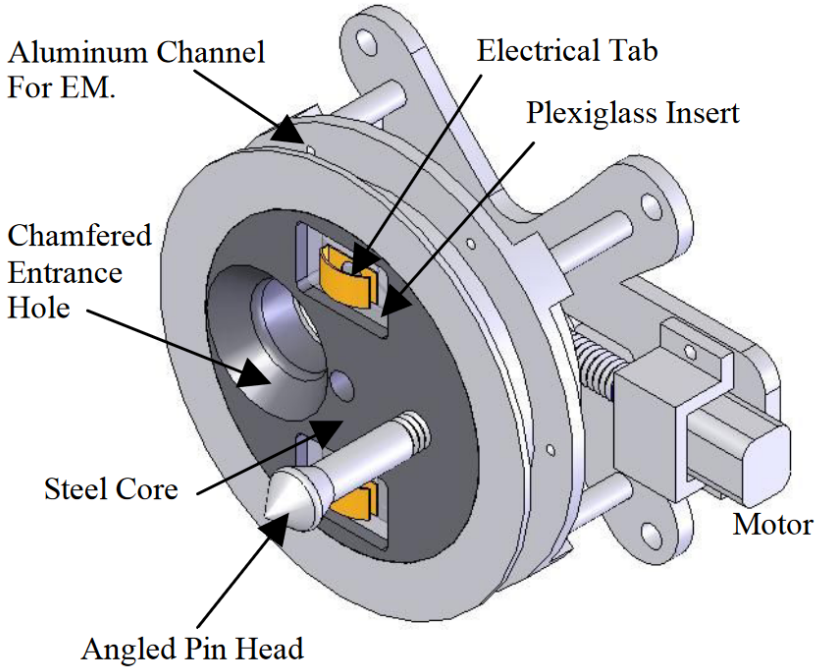

Figure 2.9: A CAD model of the Universal Docking Port. [26]

been designed for use with proposed missions.

2.3 Pose Estimation

In order to achieve successful autonomous docking, a satellite needs to understand its position, velocity, rotation angles and rotation rates relative to is target, also know as its relative pose.

The pose is defined as:

1. the distance to the target
2. the azimuth and elevation to target
3. the roll, pitch and yaw of the target

These measurements are generally obtained with the use of a pose estimator. The pose estimator makes use of a combination of sensors that will return the targets telemetry relative to the chaser allowing the chaser to perform manoeuvres to align and dock. Filtering techniques may also be employed to achieve smooth and accurate measurements.

Pose estimation of satellites is generally achieved by the use of an imaging system. These imaging systems could be monocular cameras, stereoscopic cameras or LIDAR. The cameras will generally image some form of fiducial marker or possibly use edge detection and pattern matching to match the pose of a know spacecraft to its model.

An example of a fiducial marker currently in use is that on the ISS NDA. This adapter uses 3 different targeting systems: the centreline docking target, the peripheral docking target and the perimeter reflector target. These targets can be seen in Figure 2.10. The different docking targets are used at different distances from the docking adapter. These targets allow an approaching spacecraft to determine the full 6 DOF relative position and angle of the docking adapter [18].

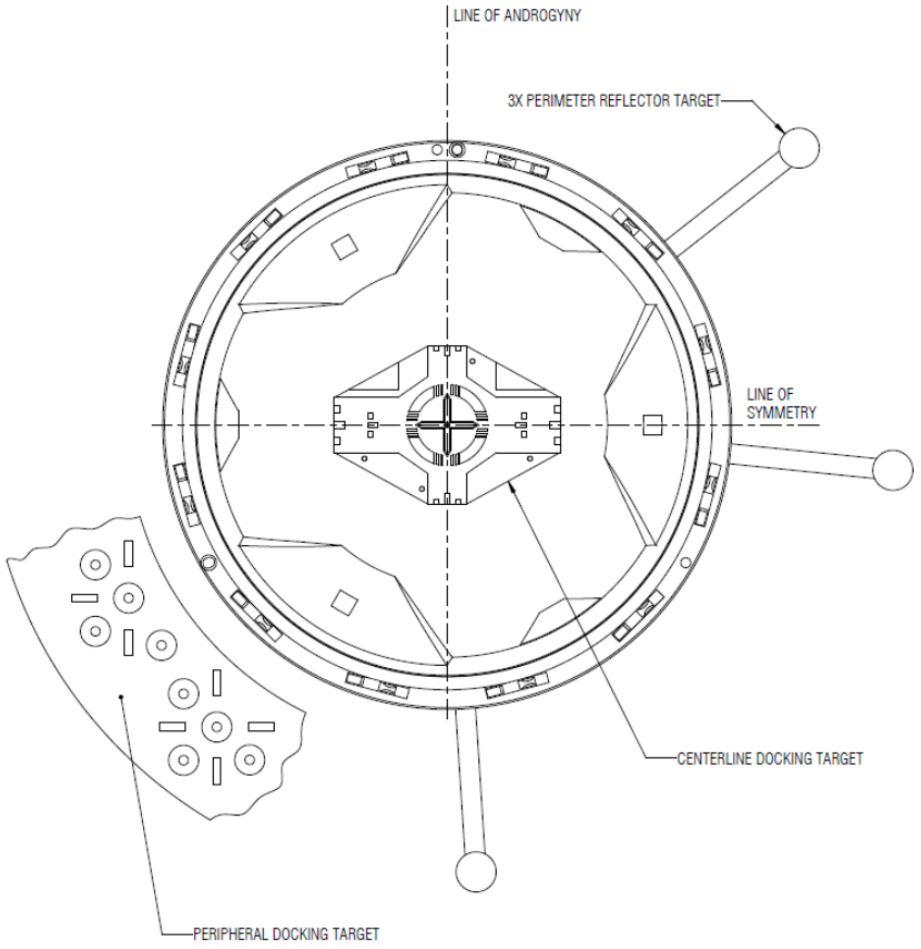

Figure 2.10: The targets used within the IDSS.[18]

Another example of a fiducial based system is that proposed for the AAReST mission. The two mirrorsats use a set of LED glyph markers on each of the faces. The camera on the coresat uses blob detection to find the LEDs within its field-of-view and then uses pattern matching to determine the relative pose of the mirrorsats [29]. Sansone, Branz and Francesconi [30] proposed a similar fiducial system. This system uses two sets of LEDs to obtain the relative pose of the imaged satellite. The two sets of LEDs are used at different distances.

In July, 2019, the ESA held a pose estimation challenge in which the goal was to estimate the pose of the Tango satellite. This satellite did not feature fiducial markers for pose estimation and thus a machine learning approach was generally used. The winning team, UniAdelaide, made use of a deep landmark regression model to determine the pose of the satellite [31]. Kisantal et al. [32] reports on the competition as well a few of the methods used by the various teams.

Kelsey et al. [33] proposes a model-based pose refinement algorithm to improve the results from visual-based pose estimation. The algorithm was tested with the VISARD analysis testbed.

2.4 Satellite Test Facility

A Satellite Test Facility (STF) was designed by Jansen [3] for use as a test platform for future satellite missions within the ESL. The STF makes use of multiple carrier carts that float on air bearings to simulate the low-friction environment of orbit.

These carts possess a high-pressure tank that stores nitrogen at a pressure of 124 bar. This nitrogen is used by air-bearings that create a thin gas film that the carrier cart floats on. The facility also uses a glass table that ensure the carts have a relatively flat, smooth surface to operate on. This reduces the disturbances on the system that would be caused by even minor slopes in the surface. An image of a carrier cart on the glass table can be seen in Figure 2.11.

The carrier carts are propelled by a set of cold-gas thrusters that make use of the same nitrogen source as the air-bearings. These thrusters are arranged in an H-pattern as can be seen in Figure 2.12. This arrangement permits translation in a single axis by firing both thrusters on one side of the cart and rotation by firing diagonally opposing thrusters. The carts are able to operate for approximately 15 minutes with the thrusters operating at a 10% duty cycle.

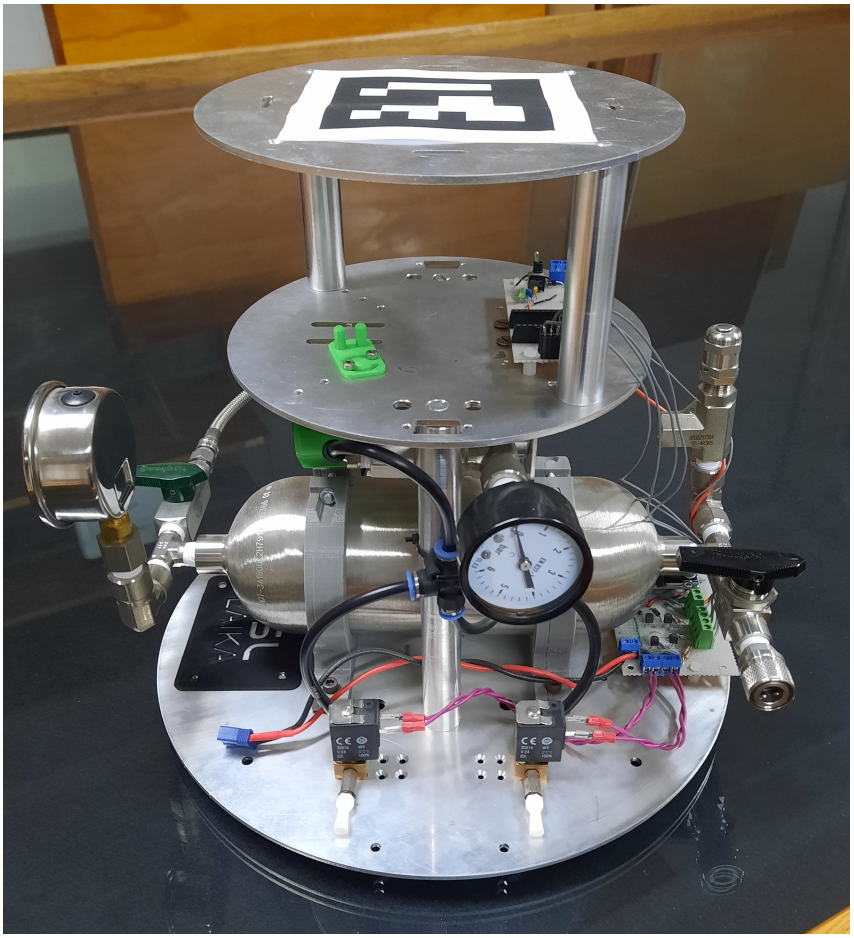

Figure 2.11: One of the carrier carts on the STF.

A further feature of the STF is the addition of an ArUco marker system that is used to determine the pose of the carts within the facility. The system is intended to provide ground truth pose measurements of the test carts. This system makes use of a camera mounted above the glass table that images the entire table surface. This video stream is then analysed to find the ArUco markers on the top of the carts. The position of the carts is then compared to a marker that is fixed to the corner of the table. The system is able to measure the position of the carts with an average accuracy of 1.2 cm. The rotation of the carts is able to be measured with an average accuracy of 0.04 rad. The translational velocity and rotational velocity are able is measured with an average accuracy of 0.04 m/s and 0.05 rad/s respectively [3].

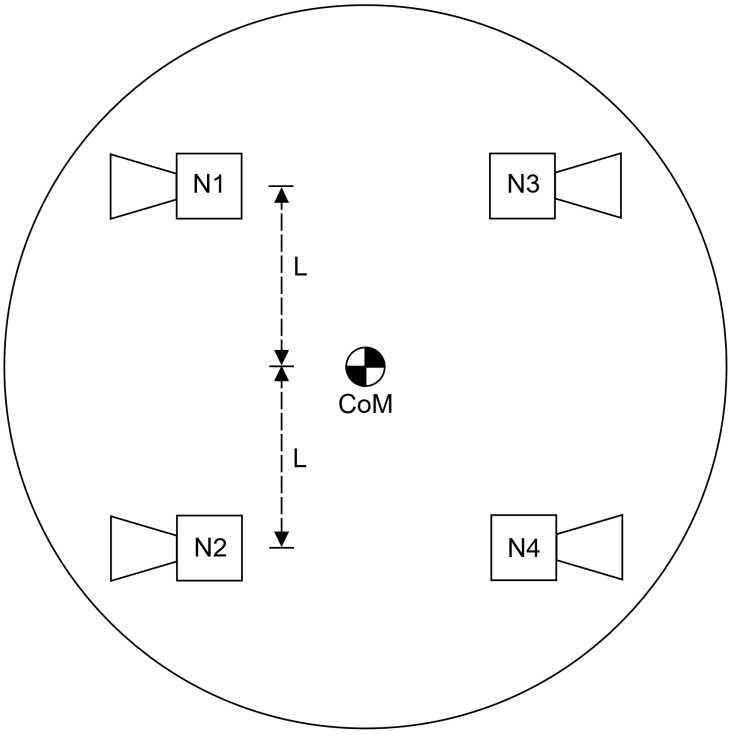

Figure 2.12: The configuration of the thrusters on the carrier cart.

Chapter 3

System Overview

This chapter discusses the system-level design choices. The specifications of the various components are also outlined.

3.1 High-Level System Design

As mentioned, this project will focus on specific aspects of the docking module. A system-level block diagram can be seen in Figure 3.1. The module elements considered for this project are those within the dashed block. Some potential solutions and desired features are listed in each of the considered blocks.

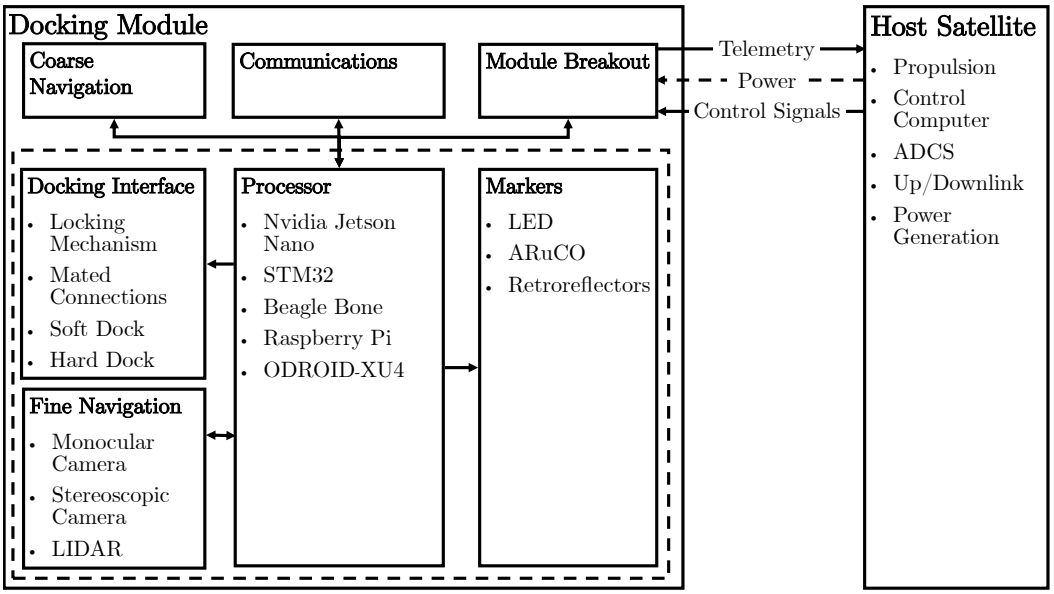

Figure 3.1: System block diagram of the docking module.

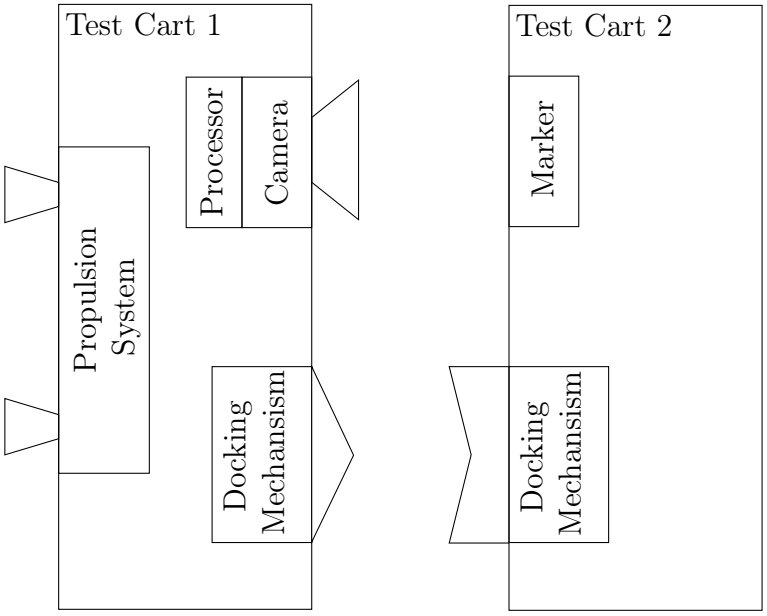

Figure 3.2: Block diagram of the proposed docking module components on the test facility.

A monocular optical imaging system was settled on for the fine navigation system. In this system, a camera on the chaser cart will image a set of fiducial markers on the target cart. The images from the camera will then be processed on an on-board processor. The telemetry of the target satellite would then be passed to a control board on the host satellite for manoeuvre planning. The host satellite is considered for the development but falls outside the scope of this project.

The docking interface was chosen to be a mechanical mechanism for hard docking. This was chosen as it would allow multiple un-docking and re-docking operations not inherent in mechanism such as permanent magnet systems or Velcro. Electro-magnets were not considered as the interference it would cause with sensor systems, such as magnetometers, was undesirable. No shared connections between mated adapters was considered for the initial prototype.

A diagram of the how the components considered fit into the satellite test facility can be seen in Figure 3.2.

3.2 Specification Overview

In order to determine a good set of alignment specifications for the docking mechanism, the specifications of a mechanism with flight heritage was considered. In this case, the IDSS was used. The IDSS outlines specifications

for initial contact of the two docking components. An extract of the relevant conditions can be seen in Table 3.1.

Table 3.1: Extract of initial contact conditions table from the IDSS [18].

Initial Contact Condition	**Limiting Value**
Lateral (radial) misalignment	0.1 m
Pitch/Yaw misalignment	4° (vector sum of pitch and yaw)
Roll misalignment	4°
Pitch/Yaw Rate	12 °/min(vector sum of pitch and yaw) rates
Roll Rate	12 °/min

These values can then be scaled down to find specifications for a cubesat sized spacecraft. The IDSS specifies the diameter of the docking mechanism to be 1.2 m. To fit on a cubesat, this would have to be scaled down to 0.1 m i.e. applying a scaling factor of $\frac{1}{12}$. Applying this scaling factor to the lateral misalignment specification yields a radial misalignment of 8.333 mm. A design value of 10 mm was thus used. The angular misalignments specifications were also increased to 5°. These values were increases as accurate control on cubesats can often be more difficult than on larger satellites due to the size of their control and propulsion systems. These larger values thus provide a greater margin of error for the mechanism improving the chances of successful docking. The angular rates values were not changed for the design. A table of the design specifications can be seen in Table 3.2.

Table 3.2: The design specification used for the docking mechanism.

Initial Contact Condition	**Limiting Value**
Lateral (radial) misalignment	10 mm
Pitch/Yaw misalignment	5° (vector sum of pitch and yaw)
Roll misalignment	5°
Pitch/Yaw Rate	12 °/min(vector sum of pitch and yaw) rates
Roll Rate	12 °/min

Another important specification for the docking module is the use of an androgynous docking mechanism. This is a mechanism that is not gendered i.e. it makes use of the same mechanism for both mating devices. This is to facilitate modularity for potential space missions that could use this module. Having an androgynous module means that the same module can be used on both the target and chaser spacecraft thus preventing the need to design two separate modules. Further, having an androgynous module means that spacecraft could potentially dock to other spacecraft that were not originally part

of the mission outline such as sending a new module to a compound satellite made of multiple cubesats.

The ability to dock multiple times was considered important as it would allow for greater flexibility for mission planning. The mechanism should thus be able to dock to another spacecraft, securely hold the two spacecraft together, and then release the two spacecraft. This procedure should be able to be repeated multiple times without failure.

In order to achieve a successful dock, a control system would need to put the satellite within the misalignment specifications of the docking adapter. For this level of control to be possible, the measurement values used by the controller need to be better than the docking specification. The same design specifications, those in Table 3.2, were thus also used for the pose estimations system. Accurate control can often require an operational frequency of the control system of up to 10 Hz. From the Nyquist theorem, the sample frequency of the pose estimator should thus be at least 20 Hz. A target sample frequency of 100 Hz was chosen to guarantee accurate control.

Chapter 4

Imaging System

This chapter describes the design, implementation and testing of the pose estimation system. The section starts with an outline of the hardware that was used for testing. The software implementation of the pose estimator is then discussed. Finally, the testing and test results are discussed: the tests used to determine whether the various elements of the pose estimator system were working correctly are discussed first followed by the testing of the complete system.

4.1 Hardware Selection

4.1.1 Processing

Due to the large number of calculations needed to process an entire image and the high frame rate required for accurate control, a fast processor was needed for the image processing. A Nvidia Jetson Nano development board, seen in Figure 4.1, was selected for this reason. The Jetson Nano has a relatively fast 1.43 GHz, quad-core processor allowing the imaging system to process the images at relatively fast frame rates. The Jetson Nano also possesses two Camera Serial Interface (CSI) connectors that can be used to quickly and easily attach a camera to the development board. The Jetson Nano also possesses a 128 CUDA-core GPU which could potentially be leveraged to further improve the processing speed of the images by parallelising the image processing. The relatively cheap price of the Jetson Nano further made it a desirable choice for the processing unit. The Jetson Nano also runs Jetpack, a linux distro developed for the Jetson, which means that development is possible directly on the Jetson Nano without the need of an external computer. Finally, the size of the development board was very appealing as it would be able to fit within a 10 cm X 10 cm docking module (A module that could fit on a cubesat). [34, 35]

The major drawback of the Jetson Nano is that it has a relatively high power usage. At maximum power mode, it consumes up to 10 W and the carrier board could draw up to a further 10 W. When used on a stationary test bench, this is not a problem as a power supply can easily handle this power requirement. When used on the carts or on a satellite, however, this high power requirement has to be supplied by a battery. This puts a major limit on the lifespan of a test before batteries need to be charged again. Further discussion of its use on satellites is discussed in Chapter 6. The use of Jetpack on the Jetson Nano also makes interacting directly at a hardware level, such as setting GPIO pins, more difficult than on other microcontrollers potentially increasing development time.

Figure 4.1: Nvidia Jetson Nano on its carrier board. [36]

4.1.2 Camera Sensor

A Waveshare camera module based on the Sony IMX219 CMOS sensor was selected for the imaging system. An image of this module can be seen in Figure 4.3. This module was selected for its compatibility with the Jetson Nano: the module uses a CSI connector to interface with the Jetson directly. This allows the Jetson to make use of its dedicated video encoder speeding up the processing of images. Further, the sensor has an effective resolution of

3280 X 2464 (8.08 Megapixles). This relatively high resolution could possibly make the pose estimation more accurate as more accurate location data can be gathered with the higher pixel density. The disadvantage of this resolution is that the possible frame rate is reduced. A figure showing the possible frame rates at various resolutions, returned from the camera module, is given in Figure 4.2. Like the Jetson Nano, the relatively cheap price and small size make this module very desirable for a small docking module.

```
GST_ARGUS: Available Sensor modes :
GST_ARGUS: 3264 x 2464 FR = 21.000000 fps Duration = 47619048

GST_ARGUS: 3264 x 1848 FR = 28.000001 fps Duration = 35714284

GST_ARGUS: 1920 x 1080 FR = 29.999999 fps Duration = 33333334

GST_ARGUS: 1280 x 720 FR = 59.999999 fps Duration = 16666667

GST_ARGUS: 1280 x 720 FR = 120.000005 fps Duration = 8333333
```

Figure 4.2: Available sensor modes for the camera module.

4.1.3 Lenses

The Waveshare module has a M12 lens mount on it. The module comes with a 200° Field-of-View (FOV) lens. This lens was chosen in order to easily locate the target satellite in the absence of other sensors that provide the relative location of the target satellite. The downside of this large FOV is it introduces large lens distortions that make correction difficult thus making measurements less accurate. Further, small changes in the distance of the target lead to large changes in the size of the target on the image meaning the effective range in which pose estimation is possible is reduced compared to a smaller FOV lens.

4.1.4 Marker

The pose estimator makes use of a set of LEDs on a marker. This is discussed further in Section 4.2.2. A set of OSRAM LR R976-NR-1 LEDs were chosen for the marker due to their relatively high luminous intensity [37]. These LEDs were placed on a custom PCB. This was done to ensure that the spacing between the LEDs was as accurate as possible. The 5^{th} LED was placed on a 3D printed stand-off to ensure it was at the correct distance from the board. An image of the marker can be seen in Figure 4.4. Due to some microcontrollers,

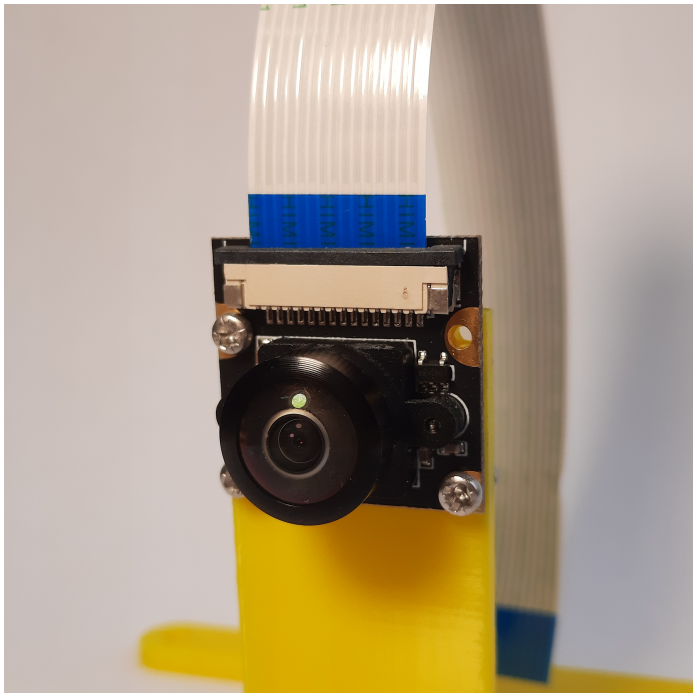

Figure 4.3: Waveshare camera module with a 200° FOV lens.

such as the Jetson Nano, not being capable of sourcing enough current to power all 5 LEDs, a BJT was used that switches a main power source. The BJT is intended to be switched by a GPIO pin on a microcontroller while the power comes from some other power source capable of sourcing sufficient current. The board thus has 3 inputs: 5 V in to power the LEDs, GPIO in to switch the BJT and ground.

4.2 Software

4.2.1 Distortion Correction

As mentioned in section 4.1.3, camera lenses add distortion to the captured images. In order for accurate measurements to be made using these images, this distortion needs to be corrected. In general, the larger the FOV of the lens, the more distortion the lens adds to the image. The 200° FOV lens used adds a very large amount of distortion to the image. Initially, the OpenCV library was used to try and correct for this distortion however it was found that once the FOV of the lens goes above 180° the algorithm fails to work correctly. It is believed this is due to the singularity that exists at 90° (half of 180°) in the tan function and the correction algorithm was not designed to handle such cases. Thus a new distortion correction algorithm needed to be found.

Figure 4.4: LED marker board with 3D printed standoff.

The OCamCalib camera calibration toolbox developed by Scaramuzza [38] is thus used. This algorithm is designed to calibrate images captured by catadioptric and fisheye cameras. The toolbox is used in the form of a Matlab script. Thus, the camera is calibrated by importing a number of images containing a calibration pattern, seen in Figure 4.5, in various orientations. The script then generates a .txt file that can then be imported into the pose estimation code. This file contains the distortion function of the lens as well as the inverse distortion function and some other information such as optical centre and misalignment correction factors. The centroid positions are then undistorted using a method from the OCamCalib toolbox that was ported to C++.

4.2.2 Pose Estimation

The pose estimation system was based off that proposed by Pirat et al. [39]. This system makes use of a target of 5 LEDs. These LEDs are placed in a cross pattern such that 4 of the LEDs are co-planar and equidistant from the centre of the pattern and the final LED is out of plane by the same distance. A diagram of this target is seen in Figure 4.6. Pirat et al. proposes using the target with an extended kahlman filter (EKF) with an analytical solution

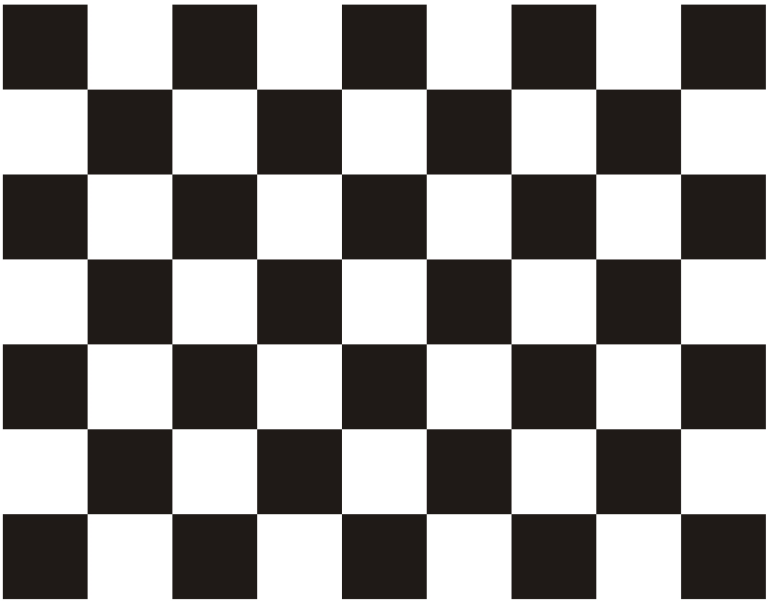

Figure 4.5: The chequerboard calibration pattern used to calibrate the camera.

used as a check for the filter. The advantage of this is that, should one of the LEDs fail, only two of the 4 in-plane LEDs are needed to solve the 6 degree-of-freedom (DOF) problem.

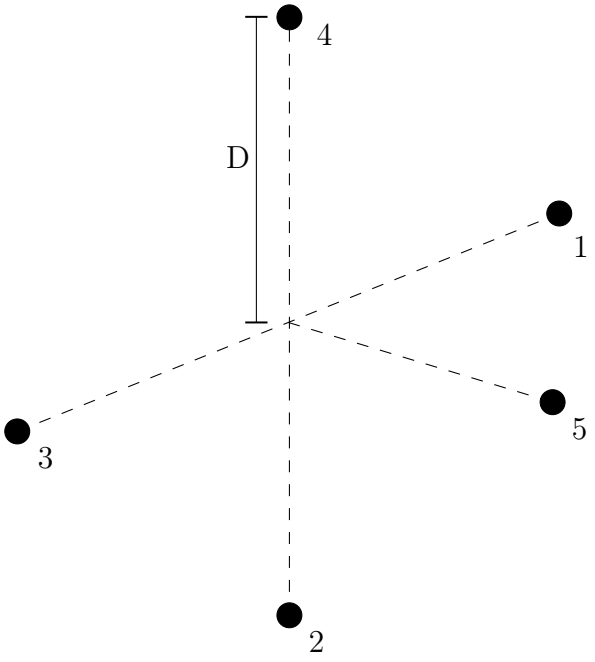

Figure 4.6: Diagram of the LED target pattern.

The analytical solution is used for the pose estimator in this case however. The reason for this is that the analytical solution is much easier to implement into the code. The analytical solution could also potentially be used on both the satellite test facility and a space-ready solution as the pose estimator does not requires completely modelling the dynamics of the system unlike the EKF. This modelling would be very time consuming.

The downside of the analytical solution is that all 5 LEDs are needed for the solution. Further, the 5 LEDs have a rotational symmetry of 4 about the pattern centre meaning that a roll of more that 90° cannot be discerned. This could be overcome by adding a 6^{th} LED to the pattern. The EKF also may have the added advantage of being more accurate especially when the target is not in the centre of the image as it makes use of the dynamics of the satellite system. Ultimately, the loss of an LED would not prove to be an issue in the demonstration as the LED could just be replaced (This is obviously not possible on a space-ready solution). This coupled with the time consuming nature of implementing the EKF lead to the decision to use the analytical solution.

The analytical solution used to solve the 6 DOF problem is outlined below. The derivation of these equations can be found in Pirat et al. [39]. The image frame used in the calculations can be seen in Figure 4.7.

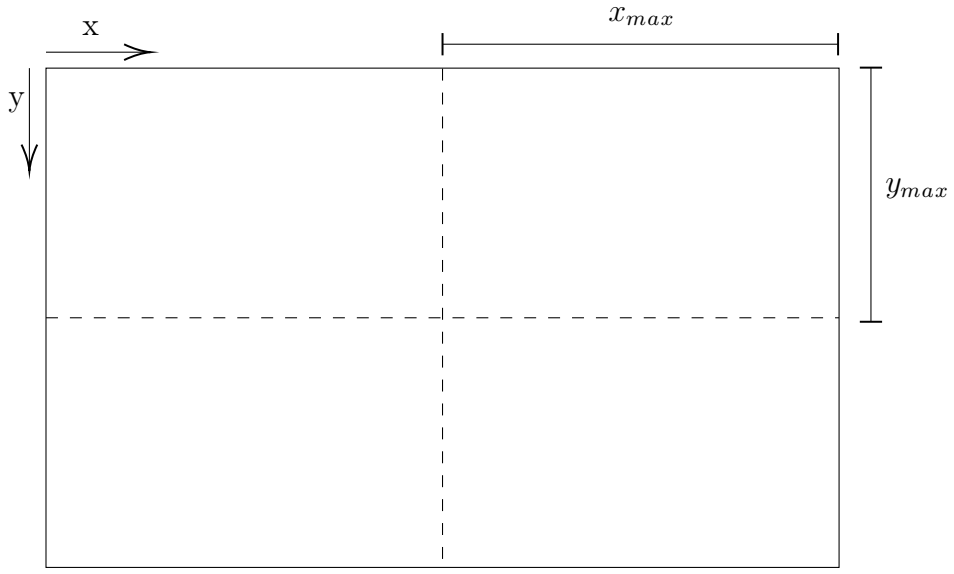

Figure 4.7: Image frame used in pose calculations.

The centre of the marker is calculated as the average position of the 4 in-plane LED's:

$$\mathbf{x}_c = \begin{cases} x_c = \frac{1}{4}\sum_{i=1}^{4} p_x^i \\ \\ y_c = \frac{1}{4}\sum_{i=1}^{4} p_y^i \end{cases} \tag{4.1}$$

where $\mathbf{p}^i = [p_x^i, p_y^i]$ is the pixel co-ordinates of the i$^{\text{th}}$ LED. The pixel co-ordinate of each LED from the pattern centre can thus be calculated as:

$$\mathbf{x}^i = \begin{bmatrix} x_x^i \\ x_y^i \end{bmatrix} = \mathbf{p}^i - \mathbf{x}_c \tag{4.2}$$

The following angles, based on the 1-2-3 Euler sequence angles, can be calculated from these new co-ordinates as:

$$\alpha = \arctan\left(-\frac{x_y^1}{x_y^2}\right) \tag{4.3}$$

$$\gamma + Az = \arcsin\left(-\frac{x_x^5}{x_y^4}\cos(\alpha)\right) \tag{4.4}$$

$$\beta + El = \arcsin\left(\frac{\cos(\gamma + Az)\cos(\alpha)}{\frac{x_x^3}{x_y^5} + \sin(\gamma + Az)\sin(\alpha)}\right) \tag{4.5}$$

where α is the roll angle, γ is the yaw angle, β is the pitch angle, Az is the azimuth angle and El is the elevation angle. To isolate the yaw and pitch angles, the azimuth and elevation angles need to be calculated and subtracted from the results in 4.8 and 4.9 respectively. These can be calculated as:

$$Az = \arctan\left(\frac{(x_c - x_{max})\tan(Az_{max})}{x_{max}}\right) \tag{4.6}$$

$$El = \arctan\left(-\frac{(y_c - y_{max})\tan(El_{max})}{y_{max}}\right) \tag{4.7}$$

where Az_{max} is the horizontal FOV from the image centre in radians, El_{max} is the vertical FOV from the image centre in radians, x_{max} is half the horizontal resolution of the image and y_{max} is half the vertical resolution of the image. The individual Euler rotation angles can now be calculated from Equations 4.7-4.11.

The range of the target from the camera can then be calculated as:

$$R = \frac{Df}{x_x^1 \frac{w_{sen}}{2x_{max}}}(\cos(\alpha)\cos(\gamma + Az) - \sin(\alpha)\sin(\gamma + Az)\sin(\beta + El)) \tag{4.8}$$

where D is the distance of the LEDs from the pattern centre in metres, f is the focal length of the camera in metres and w_{sen} is the width of the imaging sensor in metres.

Some changes were made to the original pose estimator solution. One of the main changes is the removal of the calculation for 2 of the rotation axis, the pitch and roll axis, and one of the translation axis, the vertical translation axis. This is because these are not simulated on the satellite test facility and thus would take up computation power for no gains. The method used to calculate the azimuth angle is also changed. The azimuth angle is now calculated using the vector to the centre of the pattern rather than a ratio of the pixel co-ordinates and total viewing angle. This vector is found using the inverse polynomial obtained from the camera calibration and the *cam2world()* function included in the OCamCalib toolbox.

The *cam2world()* function returns the co-ordinates of the vector to the undistorted LED points projected onto a unit sphere as seen in Figure 4.8. These vector co-ordinates are then multiplied by the image width and a scaling factor and then added to the image centre to find the pixel co-ordinates of the points. An average of the 4 in-plane LEDs co-ordinates are then used to find the co-ordinates of the pattern centre. This is then reconverted to the vector co-ordinates. Using these vector co-ordinates, the azimuth angle can be easily calculated. Taking the arctan of the x over z co-ordinate will return the azimuth angle.

Another important measurement for docking spacecraft is the velocity of the spacecraft. The pose estimator calculates the rotation rate of the test cart by averaging the differences in yaw angle between frames. The rotation rate was also smoothed using a moving window average over a set of previous measurements. This window average was calculated as:

$$\bar{\gamma} = \sum_{i=1}^{m} \gamma_i - \gamma_{(i-1)} \tag{4.9}$$

$$\dot{\gamma} = \frac{\bar{\gamma}}{m \cdot (t_m - t_{(m-1)})} \tag{4.10}$$

where γ_i is the yaw measurement taken an incremental number of frames from measurement $i-1$, m is the number of measurements used to update the yaw rate value, and t_m is the time at measurement f. This smoothed the rate data to an acceptable level however a large amount of measurement lag was added. This was considered acceptable as the time for the measurement to settle was sufficiently small for the slow movement of satellites (and thus the test carts). The translational velocity of the test carts was not implemented

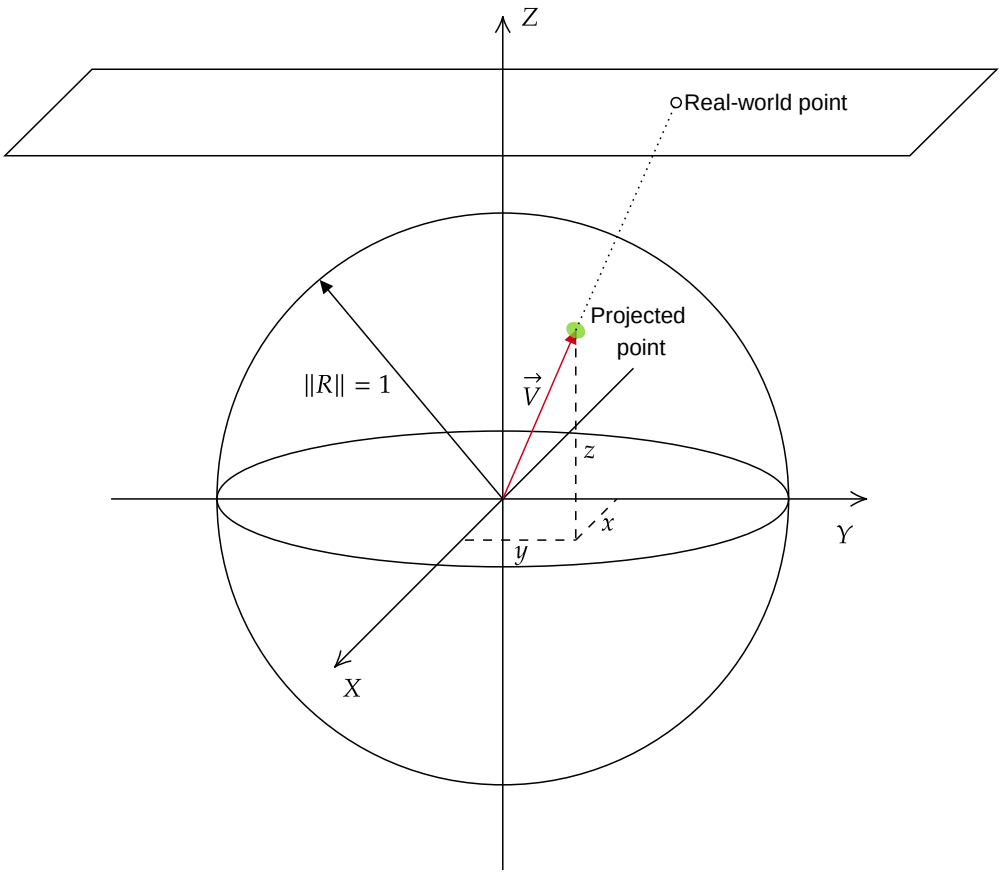

Figure 4.8: A diagram of a real-world point projected onto a unit sphere.

as there was no test rig to test this calculation, however, a similar method could be used with the azimuth angle to calculated the translational velocity and the range for the closing velocity.

Finally, the system was calibrated to give accurate measurements. It was found during testing that the measurement outputs tended to follow a straight line. Thus to calibrate the measurements, a simple constant multiplier was used. This would shift the response to align with the expected response. This calibration was applied to the yaw angle, and range measurements. It was found that the azimuth measurement was accurate enough without a calibration factor and thus one was not applied.

4.2.3 Blob Detection

A blob detector is used to find the LEDs in the image and return their centroid co-ordinates. These are then used to calculate the pose of the target.

4.2.3.1 OpenCV Solution

The first implementation of the blob detector was using the blob detector in the OpenCV package. This blob detector however made multiple passes of an image which slowed the processing speed substantially. The blob detector could be set up to only do a single pass however the LEDs were not always successfully located within the image when used in this way. In an attempt to counteract this, a thresholding pass was done on the images in order to separate the LEDs from the background. This improved the blob detections success rate, however, it had the adverse effect of greatly reducing the accuracy of the centroids of the LEDs in the image. This was due to the pixel values of the pixels making up the image of the LED being lost when the thresholding operation was done. This meant that the centroid was calculated as a simple average of the pixel co-ordinates of the pixels that made up the image. This lead to a very periodic and stepwise change in the centroid position as the image of the LED moved across the image. This response can be seen in Figure 4.9.

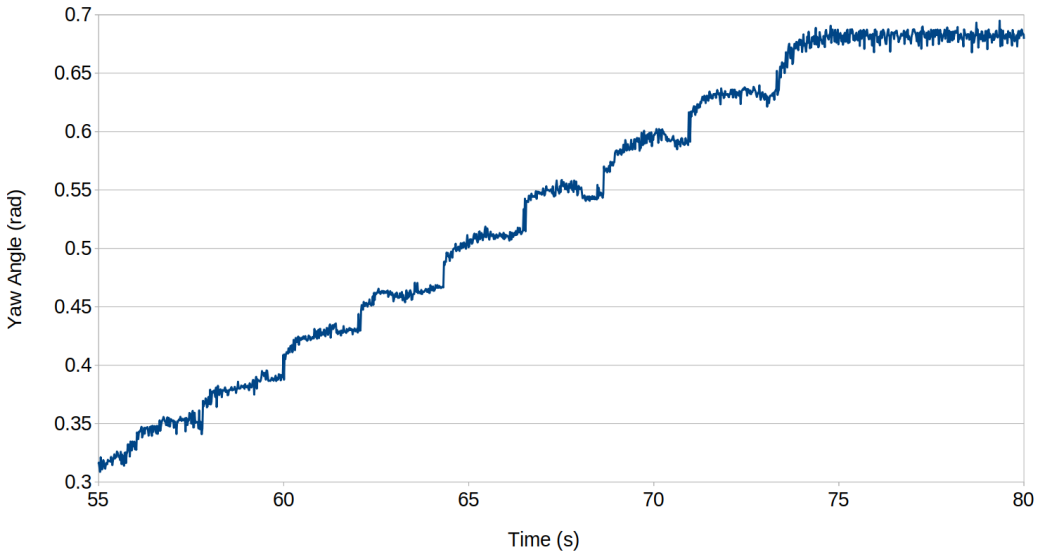

Figure 4.9: Graph of the yaw angle with the OpenCV blob detector.

This response seems to coincide with a change of about one pixel in the centroid location. The theoretical pixel shift can be calculated as follows:

$$\delta = \gamma_2 - \gamma_1 \tag{4.11}$$

where δ is the yaw angle change in radians, γ_1 is the measured yaw angle and γ_2 is the measured yaw angle with the added pixel shift. The two yaw

angles can be written in terms of their pixel co-ordinates using the equations from Pirat et al. [39]:

$$\gamma_1 = \arcsin\left(-\frac{x^5_{x1}}{x^4_{y1}}\cos(\alpha)\right) - Az_1 \tag{4.12}$$

$$\gamma_2 = \arcsin\left(-\frac{x^5_{x2}}{x^4_{y2}}\cos(\alpha)\right) - Az_2 \tag{4.13}$$

In these two equations, x^5_{x1} is the original x co-ordinate of LED 5, x^4_{y1} is the original y co-ordinate of LED 4, x^5_{x2} is the x co-ordinate of LED 5 in the pixel shifted frame, x^4_{y2} is the y co-ordinate of LED 4 in the pixel shifted frame, Az_1 is the azimuth of the pattern in the original frame and Az_2 is the azimuth of the pattern in the pixel shifted frame. The layout of the LEDs can be seen in Figure 4.6. No roll is added between frames, therefore $\cos(\alpha) = 1$. A yaw rotation of the pattern also only changes the x co-ordinate of LED 5 as the pattern pivots about the axis going through LED 4 and the centre of the pattern. Therefore, LED 4's y co-ordinate and the azimuth of the pattern do not change between the frames. Finally, between the two frames, the x co-ordinate of LED 5 is only changed by one pixel. Thus, the above equations can be combined and written as:

$$\delta = \arcsin\left(-\frac{x^5_{x1}+1}{x^4_{y1}}\right) - \arcsin\left(-\frac{x^5_{x1}}{x^4_{y1}}\right) \tag{4.14}$$

To find the theoretical angle change, a sample point is used from test data. A test point at a distance of 250 mm (the same distance as both tests that yielded Figures 4.9 and 4.10) was selected. This point has the co-ordinates $x^5_{x1} = 15.9236$ and $x^4_{y1} = -25.9186$ and thus $\delta = 0.0499$ rad. This is close to the value of the jumps seen in Figure 4.9 thus reinforcing the pixel shift hypothesis.

This is believed to be due to the point spread nature of the pixel's light, the normal light distribution, not being taken into account when the pixel is added to the blob, i.e. only the co-ordinate values are used which shifts the centroid by a greater value than if a weighted value was added.

4.2.3.2 Improved Solution

An improved blob detector was used to improve the accuracy of the blob detector results. This new blob detector was based off the region growing algorithm in Erlank [40] and the centroiding algorithm in Erlank and Steyn [41].

The region growing algorithm starts by scanning each row of the image for pixels that exceed a set threshold. Not every pixel needs to be searched as the LEDs are expected to exceed a single pixel in size, therefore every second or third pixel is checked. Once a pixel is found that exceeds the threshold, the 4 adjacent pixels are checked. This process is continued from each new pixel until no further pixels are found that exceed the threshold. The position and pixel value of each of these connected pixels is stored in an object. Each new region found is placed into a new object. For an LED detection to be considered valid, the region must exceed a certain number of pixels i.e. the region must be greater than a set minimum size. This is implemented to avoid dead pixels damaged by radiation and lessens false detection due to noise from large analogue-to-digital gain values. Small regions also have the added problem of producing less accurate centroids as there is less pixel data to work with. The centroid of the detected LED is calculated using a simple centre of gravity equation: the pixel value of each pixel is multiplied by the pixel's co-ordinates. These values are summed together and divided by the sum of all the pixel values.

This algorithm improved the results substantially. A graph of the yaw angle with the new blob detector can be seen in Figure 4.10. The one downside of this method is that the new solution tends to be slower than OpenCV solution, at least when only a single pass is used with the OpenCV solution.

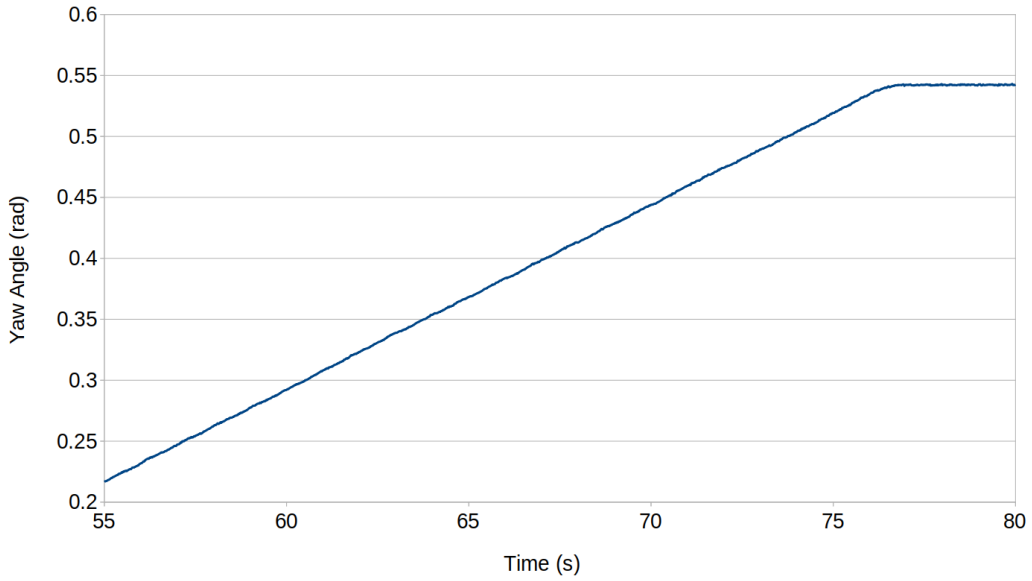

Figure 4.10: Graph of the yaw angle with the new blob detector.

To improve the processing time of the new method, the blob detector was programmed with two modes: a search mode and the tracking mode. In the search mode, the blob detector searches the entire image for LEDs. This takes a lot of processing time and an average frame rate of about 40 FPS was achieved. Once all the expected LEDs, and no additional regions, are found, the blob detector moves into tracking mode.

In tracking mode, the blob detector only searches a small area around the last centroid of the LED. This is performed for each of the 5 LEDs. This greatly reduces the number of pixels that need to be searched improving the processing time significantly. A frame rate of approximately 110 FPS was achieved once this windowed searched was added. This thus satisfies the specification of 100 Hz sampling for the pose estimator.

One aspect to note is that, if the target is moving very rapidly, the LED may move outside of the search area leading to the LED not being found. This was determined to not be an issue as at 110 FPS, the target would need to be moving faster than could realistically be achieved on the test facility and thus this case would not come into play. Motion blur would also become a much larger problem than the search area at this point. Finally, should an LED be lost when in tracking mode, the system will move back into search mode to find all the LEDs once again.

4.2.4 Filtering

A simple low-pass filter was implemented to smooth the angle and position data. The implemented filtering function can be seen in equation .

$$\theta_2 = \alpha \cdot \theta_{meas} + (1 - \alpha) \cdot \theta_1 \tag{4.15}$$

where θ_t is the angle value at time t, α is the filter weight and θ_{meas} is the measured angle value from the pose estimator. It was found during testing that, once the new blob detector was implemented, the data was smooth enough that the filtering did not aid in the accuracy of the system.

4.3 Testing

A number of tests were setup and performed in order to determine the correct operation and the accuracy of the pose estimation system. Firstly the pose estimator algorithm was tested followed by the distortion correction algorithm. The two systems were then combined and the complete system was then tested. The complete system test is performed to ensure that the pose estimator can determine a targets pose with accuracy better than the specifications set out in Section 3.2.

4.3.1 Pose Estimator Functionality

In order to test the pose estimator on its own, an image of the target without any lens distortion was needed. Any lens distortion would need to be corrected otherwise it would impact the accuracy of the pose estimation. The correction could also impact the results of the pose estimator should the model used not completely account for all distortions. This individual test would also provide insight into the limitations of the pose estimator. Thus, testing the pose estimator in isolation was deemed necessary.

The easiest way to achieve this was to use some 3D modelling software to generate test images of the target. A model 1U cubesat was modelled in Blender, an open-source, 3D modelling program. The target was added to one of the faces of the cubesat. The remaining faces were modelled to simulate solar panels. This was to check whether the blob detector would correctly detect the LEDs without also detecting reflections off the solar panels. A star field was also added to the background of the image to further test false detections in the blob detector.

The cubesat images were generated with the cubesat in various positions and rotations. These images were generated with pure translations in each axis, pure rotations in each axis and then a combination of both. This was intended to test each of the rotation and translation calculations and then all 6 degrees of freedom.

The virtual camera within Blender has a horizontal FOV of 39.6°, a focal length of 50 mm, a resolution of 1920 X 1080, and a sensor size of 36 mm x 20.25 mm. Importantly, Blender does not simulate lens distortions on this camera. The cubesat was placed 1 m from the camera. The LEDs were spaced 40 mm from the pattern centre. Examples of the images generated can be seen in Figure 4.11.

These images were passed through the pose estimator. The outputs where printed to the image and this image was stored. To get a benchmark, an image without any applied rotations or translations was first tested. The results of this can be seen in Figure 4.12. In the figure, Alpha is the roll angle, Beta is the pitch angle and Gamma is the yaw angle. The range, azimuth angle and elevation angle are all shown as well. Finally, the blue circle indicates the calculated centre-point of the pattern, the red circles are the detected blobs, and the red lines bisect the horizontal and vertical image axis i.e. it is the image centre.

The output of this test suggests fairly good results. The angles, all of which are expected to be 0°, are all within 0.3° of the expected. The range is

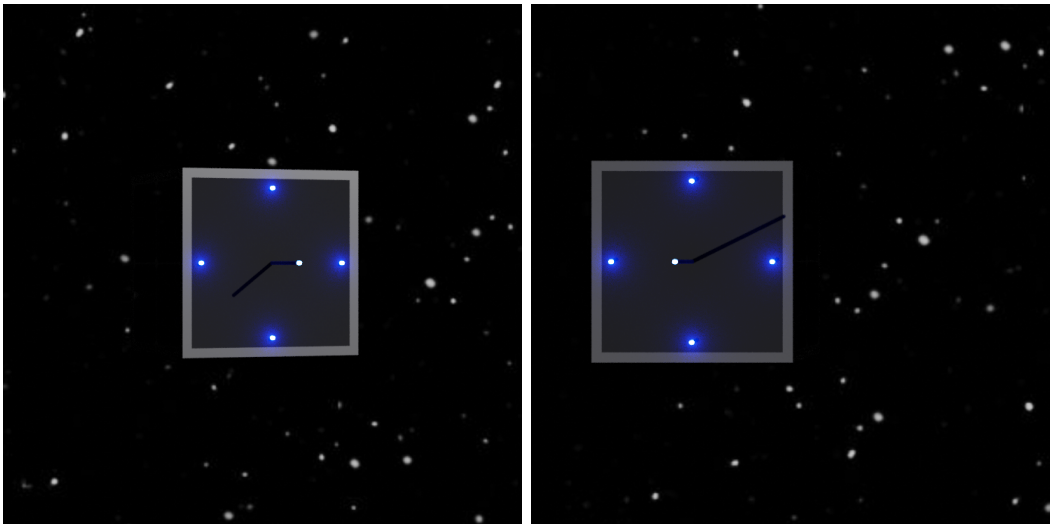

Figure 4.11: Image generated with a yaw angle of 20° (Left) and a 0.2 m translation to the left (Right).

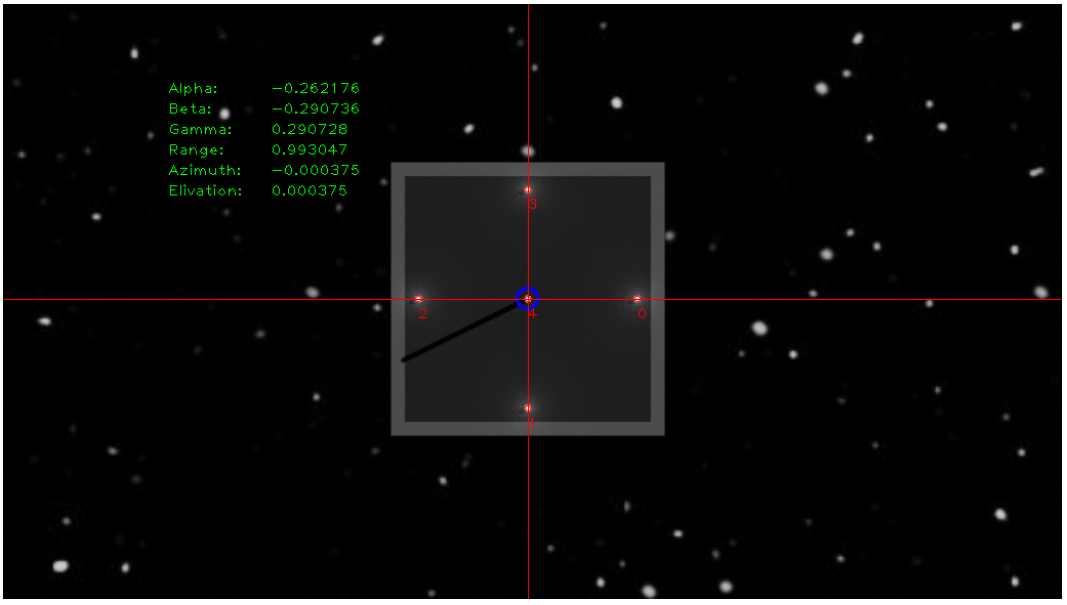

Figure 4.12: Output of pose estimator without any rotation.

within 10 mm of the expected value and the azimuth and elevation values are approximately 0°.

The accuracy of the pose estimator decreases somewhat in the actual pose tests. Two example outputs can be seen in Figure 4.13. Two noticeable changes in accuracy in the left image is in the yaw and range values. The yaw accuracy in this image is approximately 2° and the range accuracy drops to approxi-

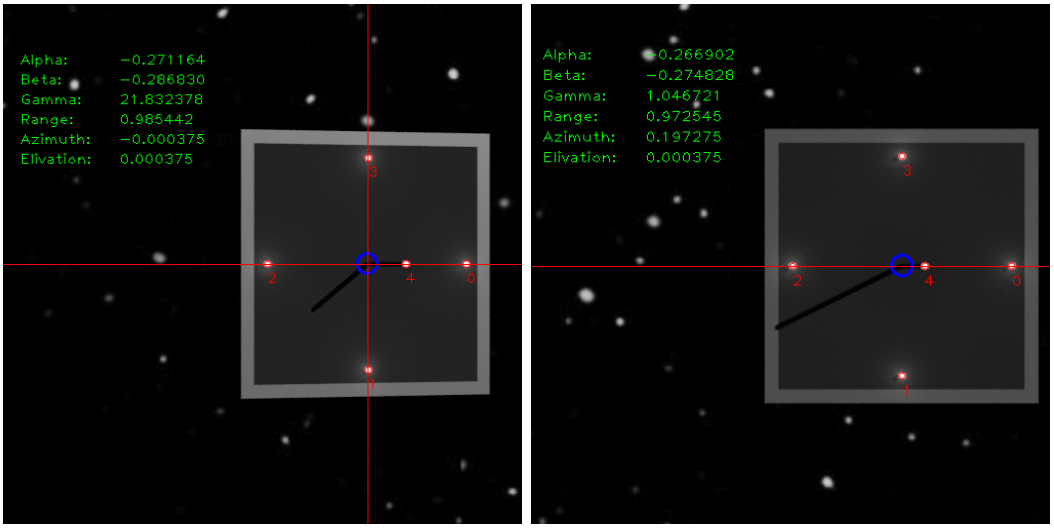

Figure 4.13: Output of pose estimator with a yaw angle of 20° (Left) and a 0.2 m translation to the Right (Right).

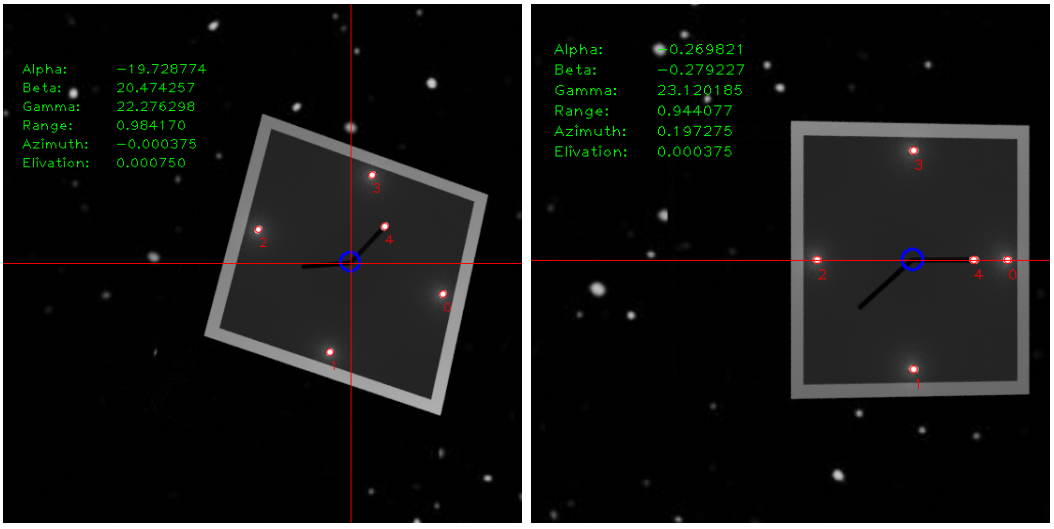

Figure 4.14: Output of pose estimator with a 20° rotation about each axis (Left) and a 0.2 m translation to the right with a 20° yaw rotation (Right).

mately 15 mm. In the right image, the range accuracy is further reduced to 30 mm. This reduction in range accuracy seems to correspond to shifts in the yaw angle or translations in the horizontal direction. The error in the azimuth angle remains approximately 0.

Testing the pose estimator with multiple rotations or translations shows that the pose estimator can properly handle such cases with a similar loss of accuracy as with the single rotation or translation cases. Some sample outputs

from these tests can be seen in Figure 4.14. In the right hand image of this figure, the range accuracy is further reduced from the pure translation case. This seem to be due to the added yaw rotation which confirms that the range value accuracy reduces with both translations and rotations. This error is believed to be caused by the fact that linear translations and pure rotations can produce the same movement in LEDs leading to errors in the measurements. This phenomenon should be corrected by the correction factors in the pose calculations however it is likely that it cannot completely correct the errors. This is further discussed in Pirat et al.[39]. The EKF implementation should provide better results in these cases.

During testing with the generated images, it was found that the pose estimation algorithm is very sensitive to the distance of the out of plane LED from the pattern centre. A shift of 1.5 mm changes the range result by approximately 7 mm. It was thus determined that care had to be taken when building the prototype marker.

4.3.2 Distortion Correction Functionality

As mentioned in Section 4.2.1, a method from the OCamCalib toolbox was ported to C++ in order to correct the distortion in the images. To ensure that this method was correctly ported, this undistort method was tested on a captured image. The distorted image can be seen in Figure 4.15.

The output generated by the distortion correction code can be seen in Figure 4.16. From this figure, the lines within the chequerboard have been straightened by the correction algorithm confirming that the distortion correction algorithm functions correctly. It can, thus, also be assumed that the calibration values in the calibration file are also correct and thus can be safely used within the final system code.

The method used to undistort the entire image could unfortunately not be used on singular points and correcting the distortion of each image prior to pose estimation would significantly slow down the system. Another method was thus implemented for correcting the distortion of only the centroids of the blobs. This method was again ported from the Matlab toolbox. This method makes use of the *cam2world()* function.

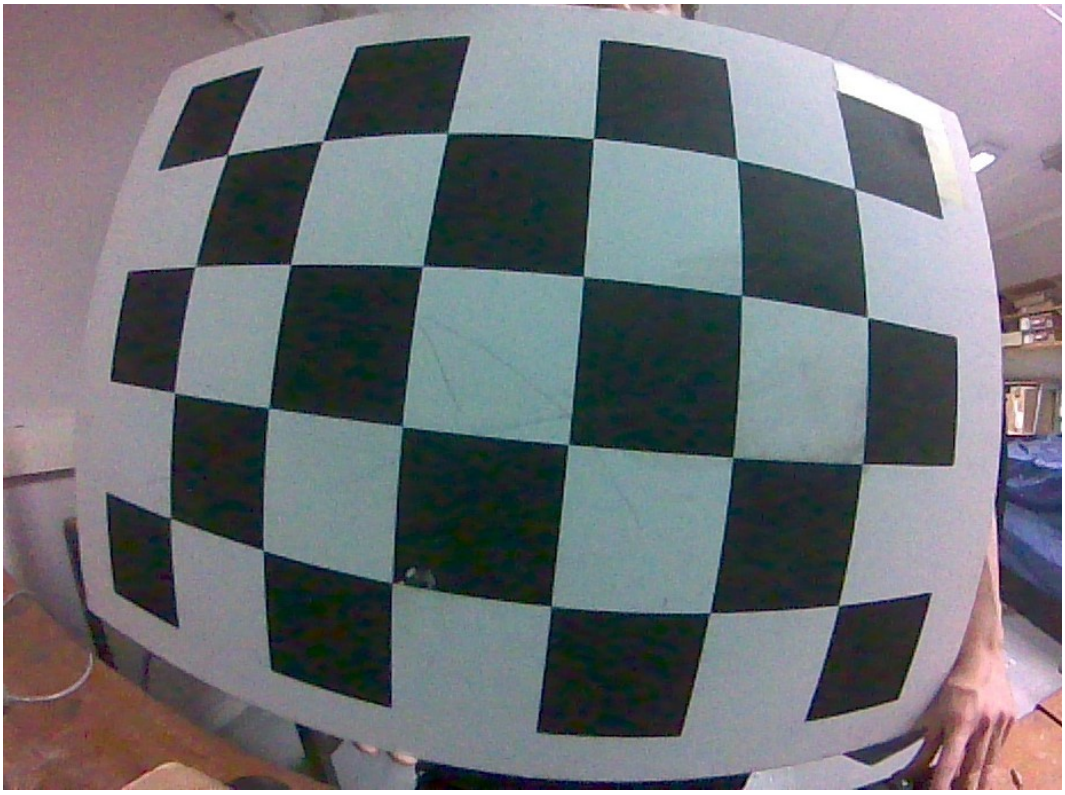

Figure 4.15: Raw image captured with a 200° FOV lens.

4.3.3 Complete System Experimental Setup

4.3.3.1 Rotation Tests

The first set of tests were intended to determine the rotational accuracy of the pose estimation system. To do this, a 3D printed mount is made for the LED target. This mount is then placed on an Ideal Aerosmith 1270VS single axis rate table. The rate table can be controlled using a RS-232 serial interface via USB to a computer. This allows the rate table to be rotated to set angles at set speeds with a theoretical accuracy of 0.000 031 25° [42]. The camera was then placed at a set distance from the LED target such that the centre of the pattern was in the centre of the image with no yaw rotation relative to the camera. The rate table was set such that this position would be defined as 0°. The pattern was then rotated from −30° to 30° at various speeds, namely 50 °/min and 100 °/min. The test was repeated at two distances from the camera, 250 mm and 500 mm.

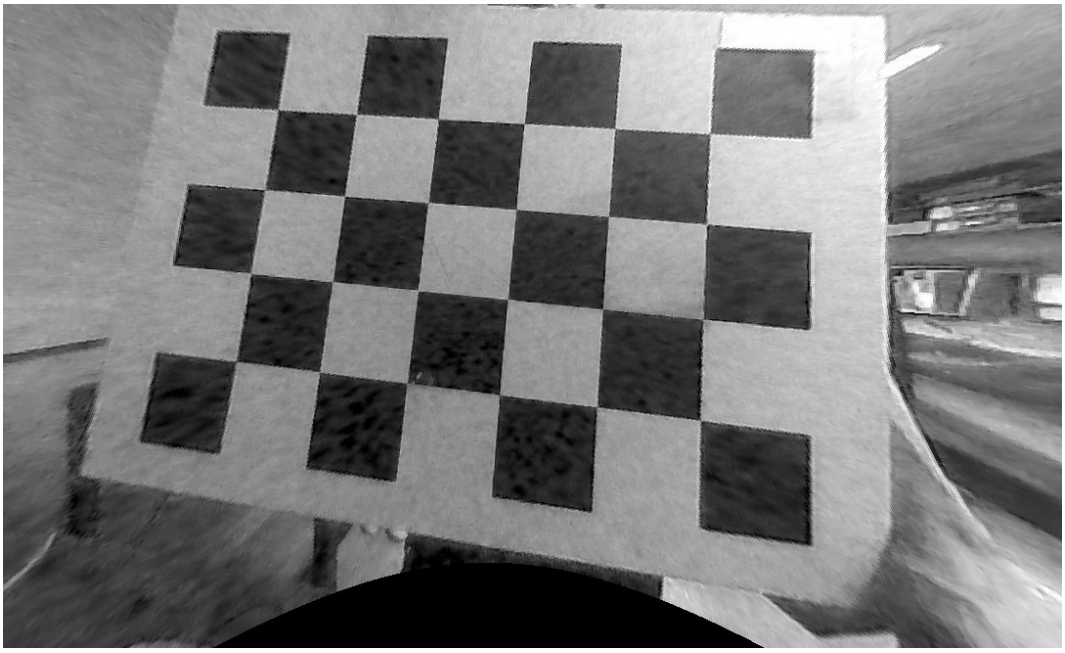

Figure 4.16: The distortion corrected image.

4.3.3.2 Translation Tests

To determine the translational accuracy of the pose estimator, the LED target was placed on a flat surface on a line perpendicular to the camera bore-sight axis at a set distance, D. The centre of the perpendicular line, where the bore-sight axis intersects it, is marked as 0 mm. The target was then moved by some distance, L_T, in 25 mm increments along the perpendicular line from -125 mm to 125 mm. The azimuth angle, the angle between the bore-sight axis and the centre of the pattern, θ, was then measured. This test was repeated at two distances, 250 mm and 500 mm. A diagram of the test setup can be seen in Figure 4.18.

The LED target was moved by hand along a straight-edge and thus the accuracy of this experiment is only as good as the accuracy with which the target can be placed by hand ($\pm$1-2 mm).

4.3.3.3 Range Tests

Similar to the translation tests, the range accuracy was determined by placing the target on a flat surface, on a line co-axial with the bore-sight. The range of the target, R, was increased in increments of 50 mm from 250 mm to 750 mm. During the entire test, the target was kept perpendicular to the bore-sight axis (yaw angle of 0°). A diagram of the test setup can be seen in Figure 4.19.

Figure 4.17: Ideal Aerosmith 1270VS. [42]

The target was again placed by hand and kept perpendicular using a straight-edge. The accuracy of the experiment is thus also determined by the accuracy with which the target can be placed by hand (±1-2 mm).

4.3.3.4 Offset Tests

During testing, it was noticed that the accuracy of the pose estimator was very sensitive to the placement of the target within the centre of the image. Thus, three further tests were conducted to quantify the change in accuracy when the target is moved away from the image centre.

The first of these tests was performed similar to the rotation test, however, the target was offset from the centre of the image. The target was offset such that the perpendicular distance, D, remained 250 mm and the azimuth angle, θ, was 0.25 rad. The target was then rotated from $-15°$ to $15°$, α, at a rate of 50 °/min. The smaller rotation angle of the test was due to the right most LED being obscured by the central LED stand-off when a larger angle was used. A diagram of this test can be seen in Figure 4.20.

The second test was performed similar to the range test, however, the target was moved on an axis parallel to- and offset from the bore-sight axis. A perpendicular offset, D, of 130 mm was used. The target was again move by some distance, L_R, in increments of 50 mm from 250 mm to 750 mm. A diagram of this test can be seen in Figure 4.21. This test is subject to the same

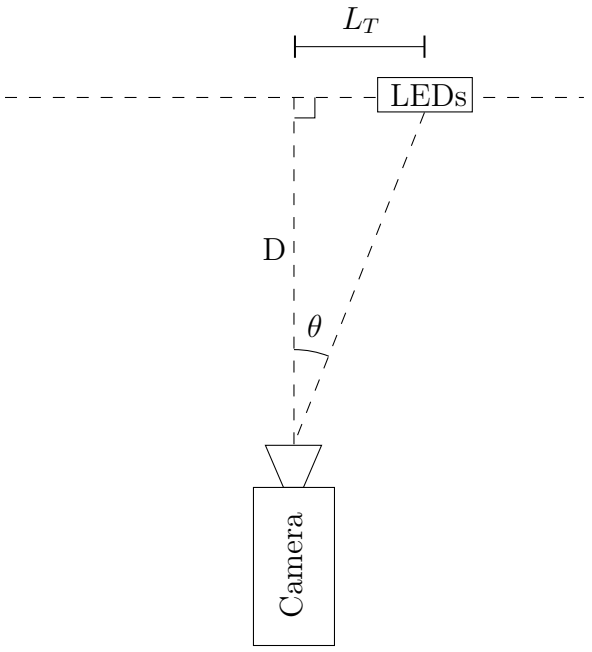

Figure 4.18: Diagram of the translation test.

accuracy as that of the in-line range test.

The final test was a repetition of the translation test at 4 distances, both with and without distortion correction. This test was intended to quantify the extent to which the distortion correction was able to correct the lens distortion.

4.3.4 Results

The RMS values below were calculated as:

$$RMS = \sqrt{\frac{\sum_{i=1}^{N}(x_i - \mu_i)^2}{N}} \tag{4.16}$$

where x is the measured value from the pose estimator, μ is the actual value, and N is the number of collected data points.

The maximum error is the largest error between the measured and actual values in the dataset.

4.3.4.1 Rotation Tests

The pose of the target was sampled at the frame rate of the camera module (110 Hz). The sampled points were then plotted versus time. The raw mea-

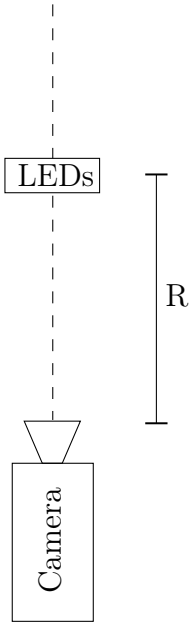

Figure 4.19: Diagram of the range test.

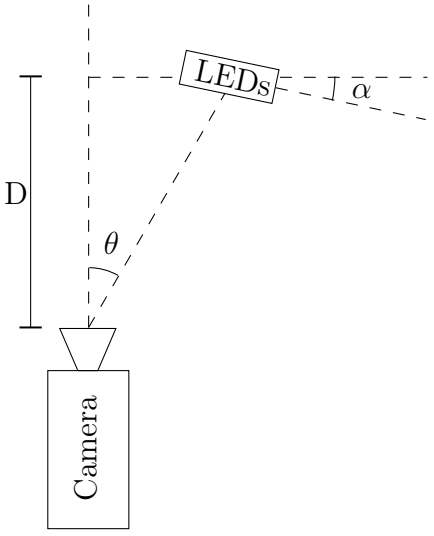

Figure 4.20: Diagram of the offset rotation test.

sured angle, the filtered angle and the expected angle were all plotted. An example plot can be seen in Figure 4.22. The RMS and maximum error of the tests were calculated. These results are tabulated in Table 4.1 and 4.2.

Taking the worst value obtained, the maximum error of the 500 mm, 50 °/min test, an accuracy of 0.0520 rad (2.979°) is obtained. This is much better than the allowable misalignment of the docking adapter of 5°.

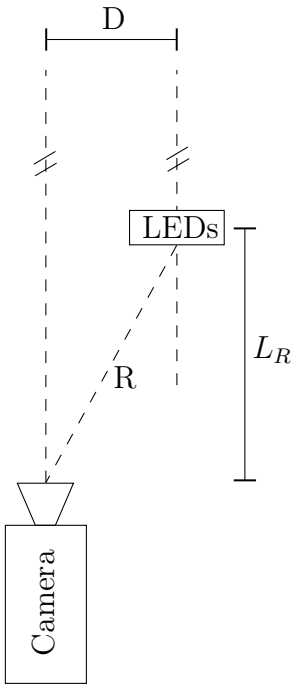

Figure 4.21: Diagram of the offset range test.

Distance (mm)	Rotation Rate (deg/min)	Raw RMS error (rad)	Filtered RMS error (rad)
250	50	0.0092	0.0094
250	100	0.0088	0.0112
500	50	0.0265	0.0262
500	100	0.0259	0.0264

Table 4.1: RMS error of inline rotation tests.

An interesting observation that can be drawn from these results is that the accuracy of the system decreases as the markers move away from the camera, i.e. as the two satellites separate. This is possibly due to the smaller area of the image taken up by the LEDs. The size of the LED blobs would also decrease with increasing distance. This results in the error of the centroids of the LEDs increasing relative to the separation of the LEDs from each other. This affects the accuracy as the angle is calculated based on this separation. This reduction in accuracy can, again, be seen by the greater deviation of the measurements from the expected results in Figure 4.23 than in Figure 4.22.

Another observation that can be made is that of the noise at various distances. As seen in the RMS values from Table 4.1, the RMS of the error increases as the distance increases suggesting larger variation in data at larger

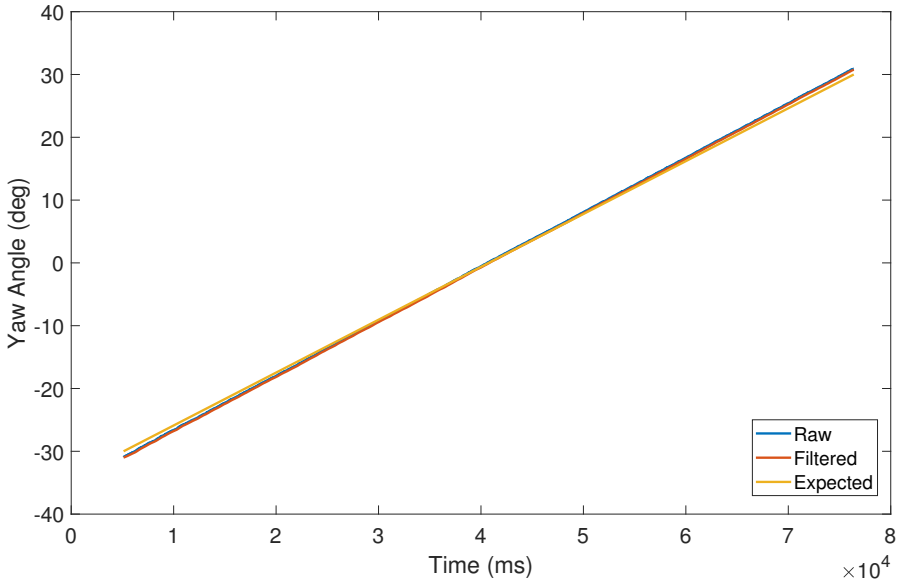

Figure 4.22: Plot of the measured yaw angle, filtered yaw angle and expected yaw angle at a distance of 250mm.

Distance (mm)	Rotation Rate (deg/min)	Raw Max Error (rad)	Filtered Max Error (rad)
250	50	0.0172	0.0194
250	100	0.0172	0.0225
500	50	0.0520	0.0470
500	100	0.0471	0.0486

Table 4.2: Maximum error of inline rotation tests.

distances. This can be seen in Figure 4.23. The measured data has more noise and the periodic shifts in the measurements with changing LED position start to become more pronounced.

Another important observations is that the accuracy of the angles measurement seems to be independent of the rotation velocity. As seen in Table 4.1, the RMS value does not change substantially between the 50 °/min and the 100 °/min tests.

From the data, it can be seen is that the filtering of the data is not necessary and can actually be detrimental to the results. In Table 4.1, in all but one case, the filtered data RMS value was higher than the raw measurements. This is due to the lag introduced by the filter shifting the measured value away from the expected value at a specific time instance. There is also very little

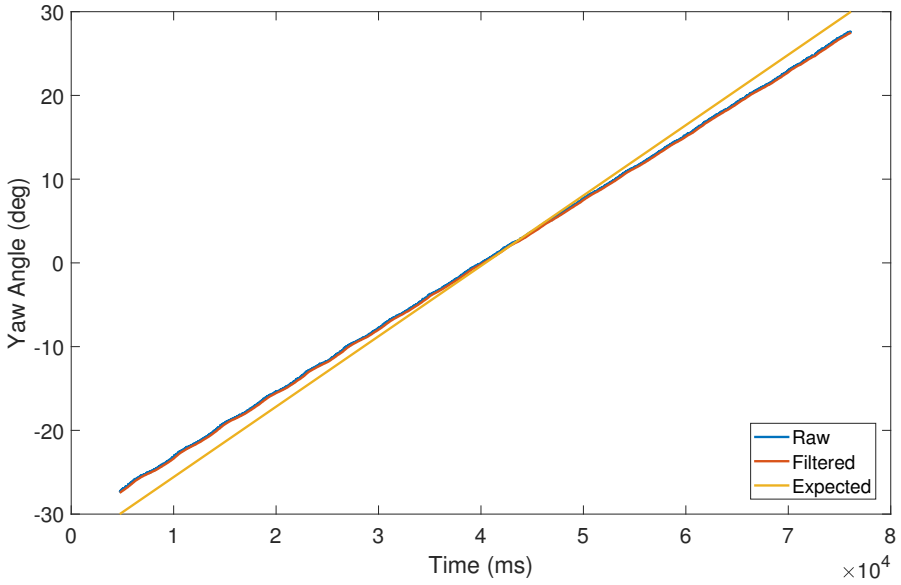

Figure 4.23: Plot of the measured yaw angle, filtered yaw angle and expected yaw angle at a distance of 500mm.

noticeable difference between the raw and filtered data in either Figure 4.22 or 4.23.

The rotation rates for each of the tests was also measured and the RMS value, mean rate and maximum error was calculated. An example graph of the rate results can be seen in Figure 4.24. The calculated results are tabulated in Table 4.3.

Distance (mm)	Rotation Rate (deg/min)	Mean (deg/min)	Standard Deviation (deg/min)	Maximum Error (deg/min)
250	50	52.036	2.4065	6.4225
250	100	104.086	4.4413	8.2390
500	50	46.058	5.2068	12.6547
500	100	92.300	8.0692	14.9423

Table 4.3: Rotation rates from inline rotation tests.

The rate results show promise with the standard deviations of all the results being below the 12 °/min design specification. An important observation that can be made is that the accuracy of the rate measurements tends to increase with decreasing angular rate as well as decreasing distance. Both these observations are important as a satellite would be trying to minimise the rotation

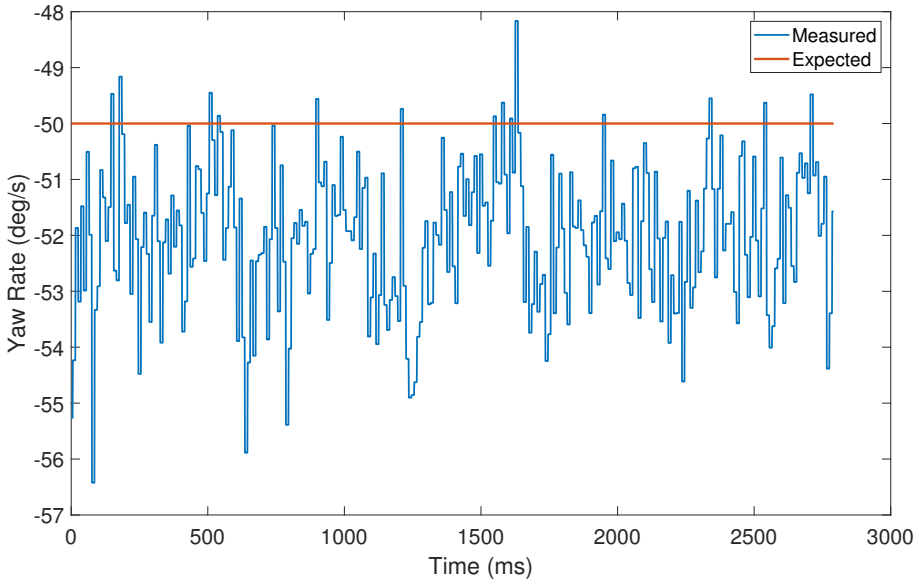

Figure 4.24: Plot of the measured yaw rate, filtered yaw rate and expected yaw rate at a distance of 250mm.

rate when attempting to dock. Further the satellite would be approaching the other, thus, the rate measurement is expected to improve in accuracy as the two satellites close distance. This is ideal as the closer the satellites get, the more accurate the pose estimator should be.

The offset in the rate average seen in Figure 4.24 is believed to be due to the slight offset seen in the slope of the rotation data. This is confirmed as in Figure 4.22 the slope is slightly steeper than the expected slope and the mean rates are slightly larger than the expected. In Figure 4.23, the slope is slightly shallower than the expected slope and the mean rate is less than the expected. These discrepancies are believed to be caused by the calibration distance of the system. The system's rotation values were calibrated at 300 mm and as mentioned above, the accuracy of the system decreases with distance. Thus, when the distance is below the calibration distance, the slope is expected to be higher and slowly drops below the expected slope after the calibration distance.

As mentioned in Section 4.2.2, a very simple, moving-window average is used to calculate the velocity values. A more sophisticated velocity determining algorithm, such as a least squares regression or the EKF approach, could be used which has the potential to greatly improve the rotation rate measurement accuracy.

4.3.4.2 Translation Tests

The translation tests were used to find the accuracy of the azimuth angle calculation. This angle would then be used to find the relative translational distance of the target from the imaging satellite using the measured range. The measured azimuth angle was continuously recorded yielding a graph such as that seen in Figure 4.25. Each of the plateaus is one of the incremental points at which the target was placed. The average of each of these plateaus was calculated. These averages where then compared to the expected values to find the RMS and maximum error values. These results can be seen in Table 4.4.

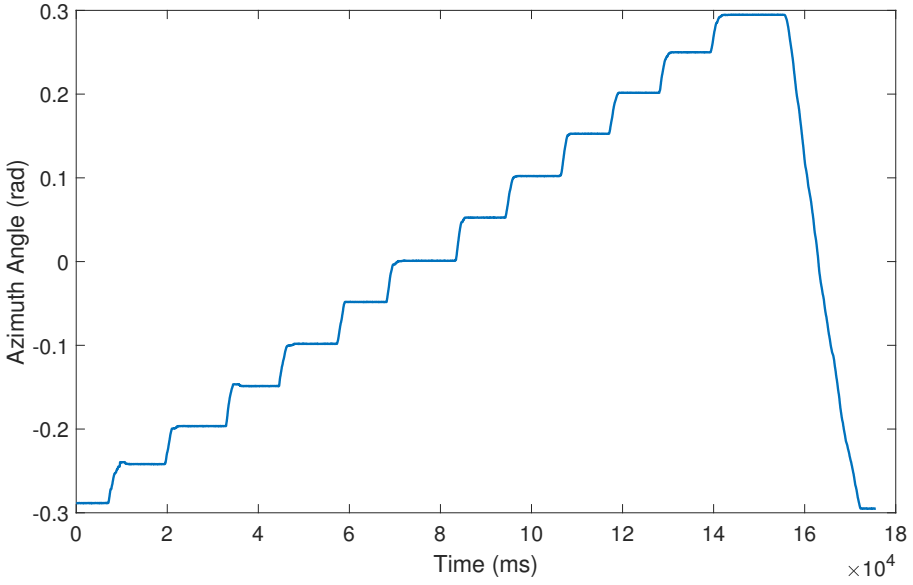

Figure 4.25: Plot of the measured azimuth angle at 500mm.

Distance from boresight (D) (mm)	azimuth angle (θ) RMS error (rad)	Maximum Error (rad)
250	0.00849	0.0132
500	0.00285	0.00499

Table 4.4: Results of the perpendicular translation tests stated as azimuth angles.

The translational positional accuracy of the pose estimator can be found using trigonometry as the distance of the target from the camera is know. The measured azimuth angle and the movement increments are also know. Using

these, the maximum RMS seen is 2.123 mm and the maximum error seen is 3.300 mm.

Again, this is far better than the 10 mm accuracy set out in the docking specification. An interesting observation in the data is that, contrary to the rotation tests, the azimuth accuracy increases with increasing distance. This discrepancy is believed to be due to the different method used to calculate the azimuth vs the other pose values. This suggests that a method that uses only the LED position vectors might improve the results of the pose estimator.

4.3.4.3 Range Tests

Similar to the translational test, the range of the markers was continuously recorded during the range test. This yielded the graph seen in Figure 4.26. Again, the average values of the plateaus were calculated and used to determine the RMS and maximum errors. A plot of these averages compared to the expected values can be seen in Figure 4.27

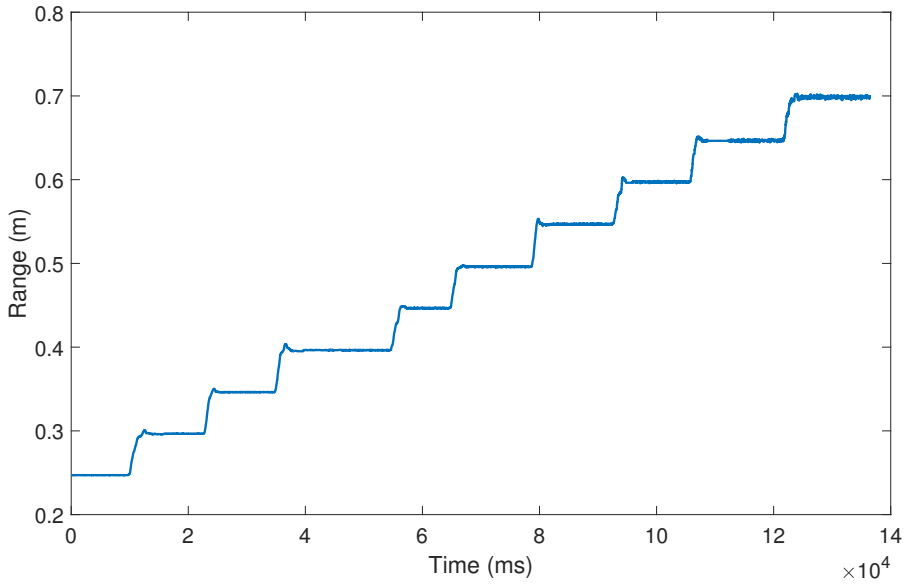

Figure 4.26: Plot of the measured range with the markers inline.

As seen in Figure 4.27, the measured results follow the expected results very well. The slight error in the measured value can also be further removed by adjusting the calibration factor as the results form a straight line. The results from this test yielded an RMS of 3.23 mm with a maximum error of 4.093 mm. Combining these results with the results of the translational test,

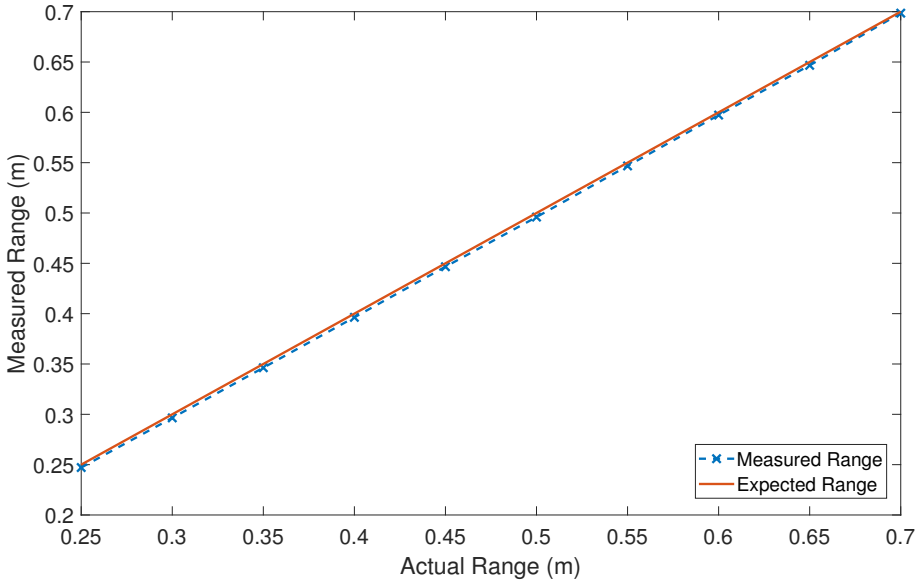

Figure 4.27: Plot of the average measured range with the markers inline.

a preliminary result for the positional accuracy of the system can be calculated. The position of the markers is thus confidently known within a circle with radius 3.865 mm around the expected location. This is far better than the 10 mm positional accuracy set out in the specifications.

4.3.4.4 Offset Tests

A graph of the offset rotation test results can be seen in Figure 4.28. From this figure, it can be seen that the measured yaw angle and the actual yaw angle differ quite substantially. The initial error at the start of the rotation is 1.5743° but steadily increases over time to an error of 4.0259°.

This relatively large error is believed to be caused by a limitation of the pose estimation calculations themselves. As was seen in the initial pose estimator tests with the 3D generated images, the accuracy of the pose values deteriorated with rotations and translations. A relatively large 3.5° error was seen in the values with a 200 mm translation. It can be safely assumed that the error would increase with increasing FOV. Thus smaller shifts produce larger errors.

Another explanation for this relatively large error is believed to be caused by the distortions introduced by the camera lens and made worse by the slight errors introduced by the pose estimator itself. The distortion correction algorithm attempts to remove the distortions however, due to the large FOV, it may not be able to remove the very large distortions present in the image,

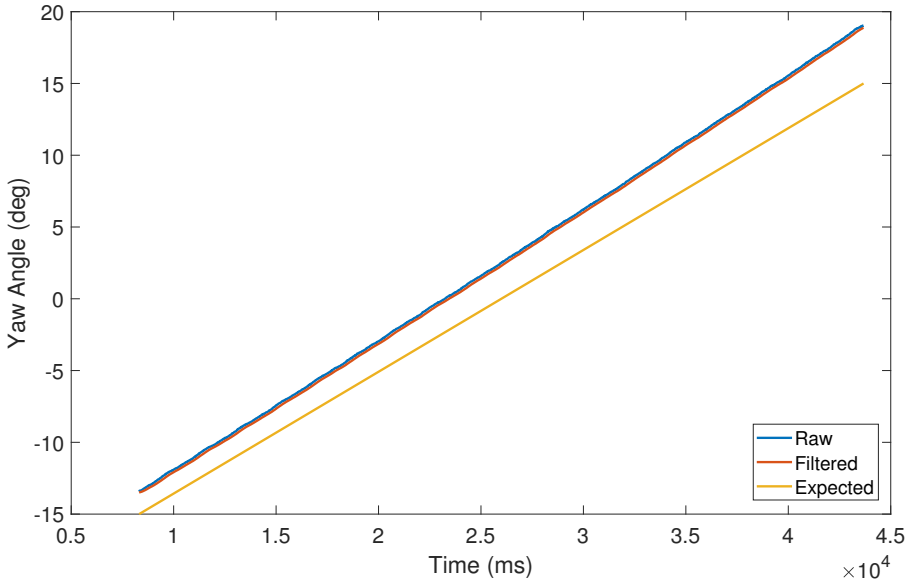

Figure 4.28: Plot of the measured yaw angle, filtered yaw angle and expected yaw angle at a distance of 250mm with a 0.25rad perpendicular offset.

especially near the edges of the image. Further, this correction algorithm assumes a camera model that may not properly capture all of the lens properties thus preventing full correction.

This deterioration in precision can again be seen in the results of the offset range test. A graph of the measured range compared to the actual range can be seen in Figure 4.29. Here the error of the range averages vs the expected results is much larger than in Figure 4.27. The general straight-line trend in the averages seen in Figure 4.27 now takes on a more curved profile meaning the loss in accuracy is greater closer to the lens. This, again, could be due to the distortion induced by the lens being greater at the edges of the image and the closer the target is to the camera, the closer it is to the edge of the image frame. This is also exacerbated by the loss of accuracy of the range value in the pose estimator calculations again seen in the initial pose estimator tests.

The RMS value of this test yielded a results of 57.493 mm. This is a significant reduction in accuracy compared to the in-line range test. This reduction in accuracy is not ideal, however, for a first iteration prototype, this is not a major issue as the satellites would likely line up such that the target is close to the centre of the image, where the accuracy is much better, prior to the approach.

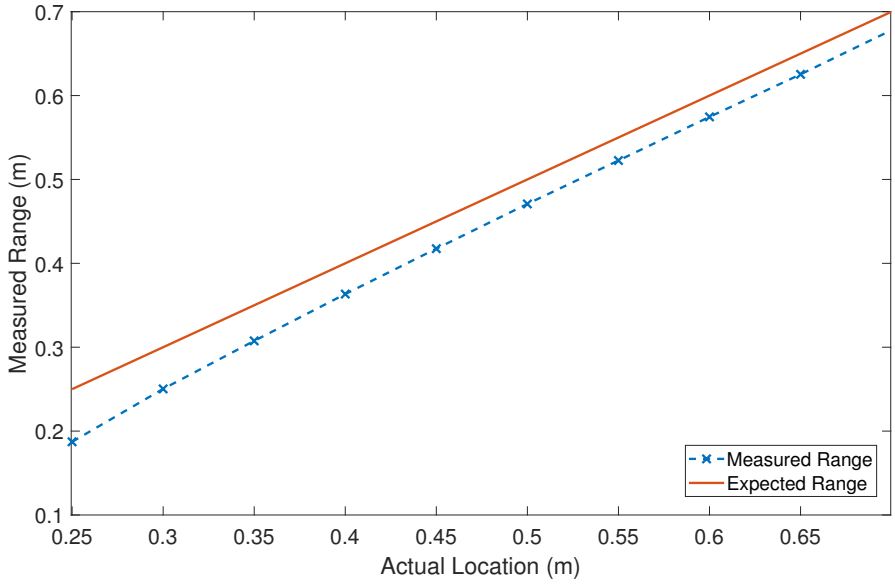

Figure 4.29: Plot of the measured range averages vs the expected averages with the markers offset from the boresight axis.

Another side effect of the loss in accuracy is that the measured yaw angle changes with the range of the target even though care was taken not to rotate the target during the test. This can be seen in Figure 4.30. The error is larger when the target is closer to the camera. This is, again, believed to be due to the larger distortions at the edges of the image and the target being closer to the edge of the image with closer ranges. This is also, again, made worse by the loss of accuracy in the pose estimation calculations.

The absolute errors obtained from the repeated translation test can be seen in Figure 4.31. From this figure, it can clearly be seen that the undistorted measurements are more accurate over the translation range than those without distortion correction. Further, because the target was placed by hand, a placement accuracy of about $\pm$1-2 mm can be expected. At a distance of 200 mm, this yields a maximum azimuth angle error of approximately 0.57°. As can be seen in the figure, all the distortion corrected measurements fall within this range whereas those without distortion correction do not. Another observation that can be made is that in general the azimuth angle error remains fairly constant with the distortion corrected measurements whereas the measurements without distortion correction tend to increase as the translation distance increases. This shows that the distortion correction seems to be working fairly well.

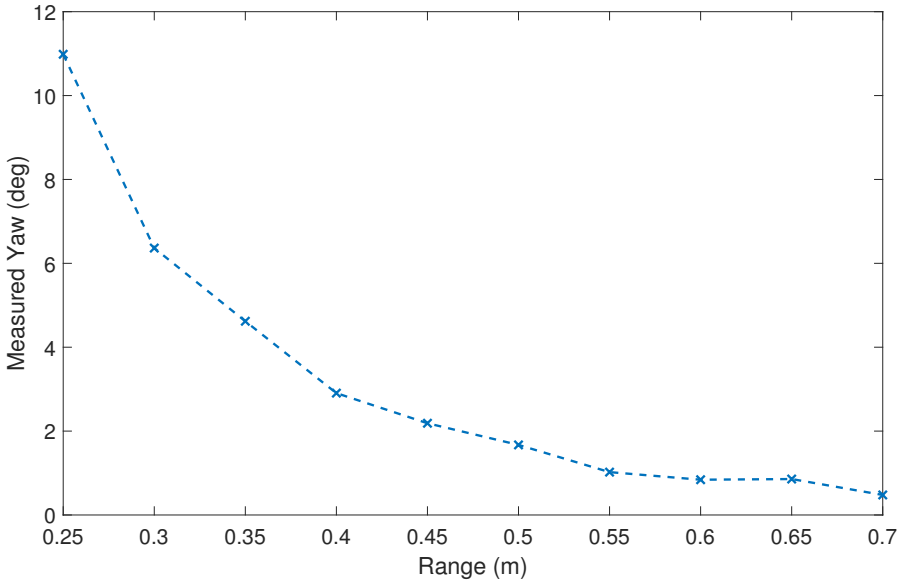

Figure 4.30: Plot of the average yaw angles measured at each of the range increments.

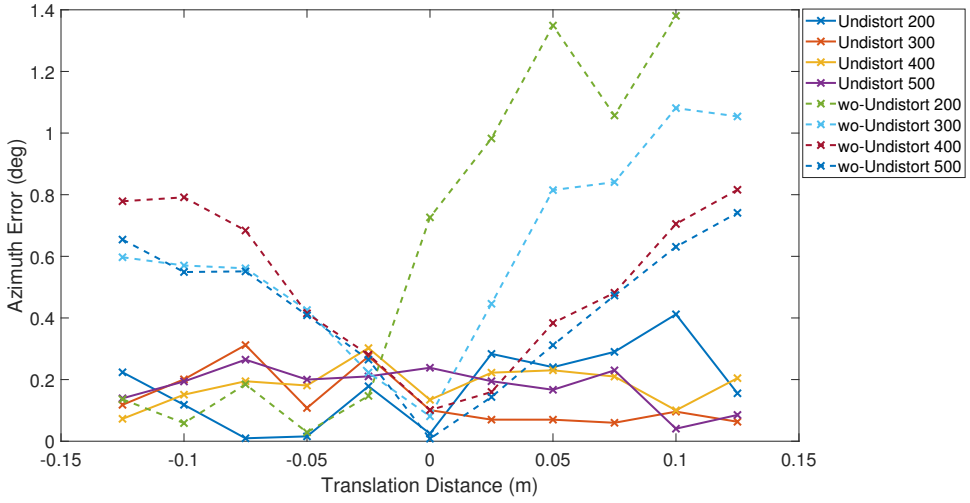

Figure 4.31: Plot of absolute azimuth errors with and without distortion correction at various distances.

It can thus be concluded that the majority of the error introduced in the measurements are most likely due to the way in which the pose values are calculated from the pixel values. The results from these translation tests seem to be quite good and these were the only values calculated using a different method than those set out by Pirat et al.[39]. Thus, potentially basing all pose

calculation on the unit position vectors of the various blobs may provide much more accurate results.

Chapter 5

Docking Mechanism

For this project, three docking concepts were investigated. Each concept was based off a different mechanism with one of them based off of a flown docking module. This section discusses the workings of each of the mechanisms as well has the manufacturing considerations determined from the prototype module.

5.1 Rotating cam

5.1.1 Design

The first concept mechanism is the rotating cam mechanism. A diagram of this mechanism can be seen in Figure 5.1. This mechanism is a probe-and-drogue design based off the clicking mechanism used in some ball point pens. This latching mechanism employs a plunger with a rotating cam. When the plunger pressed the cam is rotated. This rotation causes the cam mechanism to engage with a fixed catch. This prevents the cam from returning to its original position.

For the docking mechanism, this latch was extended such that one side of the docking mechanism contained the rotating plunger and the other side the latching catch. In the mechanism used in the ballpoint pen, the catch also includes a guide that ensures that cam does not rotate prematurely thus preventing the mechanism from getting latched open. On the docking mechanism, a fixed guide, similar to that in ballpoint pens, could not be included as the two sides of the mechanism existed in two separate pieces. To combat this, a sliding guide was added in addition to the plunger and the rotating cam. This guide would engage with the body of the catch side of the docking mechanism and slide out of the way thus allowing the cam to rotate and engage with the catch locking the two spacecraft together.

To meet the design specification for misalignment, the end of the probe was pointed and the edge of the socket was chamfered. The angled faces would guide the probe into the socket in the case where there is some misalignment.

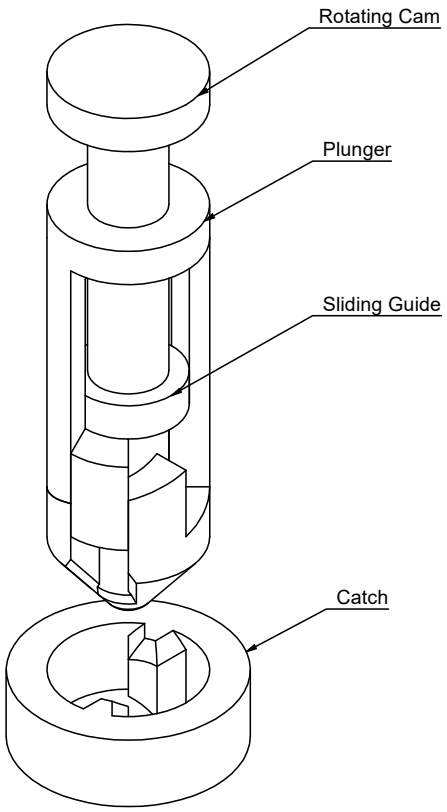

Figure 5.1: Rotating cam mechanism.

5.1.2 Operation

Docking starts with the two spacecraft lining up such that the gate in the cam and the catch are aligned allowing the cam to be inserted into the catch (Figure 5.2, stage 1). The two spacecraft approach each other with the use of thrust from a propulsion system or by making use of electromagnetic attraction. The probe enters into the socket and the sliding guide is pushed up by the catch body. The spacecraft are then held together temporarily by some mechanism such as an electromagnet. The latching mechanism is then activated. The plunger is, first, extended by a servo pushing the rotating cam further into the catch of the other spacecraft (Figure 5.2, stage 2). Once the cam is pushed far enough, the angled surfaces on the plunger and cam cause the cam to rotate 45° (Figure 5.2, stage 3). This causes the cam to engage with catch. The cam is prevented from rotating further by the step before the

next angled section on the cam. The plunger is then retracted, and the cam is allowed to rotate a further 45° into the final locked position (Figure 5.2, stage 4). In this position the cam is fully engaged with the catch and the plunger is in the release position.

The spacecraft are released from each other following a similar method. The mechanism is activated, and the plunger is extended by the servo once again. This pushes the cam mechanism down until the cam can rotate once again (Figure 5.2, stage 5). Again, the angled section on the plunger and cam cause the cam to rotate 90° (Figure 5.2, stage 6). The cam rotates and lines up with the gate in the catch allowing the two spacecraft to separate. As the spacecraft separate, the guide slider moves down to catch the cam and prevent it from rotating further. The mechanism has now made a 180° rotation. Due to the symmetry of the cam, the mechanism is now again in the docking position.

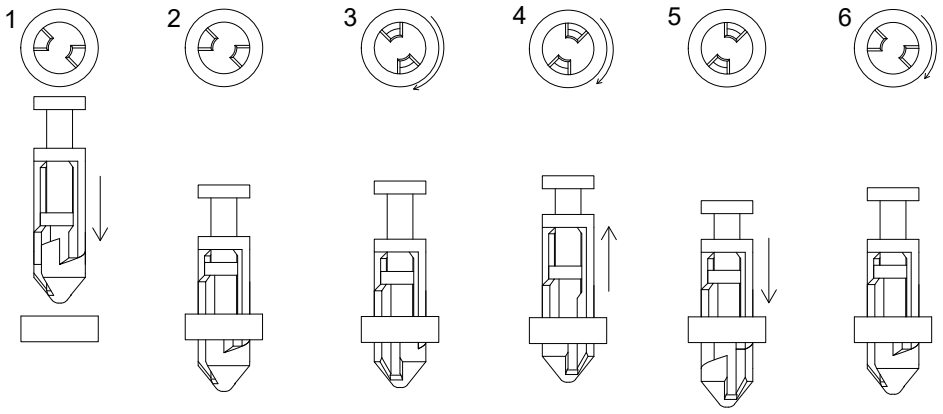

Figure 5.2: Rotating cam mechanism operation.

This mechanism was not pursued passed the concept phase as the springs required to make a prototype of the mechanism were deemed too expensive and too hard to obtain. The mechanism is also fairly complicated and makes use of many sliding parts that have the potential to seize in position preventing the mechanism from functioning. The need for some holding mechanism before the latch is activated is also not very desirable. Finally, the mechanism is not androgynous which makes it less appealing as this impacts the modularity of future missions. The mechanism could be made to be androgynous by having both the cam and the catch on both spacecraft. This is not ideal and thus a different solution was pursued.

5.2 Detent Lock

5.2.1 Design

The ball detent mechanism was inspired by the mechanism employed in pneumatic quick disconnect couplings. This mechanism involves a series of steel balls that protrude partially from a cylindrical housing. The mating part has a groove that these steel balls fit into. Finally, a locking collar fits around the balls to hold them into their detents. To turn this mechanism into an androgynous docking mechanism, the mechanism would have to have both the socket and probe. This is achieved in a similar manner to the UDP adapter used on the SPHERES platform [26]. The probe and the socket of the mechanism are offset from the centre of the mechanism. This allows the probe of the first satellite to insert into the socket of the second and vice versa. As mentioned previously, this is not ideal however a concept was still generated due to its relative simplicity. A diagram of the concept docking mechanism can be seen in Figure 5.3.

A retaining collar is used to prevent the balls from leaving their channels when the locking collar is retracted. For assembly purposes, the retaining collar would need to be removable in order to get the balls into their channels. To achieve this, the collar would be threaded on the end. This would then thread into a socket on the main body that was shallow enough to give access to the channels. This introduces a challenge, however, as access to the locking collar through this retaining collar is needed. Thus the retaining collar needs a groove that must be accurately aligned when installing.

To allow for misalignment, similar to the rotating cam mechanism, the probe would have a pointed tip and the socket would be chamfered. This prototype design is intended to use a single 9g servo to operate the locking collar. This may introduce an issue with binding as the servo operating the collar on one side only will introduce a torque that can cause the locking collar to bind within the retaining collar. For a space-ready solution, multiple smaller servos could be used to actuate the locking collar from multiple points to prevent this torque.

5.2.2 Operation

Docking begins by aligning the two docking adapters (Figure 5.4, stage 1). The locking collars on the two mechanism are retracted allowing the steel balls to move freely within their channels (Figure 5.4, stage 2). The outer retaining collar prevents the balls from fully leaving their channels (Not shown in Figure 5.4). As the two satellites come together, the pointed head of the probe

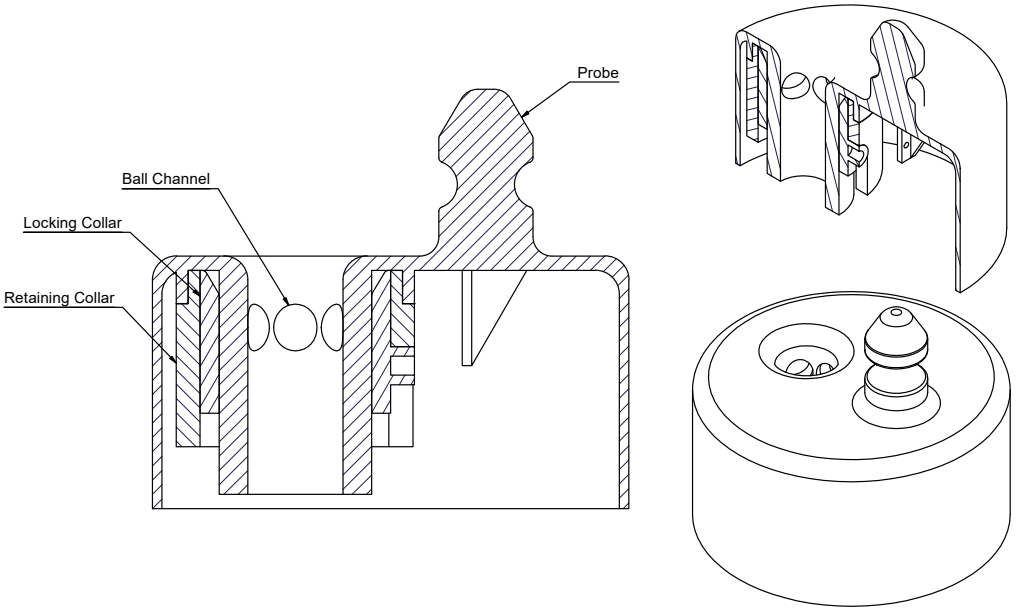

Figure 5.3: Detent Lock Mechanism.

pushes the balls out of the socket and deeper into their channels allowing the probe to move into the socket (Figure 5.4, stage 3). Once the probe is fully inserted, the locking collar is pushed forward again (Figure 5.4, stage 4). A chamfered edge on the collar pushes the steel balls down into the socket. This causes the steel balls to protrude into the socket once again. The groove in the probe locks the probe into the socket once the balls have descended entirely. The retaining collar moves over the balls once they are fully descended preventing the balls from moving back up into their channels (Figure 5.4, stage 5).

The satellites are released by reversing this operation. The locking collar is retracted allowing free movement of the balls. This allows the probe to be pulled out of the socket. As the probe is removed, the shaped edge of the groove pushes the balls up into their channels. Once the satellites have separated, the locking collar is returned pushing the balls back down and locking them in place preventing them from moving around during operations.

This mechanism was pursued up until a concept design phase. Unfortunately, time constraints prevented this mechanism from progressing into the prototyping phase. A few conceivable manufacturing challenges that could present themselves during this phase would be that the detent mechanism requires a very thin rim in the socket interior to allow the balls to protrude far enough but not come out the channel. This may be very difficult to achieve using Fused Deposition Modelling (FDM) 3D printing, the method used for the prototype docking adapter. A possible better solution for prototyping

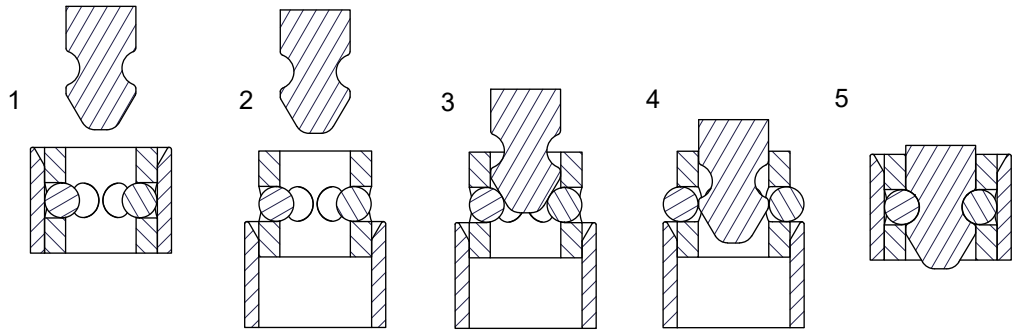

Figure 5.4: Detent Lock Mechanism operation.

would be to machine the parts however this is substantially more expensive than 3D printing. Other challenges include finding the correct size balls for the mechanism or possibly having metal parts cold welding to each other during spaceflight. The friction of the balls within their channels is also of concern as this may be large enough that it would prevent the satellites from separating using their fairly weak propulsion.

The implementation of this mechanism could also prove challenging as some form of sensor would be needed to sense when the probe is fully inserted ensuring that the locking collar does not move prematurely preventing successful docking.

5.3 Androgynous Docking Adapter

5.3.1 Design

The final mechanism that was investigated was a mechanism based off the APAS-89, APAS-95, and IDSS mechanisms. The intention of the design described here was to create a miniaturised version of these docking mechanisms. The initial design of the mechanism includes 3 inward facing guide petals that would guide the two mechanisms together accounting for the specified amount of misalignment. On these 3 guide petals is a latch that would be depressed by a latching petal on the interior of the mating adapter. Once the two adapters were fully inserted into one another the latches would spring back past the latching petal locking the two mechanisms together. The idea for these latches was to be completely passive for the docking manoeuvre thus the satellites could dock with one another even in the event of a servo failure. The unlatching portion would make use of a servo to retract the latches into the guide petals freeing the latching petals and allowing the mechanisms to separate. Finally, the latches would be locked in place once the satellites

had successfully docked, preventing them from being accidentally depressed allowing the satellites to separate. An actuator was thus needed to retract the latches and preferably to also lock the latches in place.

The prototyping phase of this mechanism started with the design of the body including the guide and latching petals. The petals on the docking mechanism were designed with an angle of 40°. This angle was chosen to be slightly steeper than the angle set out in the IDSS. This is to improve the chances of the two mechanism sliding into each other without bouncing off. To ensure that the mechanism would meet the design specifications, the petals had to protrude into the mechanism centre by more than 10 mm. This was so that the petal would still contact the body even with a misalignment of 10 mm. A height of the petals was thus chosen as 15 mm. This produces a protrusion of ≈12.6 mm. A diameter of 100 mm was chosen for the mechanism. This was so that the mechanism would fit exactly onto one face of a 1U cubesat. Finally, the height of the body was chosen to be 20 mm. This ensured enough space for the petals as well as any mechanisms that would operate the latches. The full mechanism would, thus, have a height of 35 mm. This allows 15 mm for the image processing computer, servo and mounting hardware. Thus the entire docking module should fit within a 0.5U volume.

The next prototyping phase of this mechanism was the design of the latches. The latches were designed to have three states: A docking state, a locking state, and a retracted state. To allow all 3 states in one mechanism, a spring was used that would allow some movement in the latch. The latch would also have a sliding mechanism that a push-rod would slide in allowing latch movement. In the docking state, the push-rod would be in a middle position that would allow the latch to be depressed when the two mechanisms mated. A spring would be used to keep the latch extended and would re-extend the latch after the latching petal had moved passed it. Retracting the push-rod would retract the latch into the guide petal and extending the push-rod would lock the latch in position preventing it from being depressed.

The initial latch design included an L-shaped groove in the latch. A push-rod with a bent section would slide within the latch groove. A CAD model of this latch design is presented in Figure 5.5 To achieve the three different working positions, the push-rod would move to three positions in the groove. When the push-rod was pushed fully into the groove, it prevents the latch from moving thus locking the latch in position. The push-rod can then be pulled to the other end of the groove. In this position, the latch can move as far as the groove allows. This allows the latch to be fully extended but can also be depressed thus this is the position used for docking. The push-rod can then be pulled further. At this point the push-rod has moved the full extent of the groove and thus will be pulled down by the push-rod with further retraction

of the push-rod. A small plate over the groove prevents the push-rod from being pulled out the latch completely. This facilitates the unlatching/undocking position.

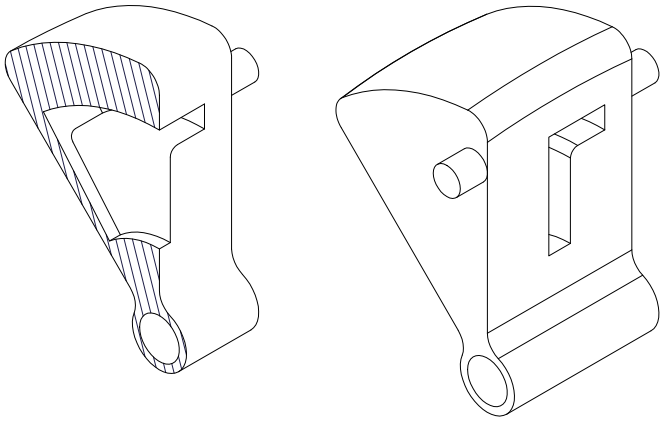

Figure 5.5: Initial latch design with L-shaped groove.

It was found during prototyping that this latch design presented multiple issues when 3D printed. Initially, an FDM printer was used but this printer could not achieve the resolution required for the latch. The latch was thus printed on a Stereolithographic (SLA) printer. This yielded great improvements to the mechanism however the print left residue in the groove that caused the push-rod to bind in the groove. The groove was also warped somewhat which caused further binding. This lead to a redesign of the latch.

The new latch would include a solid latch with a lever arm that the push-rod would engage with, operating the latch. This new design was significantly easier to print on the SLA printer as it did not include the undercuts of the grooved latch. This new latch design can be seen in Figure 5.6. To operate the latch, an EZ-connector, a connector used for servos on RC aircraft, was used. This connector can rotate accounting for the change in angle of the push-rod during operation. With the push-rod in its resting position, the EZ connector can slide on the push-rod. This allows the latch to be depressed. A spring is used to keep the latch extended. To lock the latch, the push-rod is pushed into the EZ connector. The push-rod then engages with the latch preventing it from being depressed locking it in position. Finally, to retract the latch, the push-rod is pulled until the stop at the end of the rod engages with the EZ connector. Further pulling on the rod will thus retract the latch.

The approximate strength of the spring can be calculated by analysing the forces on the latch during docking. The force diagram for this problem can be

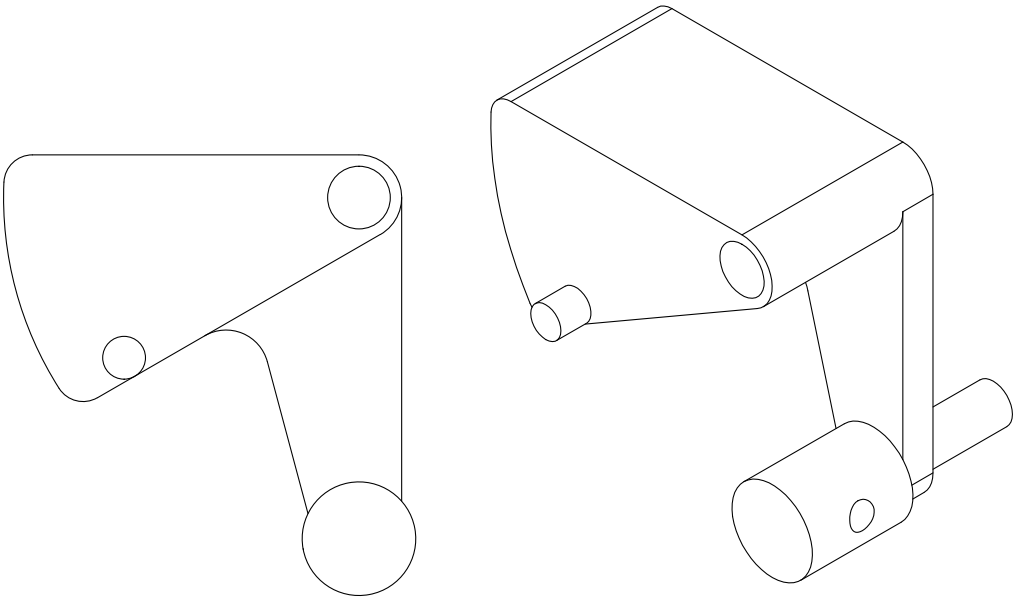

Figure 5.6: New latch design with EZ connector.

seen in Figure 5.7.

The first equation that can be derived is that of the moments on the latch. The static moment equation for the latch is as follows:

$$F_d \cos(40^\circ) \cdot L \cos(10^\circ + \theta) + F_d \sin(40^\circ) \cdot L \sin(10^\circ + \theta) - (d) \cdot F_s \cos(30^\circ + \theta) = 0 \tag{5.1}$$

where F_d is the normal contact force between the latch petal and the latch, F_s is the force applied by the spring on the latch, L is the distance from the pivot of the latch to the contact point, and d is the distance from the pivot of the latch to the point where the force F_s is applied.

The second equation derived is that of the vertical forces between the satellites as they dock. For simplicity, one of the satellites is assumed to be fixed i.e. it will not accelerate or decelerate when the two spacecraft dock. It is also assumed that all 3 latches on both spacecraft are involved in the docking. The force equation for the satellites is as follows:

$$F = ma \tag{5.2}$$

$$6F_d \cos(40^\circ) = 3a$$

$$F_d = \frac{a}{2\cos(40^\circ)} \tag{5.3}$$

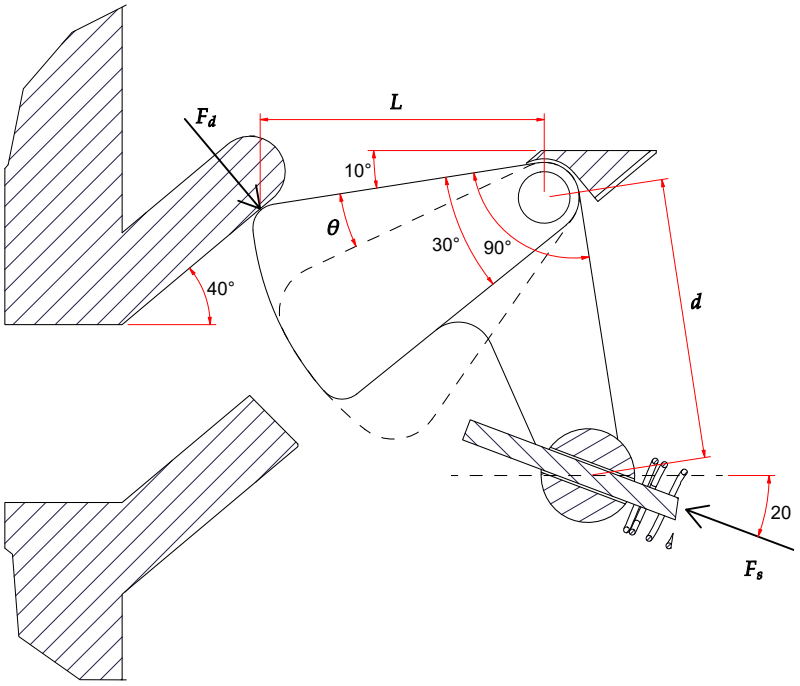

Figure 5.7: Force diagram of the latch during contact when docking.

where a is the acceleration of the spacecraft upon contact. An approximate mass of 3 kg was used to approximate a 3U cubesat. This is the smallest likely cubesat size that would fly a docking module.

Equations 5.1 and 5.3 have 3 unknowns for the two equations thus another equation is needed. An approximation of the acceleration can be calculated using the linear motion equations and some assumptions. To begin this process, an approximate distance travelled by the spacecraft from first contact to latching is needed. This is calculated as follows:

$$\frac{L\sin(\theta)}{\cos(40°)} = s \tag{5.4}$$

The size of the latch, and thus the size of L and d are known as 12.5 mm and 12 mm respectively. The travel of the latch, θ, is also know as 30°. The distance travelled, s, is thus calculated as 8 mm.

Assuming the spring force increases linearly, the acceleration on the satellite from first contact to latching will increase linearly. The acceleration of the satellite can thus be approximated using the median acceleration over the full distance which would have the equivalent effect as a constant acceleration over the distance. An initial contact velocity of 0.05 m/s was assumed for this

equation. This velocity was considered achievable by a cubesat within a 1 m distance. Using the equations of linear acceleration, the acceleration can thus be approximated as:

$$\begin{aligned} v^2 &= u^2 + 2as \\ 0 &= 0.05^2 + 2a(0.008) \\ a &= -0.156\,25\,\mathrm{m/s^2} \end{aligned} \tag{5.5}$$

From equation 5.3, an approximate, minimum docking force can be calculated as:

$$\begin{aligned} F_d &= \frac{0.15625}{2\cos(40^\circ)} \\ &= 0.101\,985\,\mathrm{N} \end{aligned}$$

Substituting this result into equation 4.1, the spring for can be calculated as:

$$F_s = 0.310\,609\,\mathrm{N}$$

The standard spring equation for a linear spring can be used to calculate an approximate maximum spring constant for this docking velocity. The spring equation is:

$$F_s = kx \tag{5.6}$$

where k is the spring constant and x is the compression of the spring. To find k, the compression of the spring must be know. This compression can be approximately calculated as:

$$\begin{aligned} x &\approx d\sin(\theta) \\ x &\approx 12\sin(30^\circ) \\ &\approx 6\,\mathrm{mm} \end{aligned} \tag{5.7}$$

Substituting the spring force calculated earlier and the compression of the spring into equation 5.6, k can be calculated as:

$$\begin{aligned} 0.310609 &= k(0.006) \\ k &\approx 51.768\,\mathrm{N/m}. \end{aligned}$$

Unfortunately, a spring with this low spring constant could not be readily found. A spring with a spring constant of 60 N/m was thus used in the prototype. This was the weakest, readily obtainable spring that was small enough

to fit within the latching mechanism. Custom springs were considered for this prototype however it was deemed too expensive and difficult to obtain. Using this spring constant, a new docking velocity of 0.065 m/s can be calculated. Though larger than the 0.05 m/s initial estimate, this docking velocity should also be achievable on the STF. An electromagnet could also be used to supplement the docking force reducing the required velocity.

Due to size constraints on the prototype piece, a 9 gram servo was used. This servo, however, took up a large amount of space within the mechanism and thus the one servo would have to retract all 3 latches. Initially, a rotation plate with 3 fixed push-rods was part of the design. The issue with this is that the mechanism would then have to allow for the transverse motion of the rods when the plate was rotated. A ball joint within the latch would allow for this however this would prevent the same push rods from performing the locking action. Another alternative was to split the push-rod into two pieces. This would allow the push-rod to be used for both locking and retracting the latches. The problem with this is that a spilt rod would need a complicated joint in the middle, which, at these scales, was difficult to achieve. Further, guides would have to be used to prevent the rods from collapsing when trying to lock the latches.

Two mechanisms were designed to linearise the servo motion allowing the latches to be retracted and locked without needing to consider the transverse motion induced by the rotation. The main downside of this is that it introduces more complexity into the mechanism which inherently makes the mechanism less reliable. The first of these linearisation mechanisms placed the servo perpendicular to the base plate of the docking mechanism. The servo would have a servo arm with a push-rod that pushed a sliding plunger vertically. This plunger was connected to 3 levers that each had push-rods connecting to the latches. Thus, to retract the latches, the servo would be rotated pushing the plunger upwards. This would cause the levers to pull the latching push-rod downwards retracting the latches. To lock the latches, the servo would be rotated to pull the plunger downwards. This would push the levers upwards, pushing the push-rods into the latches, preventing them from retracting. A CAD diagram of this mechanism can be seen in Figure 5.8. This mechanism introduces many extra moving parts into the docking adapter, greatly increasing the complexity.

The second linearisation mechanism had the servo operating a rotating plate in the same plane as the docking mechanism base. Within this plate are a series of spiral grooves starting near the centre of the plate and moving outwards towards the edge. A set of sliders would then run in these grooves. Attached to the sliders would be a push-rod that operated the latches. To ensure that the sliders motion was linear, a set of 3 channels would be placed

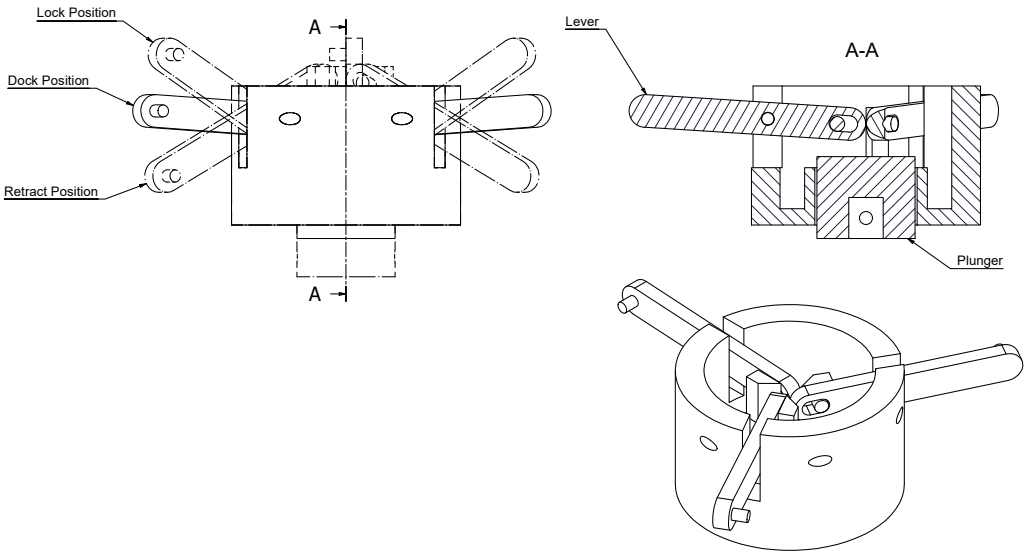

Figure 5.8: Lever arm linearisation mechanism.

into the base of the docking mechanism that the sliders would run in. Thus, when the plate was rotated, the slider would move outwards from the centre of the mechanism in a linear fashion. During the docking operation, the sliders would be moved to the centre of the channel. This ensures that the push-rods are not pulling on the latches retracting them, nor are they pushed into the latches locking them in place. This mehcanism can be seen in Figure 5.9. This mechanism has the advantage over the previous in that there are less moving parts and thus less complexity. The downside, however, is that this mechanism makes use of sliding parts. This type of part add extra complex as they can easily bind, specially in a mechanism such as the spiral grooves. Should these parts be made of some metal, cold welding of the parts would also need to be considered.

In both cases, a set of 3 small servos would be preferable to the single larger servo. These 3 servos would actuate the 3 push-rods directly forgoing the need to have a complicated linearisation mechanism. This would not only make the mechanism less complicated but is also likely to make the mechanism more reliable as there would be less chance of parts binding. These small servos are very hard to obtain however and thus a standard 9g servo was used.

The spindle based mechanism was chosen due to the space constraints in the centre of the module. The spindle mechanism also worked better with the latch redesign. Once the lever arms had been added to the latches, the lever based mechanism would need to have very short push-rods and thus a very short spring. This made it less feasible than the spindle mechanism.

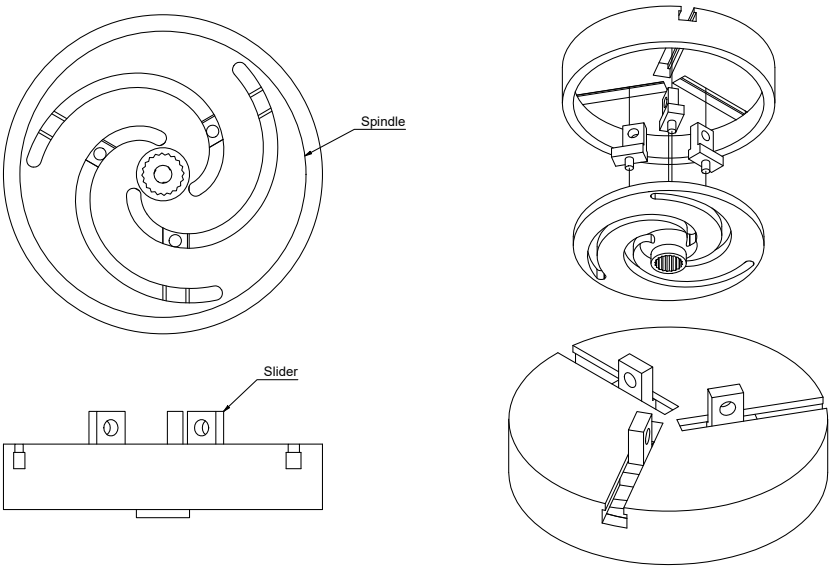

Figure 5.9: Spindle linearisation mechanism.

In summary, the prototype docking mechanism was made up from 3D printed and bought out parts. The main body of the mechanism as well as the swivel plate on the servo were 3D printed using an FDM printer. The latches, slider, and push-rod ends were printed on an SLA printer. The spring was an easily obtainable, bought-out part and the servo was a 9 gram hobby aircraft servo which was also readily obtainable. An EZ connector was used to connect the latch to the push-rod. This connector is commonly used on hobby aircraft. Finally, 2mm brass rod was used for the axles for the latches and push-rods and a 1mm brass rod was used for the push rods. A 90° bend was placed in the end of the push-rod to catch on the EZ connector to pull the latch back. The complete CAD model of the prototype can be seen in Figure 5.10 and an image of the physical prototype can be seen in Figure 5.11.

5.3.2 Results

5.3.2.1 Basic Testing

From basic fit checks, the latch mechanism is able to successfully hold the two docking adapters together. This basic check consisted of mating two prototype mechanisms together. One of the mechanism had a 1 kg mass suspended from it. A image taken from the test is seen in Figure 5.12. The mechanism successfully supported the weight suggesting it would perform satisfactorily as a docking adapter. Further testing would be needed to confirm this.

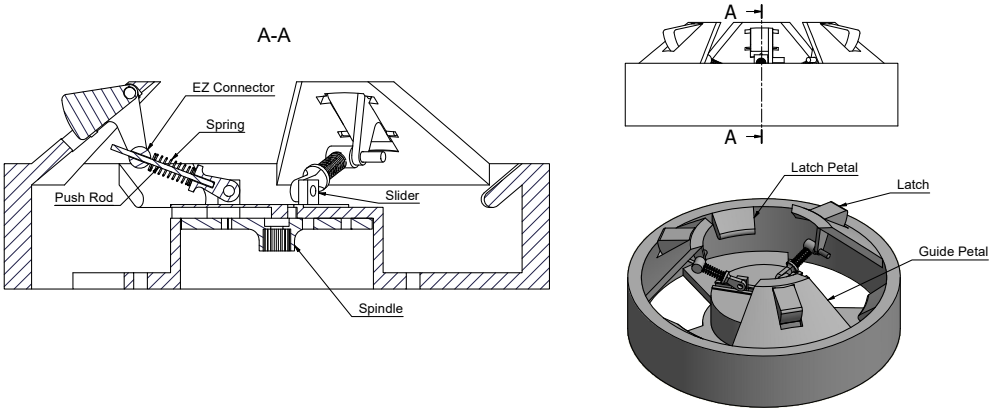

Figure 5.10: Androgynous Docking Adapter Mechanism.

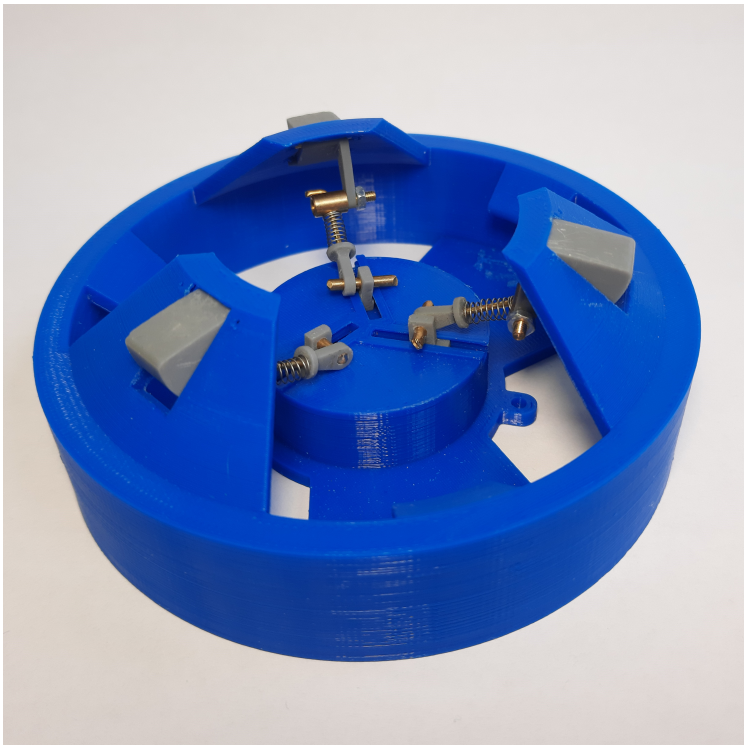

Figure 5.11: Prototype docking module.

5.3.2.2 Manufacturability

As mentioned in the previous section, the prototype docking mechanism was 3D printed on a Creality CR-10S with PLA filament. Due to the overhangs of the petals, support was needed on the latch petals. The angle on the guide petals was small enough that no support was needed, however, the underside of the petals have grooves for the pivot of the latches and for the latch stops

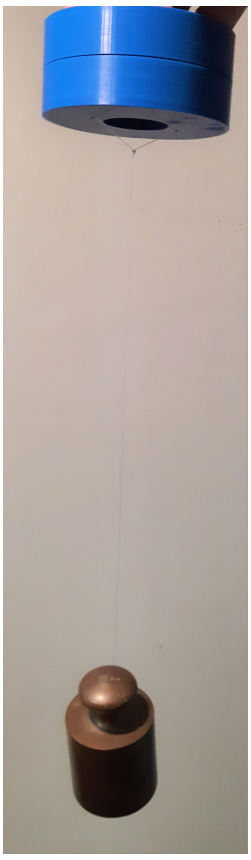

Figure 5.12: Prototype docking adapter supporting a 1kg load.

which were often not printed correctly without supports. The grooves are also fairly small which meant that adding supports didn't improve the print quality significantly. Using SLA printing may yield improved printed results due to the finer print resolution.

The prototype also yields some insight into the manufacturability of the mechanism. For a space application, only certain plastics can be used such as delrin. Some of these plastics can be used for 3D printing however they bring a lot of challenges that may render 3D printing a space-ready mechanism impractical. The use of Selective Laser Sintering (SLS) printing allows the mechanism to be printed out of metals. Metals are a good material for space applications and this specific printing process may yield great results.

Should 3D printing not be viable for the space-ready mechanism, this mechanism could easily be converted to a machinable part. A 6-axis CNC may be able to machine the part as is however this process is generally very expensive. Potentially converting the circular body from circular to hexagonal would mean that the petals would end up as flat planes rather than curved. This

means that the petals could be easily manufactured from flat metal stock and attached to the main body reducing the need for complicated machining processes greatly improving manufacturability.

5.3.2.3 Suggested Testing

The following tests are proposed to test the effectiveness of the docking mechanism. Due to time constraints, these test were not able to be completed.

The first proposed test involves placing one of the mechanism on a fixed mount. The mating mechanism will be placed on a linear rail such that the mechanisms can be docked, separated and then redocked. The idea of this test is to test the repeatability of the docking mechanism to determine its reliability. This test could also be extended to include a test of the docking velocity by using some form of motor to move the docking mechanism at a fixed velocity.

The second proposed test involves having one of the mechanisms on a fixed mount once again. The other mechanism is then placed on a rotating mount that causes the mechanism to rotate about the yaw axis. This rotating mount is then placed on a linear rail. This test is intended to determine whether the mechanism can successfully dock with the specified angular misalignment. A similar test can also be set up for the other rotational axis however the docking mechanism would likely have similar capabilities in the other axis due to its symmetry. This is similar to the test performed by Boesso and Francesconi, and Barbetta et al.[23, 24]. This test could be extended further to include placing the moving mechanism on some form of ball joint. This would allow a compound angular misalignment to be tested.

The third proposed test involves placing the linear rail at some perpendicular offset from the centre of the fixed docking mechanisms. The moving docking mechanism would be mounted to another linear rail that allows motion perpendicular to the first rail. Thus, when the mechanisms meet, the rail will allow the mechanism to move into the centre of the other mechanism and allow the two mechanisms to mate. This test would then be used to determine whether the mechanism meets the requirement for lateral misalignment.

The final proposed test involves the use of the satellite test facility. In this test, the two docking mechanisms would be placed on two test carts. The tests carts would then use the pose estimator and closed-loop control to perform the necessary docking manoeuvres to dock the two test carts. This test would obviously require the development of a control system for this purpose and thus is closer to a final implementation test. This test would thus prove the viability of this mechanism for a cubesat docking mission.

Chapter 6

Flight Solution Adaptations

The docking system that was presented and analysed so far in this thesis is intended for testing in a laboratory environment, and certain assumptions and simplifications have been made to allow for the concept to be proven, without necessarily designing the system for a full flight mission. This chapter discusses the increments and design adaptations that are still necessary to move from the concept design to a flight-ready implementation.

6.1 Processing

The use of a computing unit such as the Nvidia Jetson Nano is not completely unreasonable on board a cubesat. A few considerations need to be made such as power consumption, spatial constraints and radiation tolerance.

The biggest issue with using the Jetson Nano onboard a cubesat is the power consumption, at least at full power. As stated in Section 4.1.1, the Jeston Nano can consume up to 10 W of power. A cubesat generally is able to produce between 3 and 20 W of power from solar panels. This does not bode well for the use of the Jeston onboard a cubesat, however, it is important to remember that the docking operation, and thus the use of the Jetson, is not a constant operation during a mission. Thus, a cubesat with a sufficiently large battery to store sufficient amounts of power for the portions of the mission in which the Jetson is used, would feasibly be able to fly a Jetson.

Cubesats have very restrictive spatial constraints. The Jetson, however, is well suited for small spaces. The Jetson Nano module, without the carrier board, measures only 70 mm x 45 mm. This is well within the 100 mm x 100 mm form factor of a cubesat. Thus, spatial constraints are not likely to prevent a cubesat flying a Jetson Nano.

The radiation tolerance of cubesat components also plays a major role in parts selection. A cubesat is typically launched into low-earth orbit (LEO) (<1000km altitude). The typical lifespan of a cubesat mission also tends to be less than 2 years. A demonstration mission, such as Docksat, would likely easily complete all mission goals comfortably within one year. Slater et al. [43] tested the total ionizing dose (TID) that the Nvidia Jetson Nano could withstand. From this testing, it was found that the Jetson could likely operate with a TID of beyond 20 krad(Si) with 100 mils (2.54 mm) of aluminium shielding. This equates to an approximate lifespan of 1.5 to 2 years. This is much longer than the expected duration of the Docksat demonstration mission. Thus it is not unreasonable to assume that a Jetson Nano could possibly be flown on a cubesat mission.

There also exists a few off the shelf on-board computers (OBC) units for cubesats that could be used for the imaging system such as the Telos-10, Telos-40 and Telos-60 series OBC's from Orb Astro [44]. These units possess relatively fast processing units design for advanced compute applications such as image processing.

A final consideration for processing is the use of a slower processor used for the calculation steps with a field-programmable gate array (FPGA) that handles the image capture and basic processing. The combination of FPGA and micro-processors could allow similar frame rates as a pure processor solution while using a much cheaper and more radiation hardened processor. A slower, conventional processor, such as an STM microcontroller, could be used in isolation if the pose estimator sample rate needed is much lower than the 100 Hz used for design in this project.

6.2 Camera

Cameras are not a new payload for cubesats and thus finding a suitable camera should not prove too difficult a task. The biggest issues will be finding a camera that can operate at the desired frame rates and that is sufficiently radiation and temperature resistant. The resolution of the camera is also a consideration however, similar resolution as that used in the pose estimation testing is not uncommon among space rated cameras.

6.3 Docking Mechanism Materials

Two main materials exists that could potentially be used to manufacture the docking mechanism: space-grade plastics and metals.

Plastics seem like a viable solution due to their low mass and ease of manufacturing. A few considerations need to be taken into account when selecting a plastic for use with the docking mechanism. The first is the friction when the two docking mechanisms meet. Should this friction be too high, the cubesat may loose to much speed and thus not be able to compress the latches and thus would not be able to dock. Another consideration is that of outgassing. Outgassing has the potential to damage electronic systems and degrade the performance of optical payloads. Both of which could endanger the cubesat mission. The structural integrity of parts may also become an issue as outgassing slowly degrades their structure. Impact resistance could also prove to be a factor and multiple docking procedures could damage the mechanism and prevent further docking. Also, micrometeorites could also damage the mechanism. Finally, the thermal expansion of the plastic becomes very important for the docking module. A large expansion or shrinkage of the plastic could prevent the mechanism from mating correctly thus preventing the docking procedure.

Metals could also prove a viable solution and are generally the material of choice for larger docking modules. Metals such as aluminium and titanium could be good choices due to their low density leading to lighter docking modules. This could affect launch costs. These metals also tend to be much stronger than plastics and so damage of the docking module could be less of an issue. Metals, however, pose the added problem of potential cold welding, a phenomenon whereby metals fuse without heat due to the lack of a protective oxide layer on the metal surface [45].

Chapter 7

Conclusions

This thesis set out to develop components of a cubesat docking module for demonstration on the ESL's air bearing satellite test facility. Two major components were investigated: a pose estimation system was designed and tested and a mechanical docking mechanism was investigated and a prototype was constructed. The ability to create a space-ready solution from the work of this thesis was also discussed.

The design and testing of the pose estimator included combining a simple 6 DOF pose estimation system with distortion correction of a 200° FOV lens. A number of tests were set up to determine the systems accuracy. These yielded very good results when the LED target was in the centre of the camera image however, movement away from the centre yielded very large losses in accuracy. This was believed to be due to limitations in the specific pose calculations combined with the large distortions added by the lens that the correction algorithm may have failed to fully correct.

The main issues with the system are the loss of accuracy of the pose estimator when the target is not in the image centre. This could potentially be mitigated or at least lessened by using a smaller FOV lens with the downside of require more manoeuvres to find the targets on orbit. Further, great accuracy of the azimuth measurement was achieved with the use of the distortion corrected vectors. Moving the entire pose estimator over to using these vectors could potentially improve the accuracy of the system as a whole even when away from the image centre.

Three different docking mechanism concepts were investigated for this thesis. Of the three mechanisms, two were pursued into a module concept development phase. Finally, one module concept was prototyped. This module was 3D printed and the mechanism basic functionality was tested. The mechanism worked well however some issues were found: the positioning of the push-rod made the latches bind open on occasion and the length of the push-rods needed

to be very accurate to ensure proper locking. With further testing, the module could be improved to a working, space-ready solution.

The discussion of the ability to turn this project into a space-ready solution found that the processor used could easily be implemented on a cubesat as well with sufficiently large solar panels and battery storage. Sufficiently powerful, space-ready processors also exist that could replicate this system on a cubesat platform. The docking mechanism was also small enough to fit on a cubesat and with some consideration to material and actuator selection, the module could be used directly as a space-ready docking mechanism.

To implement a full demonstration, a control system would need to be developed for the test facility that would handle the manoeuvres required to dock the two carts. Also, the docking adapter servos would need to interface with the main control computer so that the docking modules could be controlled by whatever system operates the control system.

7.1 Future Work

The following is recommended to develop a working prototype docking module following on from the completed work:

- Develop a control system based on the pose estimator to dock the two test carts.
- Implement the image processing and control on a platform small enough to fit within the docking module.
- Combine all segments into one docking module.
- Preform docking tests.

The following future work can be considered to improve the docking module:

- Investigate the use of the unit position vectors for pose estimation.
- Consider implementing a EKF to improve the pose estimation accuracy.
- Investigate smaller FOV camera lenses to potentially improve pose results.
- Investigate the use of multiple cameras for long and short range pose estimation. This would include handover between the two cameras.

- Machine the docking mechanism from space ready materials and investigate their effectiveness.
- Investigate the use of electromagnets to aid in the docking procedure.
- Investigate the other docking mechanisms. A comparison would allow the best mechanism to be selected.
- Investigate the addition of an inter-satellite link for effective communications between the satellites.
- Investigate adding data and/or power transfer between test carts once they have docked.
- Look into novel control methods for test carts with limited translational capabilities. This could include having both carts actively engage in the docking manoeuvre rather than the typical active chaser/passive target case.

Appendices

Appendix A

Docking Interface Drawings

This appendix includes the drawings of the concept Detent Mechanism and of the prototype Androgynous docking adapter.

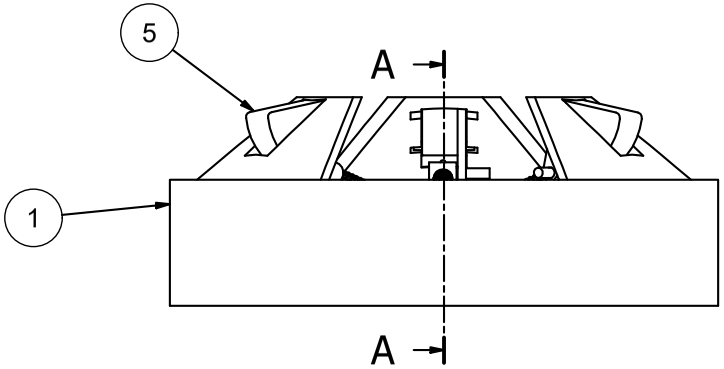

A-A (1 : 1)

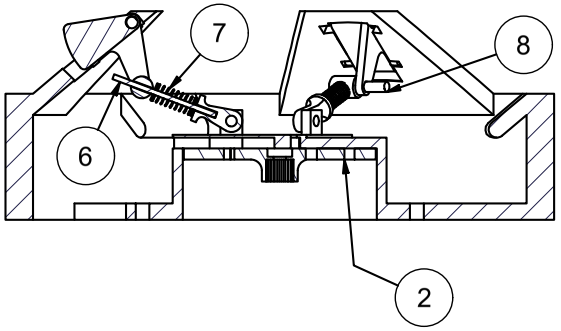

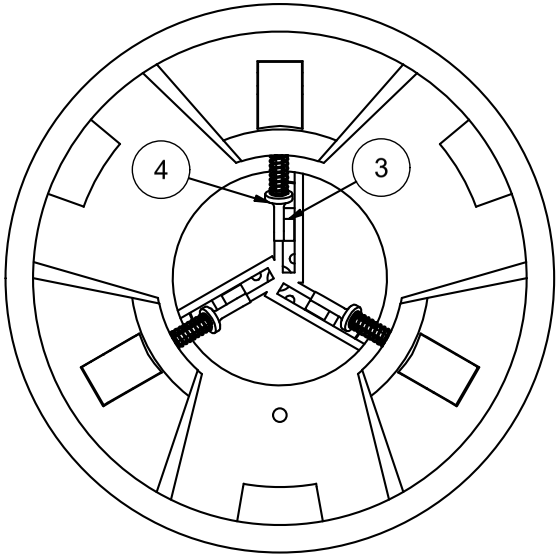

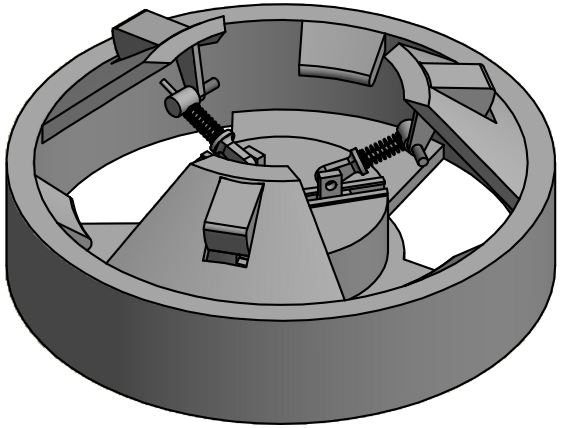

Parts List			
8	EZ Connector	3	
7	Spring	3	0.6N/m
6	Push-rod	3	1mm x 13
5	Catch	3	2-2
4	Push-rod Eye	3	2-5
3	Shifter	3	2-3
2	Spindle	1	2-4
1	ADA Base	1	2-1
ITEM	**DESCRIPTION**	**Qty.**	**MATERIAL / SPECIFICATIONS**

STELLENBOSCH UNIVERSITY

STUDENT Nr. 20159293	**DRAWN BY** RJ WALLER	**CHECKED**	**SCALE ON A**3=1:1 **UNITS IN** mm	**TITLE:** Androgynous Docking Adapter	
			DATE 16-11-21	**SHEET Nr.** **OF** **SHEETS**	**Nr.** 2

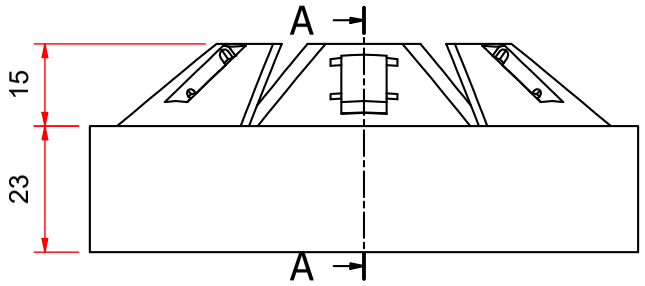

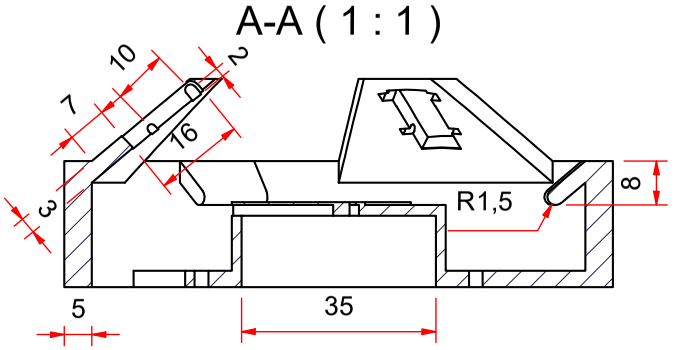

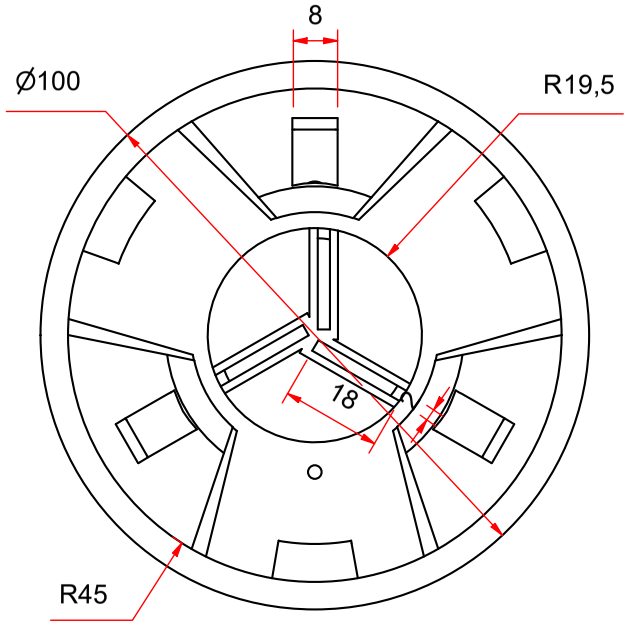

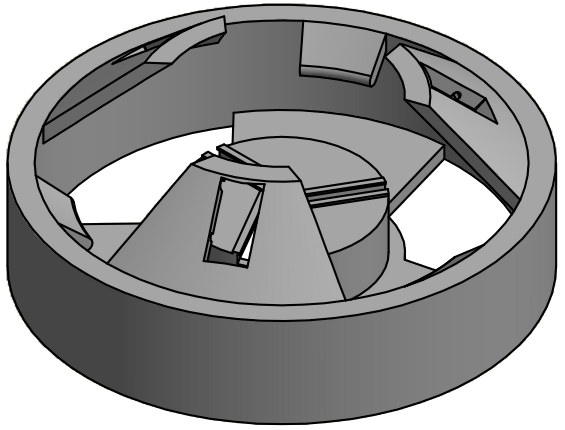

ITEM	DESCRIPTION	Qty.	MATERIAL / SPECIFICATIONS

STELLENBOSCH UNIVERSITY	SCALE ON A3=1:1	TITLE: ADA Base	
	UNITS IN mm		
STUDENT Nr. 20159293	DRAWN BY RJ WALLER	CHECKED	DATE 16-11-21
SHEET Nr. OF SHEETS	Nr. 2-1		

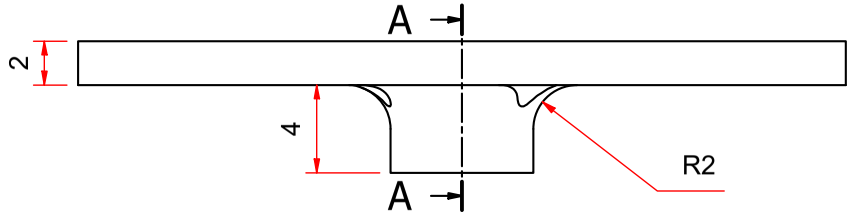

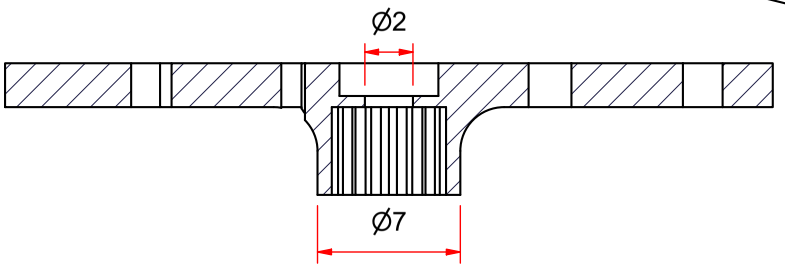

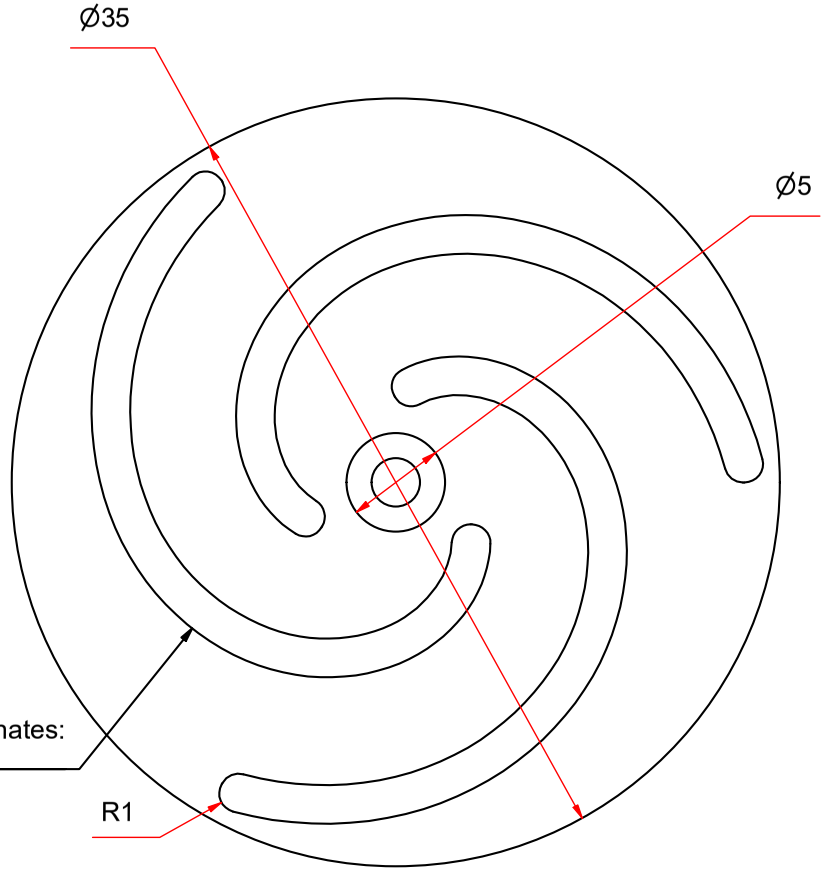

Equation in radial co-ordinates:
$r = 16 - 0.058\Theta$

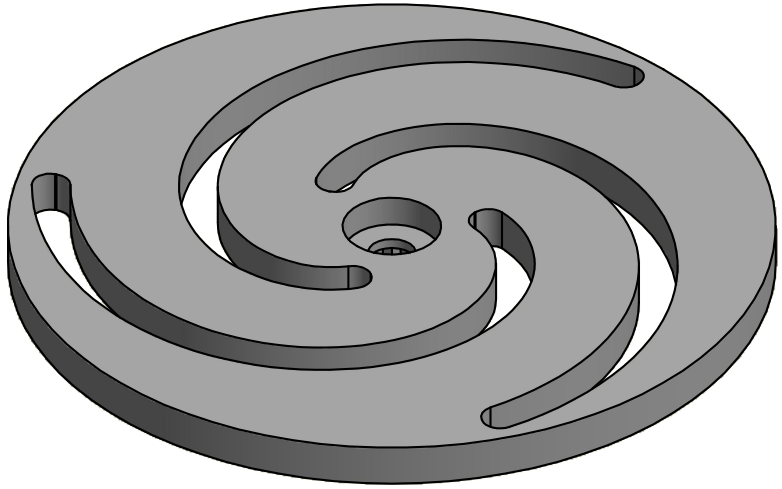

ITEM	DESCRIPTION	Qty.	MATERIAL / SPECIFICATIONS

STELLENBOSCH UNIVERSITY	SCALE ON A3=4:1 UNITS IN mm	TITLE: Spindle	
STUDENT Nr. 20159293	DRAWN BY RJ WALLER	CHECKED	DATE 16-11-21
SHEET Nr. OF SHEETS	Nr. 2-4		

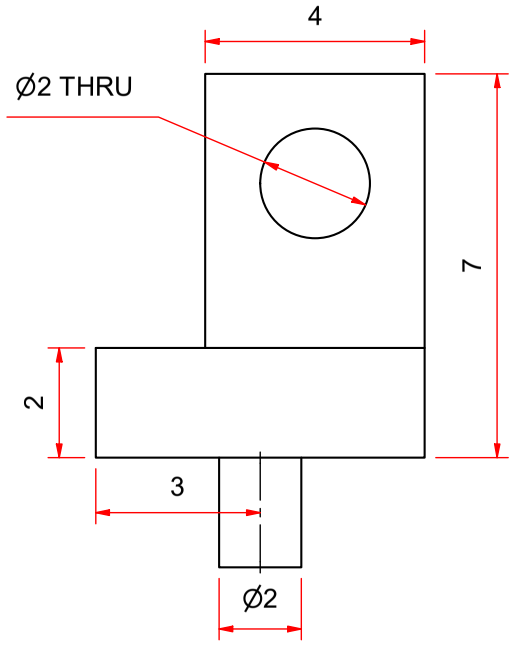

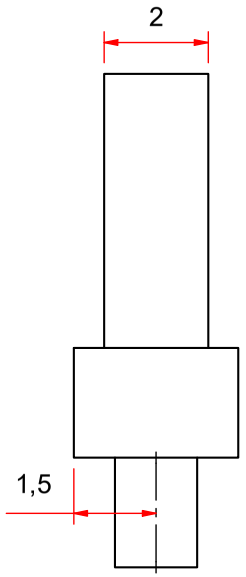

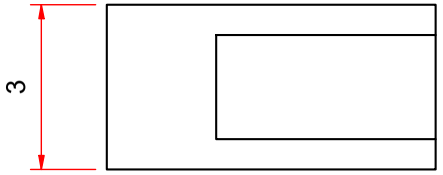

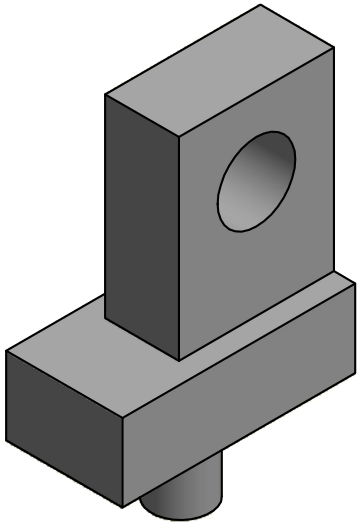

ITEM	DESCRIPTION	Qty.	MATERIAL / SPECIFICATIONS

STELLENBOSCH UNIVERSITY	SCALE ON A3=10:1 UNITS IN mm	TITLE: Shifter	
STUDENT Nr. 20159293	DRAWN BY RJ WALLER	CHECKED	DATE 16-11-21
SHEET Nr. OF SHEETS	Nr. 2-3		

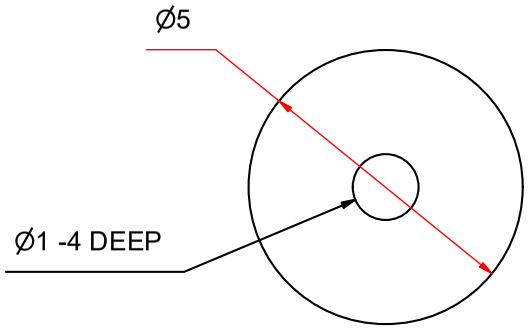

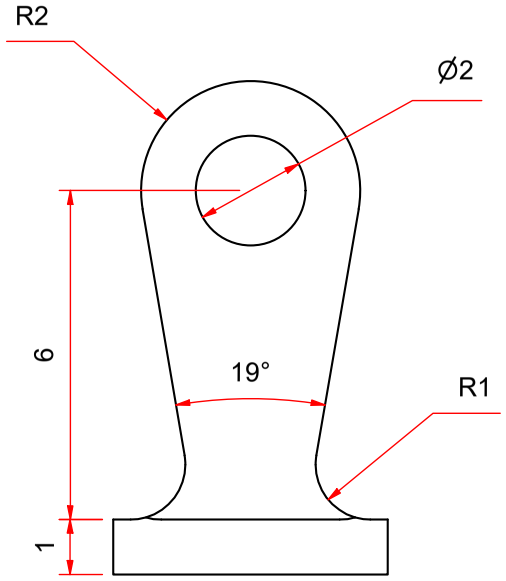

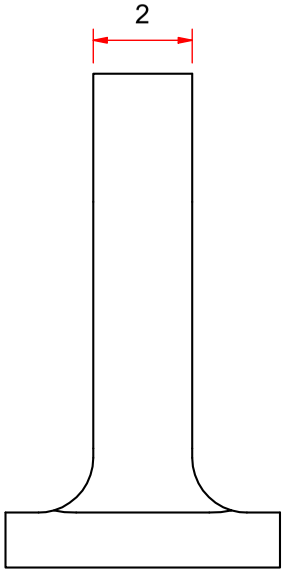

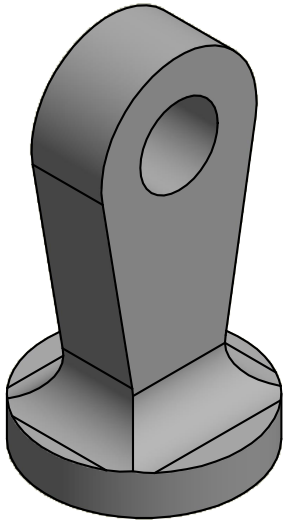

ITEM	DESCRIPTION	Qty.	MATERIAL / SPECIFICATIONS

STELLENBOSCH UNIVERSITY

SCALE ON A3=10:1		TITLE: Push-rod Eye	
UNITS IN mm			
STUDENT Nr. 20159293	DRAWN BY RJ WALLER	CHECKED	DATE 16-11-21
SHEET Nr. OF SHEETS		Nr. 2-5	

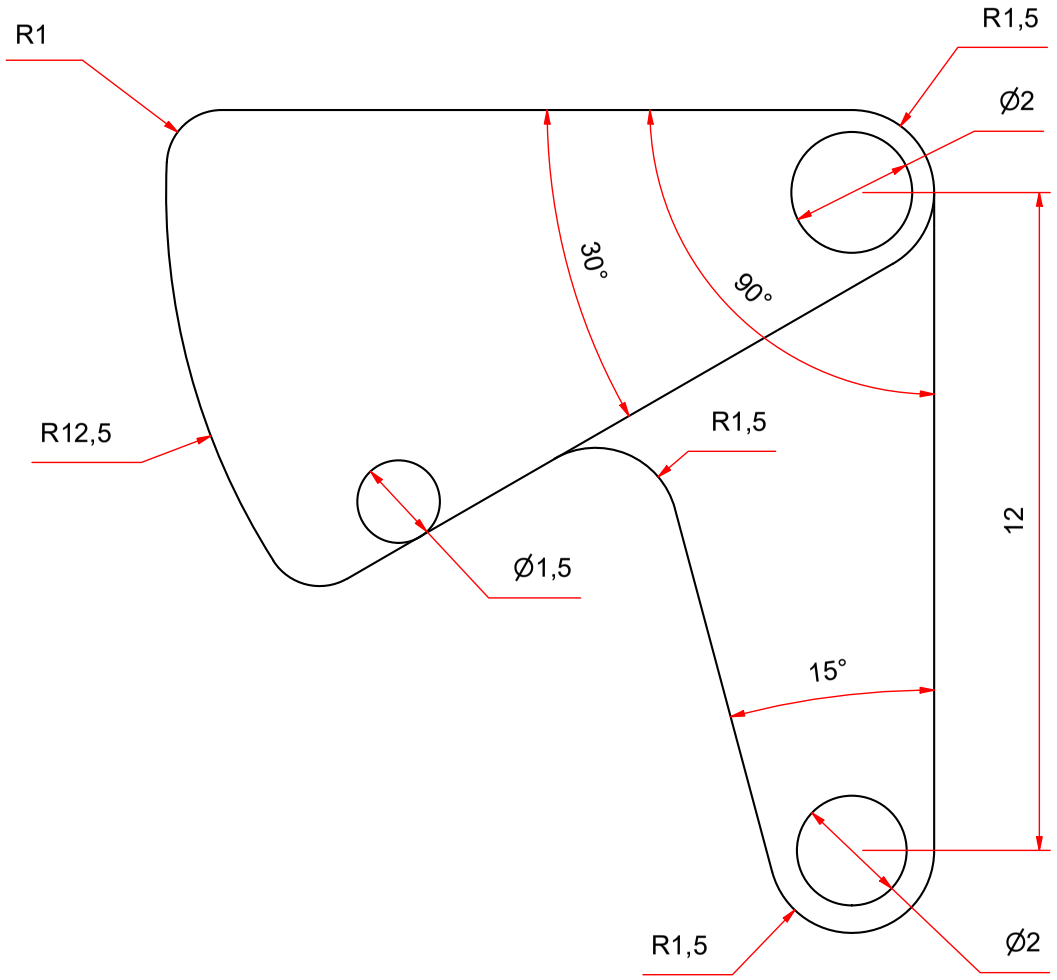

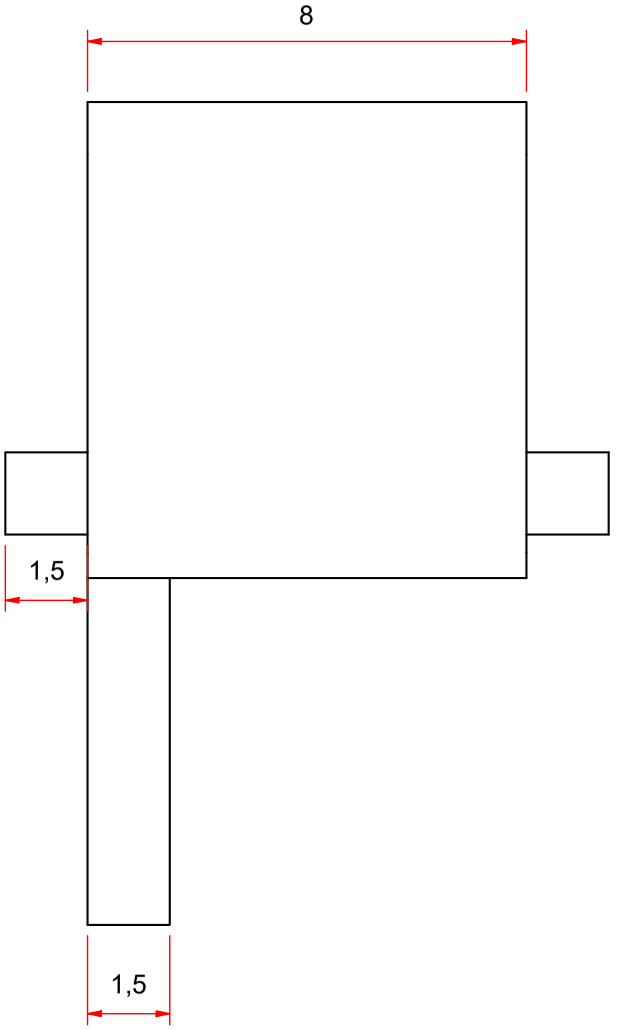

ITEM	DESCRIPTION	Qty.	MATERIAL / SPECIFICATIONS

STELLENBOSCH UNIVERSITY

SCALE ON A3=10:1
UNITS IN mm

TITLE: Catch

STUDENT Nr. 20159293	DRAWN BY RJ WALLER	CHECKED	DATE 16-11-21	SHEET Nr. OF SHEETS	Nr. 2-2

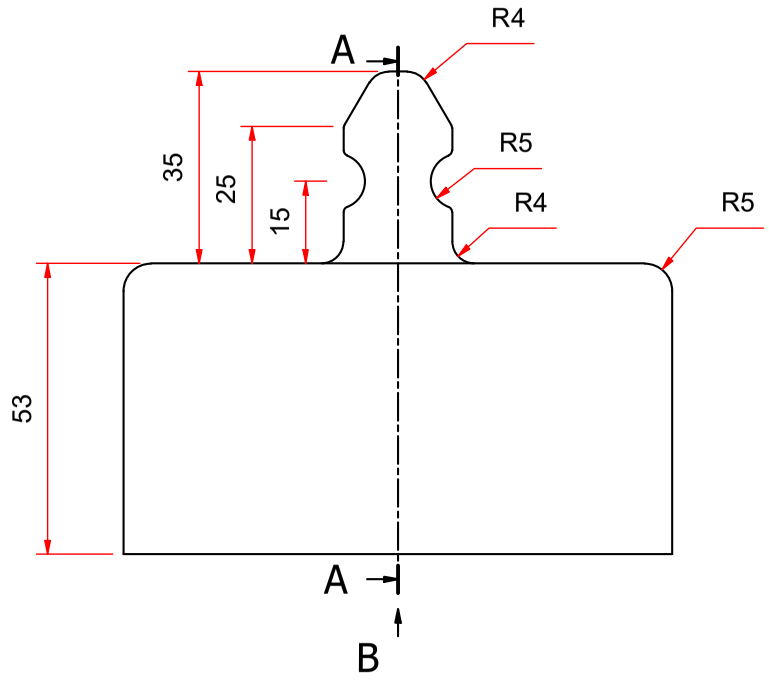

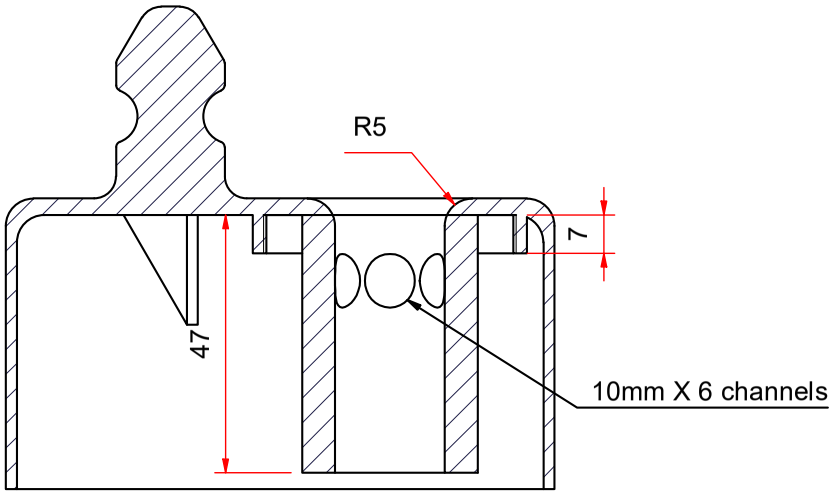

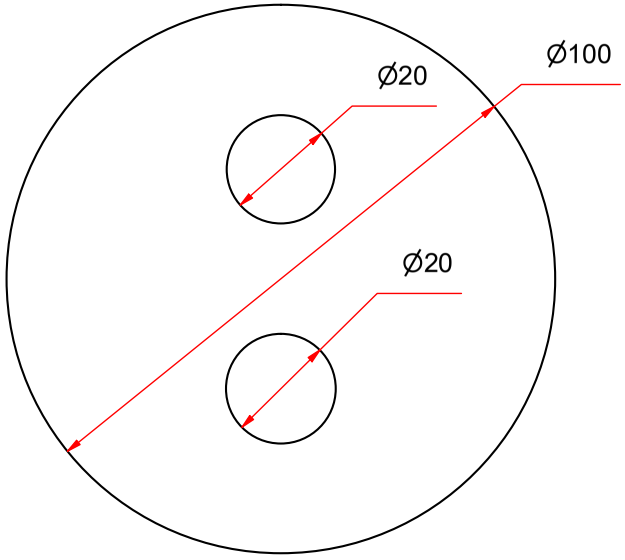

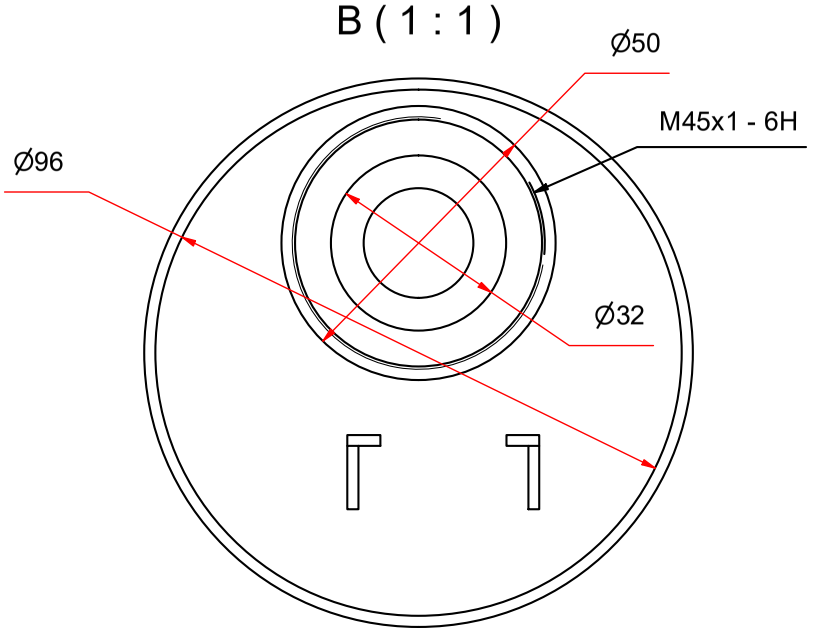

ITEM	DESCRIPTION	Qty.	MATERIAL / SPECIFICATIONS

STELLENBOSCH UNIVERSITY

SCALE ON A3=1:1		TITLE: Ball Detent Base	
UNITS IN mm			
STUDENT Nr. 20159293	DRAWN BY RJ WALLER	CHECKED	DATE 16-11-21
SHEET Nr. OF SHEETS		Nr. 1-1	

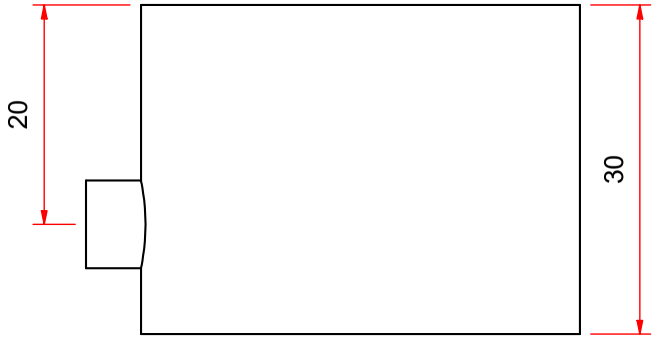

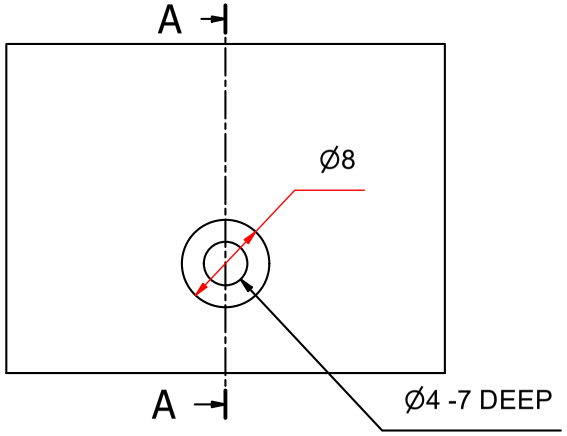

A-A (2 : 1)

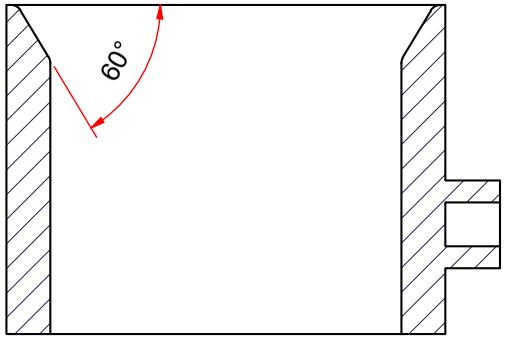

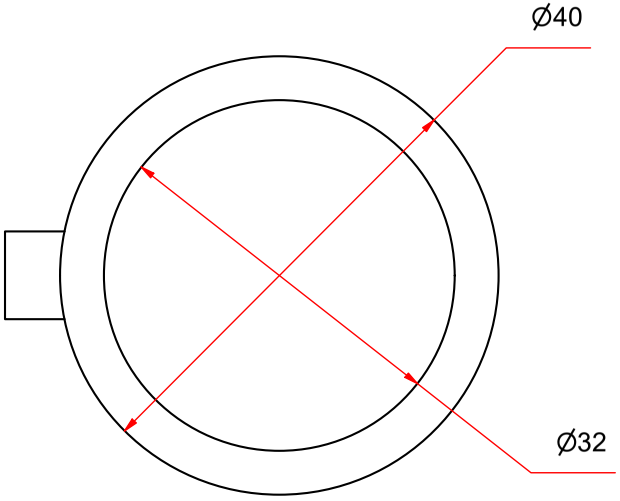

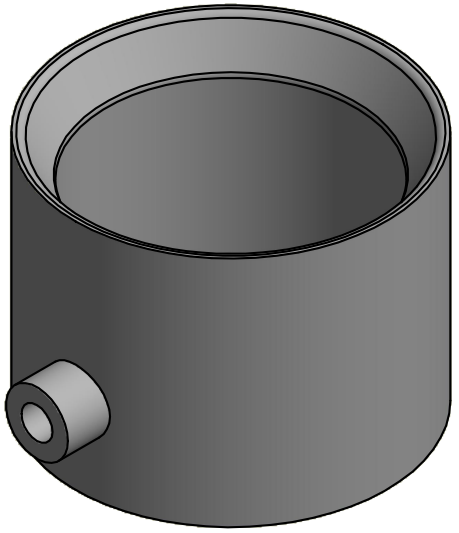

ITEM	DESCRIPTION	Qty.	MATERIAL / SPECIFICATIONS

STELLENBOSCH UNIVERSITY

SCALE ON A3=2:1		TITLE: Locking Collar	
UNITS IN mm			
STUDENT Nr. 20159293	DRAWN BY RJ WALLER	CHECKED	DATE 16-11-21
SHEET Nr. OF SHEETS		Nr. 1-3	

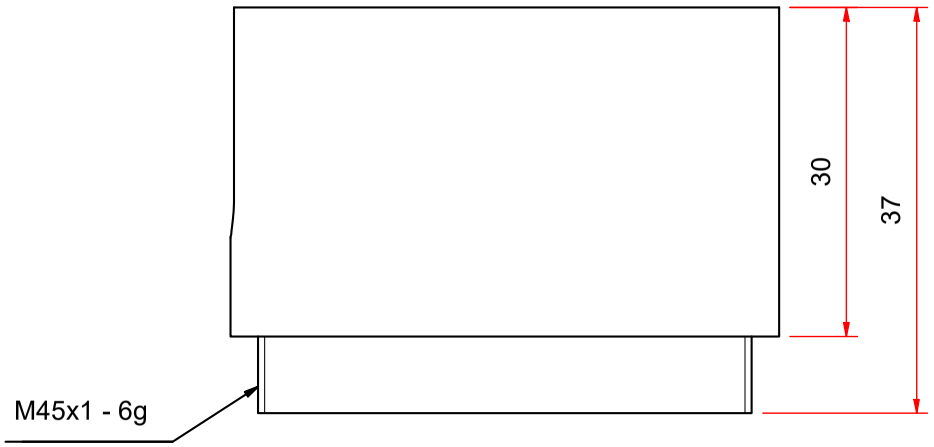

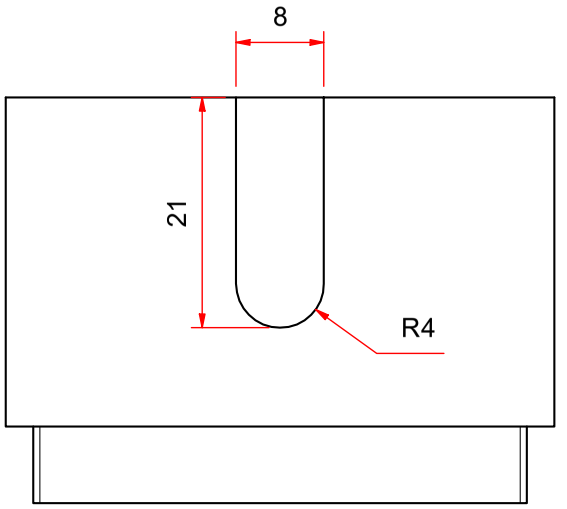

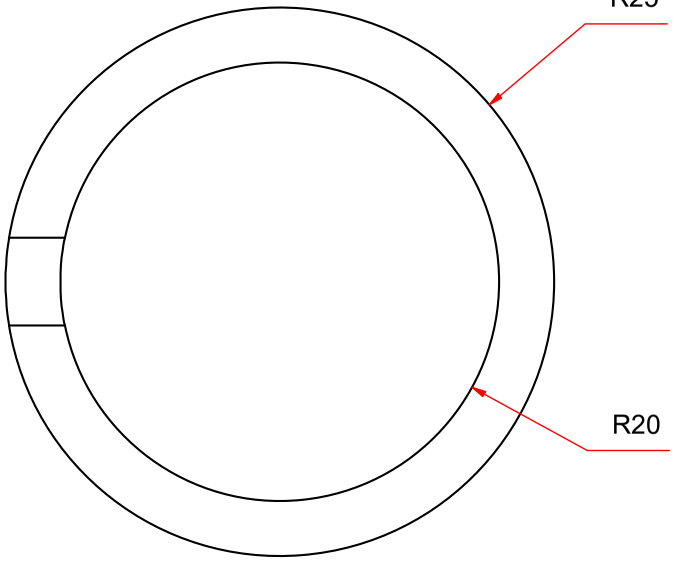

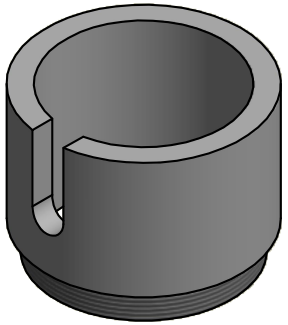

ITEM	DESCRIPTION	Qty.	MATERIAL / SPECIFICATIONS

STELLENBOSCH UNIVERSITY

SCALE ON A3=2:1		TITLE: Retaining Collar	
UNITS IN mm			
STUDENT Nr. 20159293	DRAWN BY RJ WALLER	CHECKED	DATE 16-11-21
SHEET Nr. OF SHEETS		Nr. 1-2	

List of References

[1] R. J. Waller and L. Visagie, "Pose estimation for cubesat docking," *IFAC-PapersOnLine*, vol. 54, no. 21, pp. 216–221, 2021, control Conference Africa CCA 2021. [Online]. Available: https://www.sciencedirect.com/science/article/pii/S2405896321023764

[2] J. Cook, V. Aksamentov, T. Hoffman, and W. Bruner, "ISS Interface Mechanisms and their Heritage," in *AIAA Space 2011*, 2011.

[3] D. Jansen, "Development of a Test Facility for Satellite Experiments," Master's thesis, Stellenbosch Univerisity, 2020.

[4] C. Underwood, S. Pellegrino, V. J. Lappas, C. P. Bridges, and J. Baker, "Using CubeSat/micro-satellite technology to demonstrate the Autonomous Assembly of a Reconfigurable Space Telescope (AAReST)," *Acta Astronautica*, vol. 114, pp. 112–122, 2015. [Online]. Available: https://www.sciencedirect.com/science/article/pii/S0094576515001642

[5] M. Garcia, "50 Years Ago: The First Automatic Docking in Space," 2017. [Online]. Available: https://www.nasa.gov/feature/50-years-ago-the-first-automatic-docking-in-space

[6] T. Rumford, "Demonstration of Autonomous Rendezvous Technology (DART) Project Summary," *Proceedings of SPIE - The International Society for Optical Engineering*, vol. 5088, 08 2003.

[7] "On-orbit satellite servicing study project report," Goddard Space Flight Center, Tech. Rep., October 2010.

[8] "Automated Transfer Vehicle: Europe's Space Freighter," 2014. [Online]. Available: https://esamultimedia.esa.int/multimedia/publications/ATV_brochure_EN/offline/download.pdf

[9] "SpaceX CRS-21 Mission Overview." [Online]. Available: https://www.nasa.gov/sites/default/files/atoms/files/spacex_crs-21_mision_overview_high_res_0.pdf

[10] "Cygnus Advanced Manoeuvring Spacecraft." [Online]. Available: http://wsn.spaceflight.esa.int/docs/Factsheets/29%20Orbital%20Cygnus%20LR.pdf

[11] "MEV-1 (Mission Extension Vehicle-1) and MEV-2." [Online]. Available: https://directory.eoportal.org/web/eoportal/satellite-missions/m/mev-1

[12] "ISS Utilization: SPHERES (Synchronized Position Hold Engage Reorient Experiment Satellites)." [Online]. Available: https://earth.esa.int/web/eoportal/satellite-missions/i/iss-spheres

[13] "Project Gemini Familiarization Manual," McDonnell Aircraft Corporation, Tech. Rep., 1966. [Online]. Available: https://www.ibiblio.org/apollo/Documents/GeminiManualVol2.pdf

[14] J. G. Cook, V. Aksamentov, T. Hoffman, and W. Bruner, "ISS Interface Mechanisms and their Heritage," 2011. [Online]. Available: https://ntrs.nasa.gov/citations/20110010964

[15] D. S. F. Portree, "Mir hardware heritage," National Aeronautics and Space Administration, 1995. [Online]. Available: https://history.nasa.gov/SP-4225/documentation/mhh/mirheritage.pdf

[16] "Apollo Operations Handbook: Block II Spacecraft," National Aeronautics and Space Administration, Tech. Rep., 1969. [Online]. Available: https://www.hq.nasa.gov/alsj/SM2A-03-BK-II-%281%29.pdf

[17] "Apollo-Soyuz Test Project: Information for Press," 1975. [Online]. Available: http://www.ibiblio.org/apollo/Documents/ASTP2.pdf

[18] "International Docking System Standard (IDSS): Interface Definition Document (IDD) ," International Space Station Multilateral Control Board, Tech. Rep., 2016. [Online]. Available: https://www.internationaldockingstandard.com/download/IDSS_IDD_Revision_E_TAGGED.pdf

[19] J. L. Lewis, "NASA Docking System (NDS) Technical Integration Meeting," November 2010. [Online]. Available: https://ntrs.nasa.gov/citations/20110005478

[20] "International Docking Standard Image Galley," 2017. [Online]. Available: https://internationaldockingstandard.com/gallery.html

[21] E. McKenna, "AAReST Spacecraft Electron-magnetic Docking System," Master's thesis, University of Surrey, 2015.

[22] G. Ritter, A. Hays, G. Wassick, G. Sypitkowski, C. Nardell, P. Tchory, and J. Pavlich, *Autonomous satellite docking system*, 2001. [Online]. Available: https://arc.aiaa.org/doi/abs/10.2514/6.2001-4527

[23] A. Boesso and A. Francesconi, "ARCADE small-scale docking mechanism for micro-satellites," *Acta Astronautica*, vol. 86, pp. 77–87, 2013. [Online]. Available: https://www.sciencedirect.com/science/article/pii/S0094576513000180

[24] M. Barbetta, A. Boesso, F. Branz, A. Carron, L. Olivier, J. Prendin, G. Rodeghiero, F. Sansone, L. Savioli, F. Spinello, and A. Francesconi, "ARCADE-R2 experiment on board BEXUS 17 stratospheric balloon," *CEAS Space Journal*, vol. 7, pp. 347–358. [Online]. Available: https://link.springer.com/article/10.1007/s12567-015-0083-3?utm_source=getftr&utm_medium=getftr&utm_campaign=getftr_pilot#citeas

[25] L. Olivieri and A. Francesconi, "Design and test of a semiandrogynous docking mechanism for small satellites," *Acta Astronautica*, vol. 122, pp. 219–230, 2016. [Online]. Available: https://www.sciencedirect.com/science/article/pii/S0094576516000515

[26] L. Rodgers, N. Hoff, E. Jordan, M. Heiman, and D. W. Miller, "A Universal Interface for Modular Spacecraft," 2005.

[27] D. Miller, A. Saenz-Otero, J. Wertz, A. Chen, G. Berkowski, C. Brodel, S. Carlson, D. Carpenter, S. Chen, S. Cheng, D. Feller, S. Jackson, B. Pitts, F. Perez, J. Szuminski, and S. Sell, "Spheres: a testbed for long duration satellite formation flying in micro-gravity conditions," *Advances in the Astronautical Sciences*, vol. 105, 01 2000.

[28] J. Bowen, A. Tsuda, J. Abel, and M. Villa, "Cubesat proximity operations demonstration (cpod) mission update," in *2015 IEEE Aerospace Conference*, 2015, pp. 1–8.

[29] J. Lee, "Monocular vision based pose estimation of rendezvous and docking for autonomous assembly of a reconfigurable space telescope (aarest)," Master's thesis, Unversity of Surrey, 2016.

[30] F. Sansone, F. Branz, and A. Francesconi, "A relative navigation sensor for cubesats based on led fiducial markers," *Acta Astronautica*, vol. 146, pp. 206–215, 2018. [Online]. Available: https://www.sciencedirect.com/science/article/pii/S0094576517312109

[31] B. Chen, J. Cao, A. Parra, and T.-J. Chin, "Satellite pose estimation with deep landmark regression and nonlinear pose refinement," 2019.

[32] M. Kisantal, S. Sharma, T. H. Park, D. Izzo, M. Martens, and S. D'Amico, "Satellite pose estimation challenge: Dataset, competition design, and results," *IEEE Transactions on Aerospace and Electronic Systems*, vol. 56, no. 5, pp. 4083–4098, 2020.

[33] J. Kelsey, J. Byrne, M. Cosgrove, S. Seereeram, and R. Mehra, "Vision-based relative pose estimation for autonomous rendezvous and docking," in *2006 IEEE Aerospace Conference*, 2006, pp. 20 pp.–.

[34] *NVIDIA Jetson Nano System-on-Module Datasheet*, NVIDIA, 2020.

[35] *NVIDIA Jetson Nano Developer Kit Carrier Board Specification*, NVIDIA, 2020.

[36] "Jetson nano developer kit," NVIDIA. [Online]. Available: https://developer.nvidia.com/embedded/jetson-nano-developer-kit

[37] *LS R976 Chip LED 0805*, OSRAM Opto Semiconductors, 2021.

[38] D. Scaramuzza, "OCamCalib: Omnidirectional Camera Calibration Toolbox for Matlab," 2021. [Online]. Available: https://sites.google.com/site/scarabotix/ocamcalib-omnidirectional-camera-calibration-toolbox-for-matlab

[39] C. Pirat, F. Ankersen, R. Walker, and V. Gass, "Vision based navigation for autonomous cooperative docking of cubesats," *Acta Astronautica*, vol. 146, pp. 418–434, 2018. [Online]. Available: https://www.sciencedirect.com/science/article/pii/S0094576517309086

[40] A. O. Erlank, "Development of cubestar, a cubesat- compatible star tracker," Master's thesis, Stellenbosch University, 2013.

[41] A. O. Erlank and W. H. Steyn, "Arcminute attitude estimation for cubesats with a novel nano star tracker," *IFAC Proceedings Volumes*, vol. 47, no. 3, pp. 9679–9684, 2014, 19th IFAC World Congress. [Online]. Available: https://www.sciencedirect.com/science/article/pii/S1474667016431459

[42] *1270VS SERIES SINGLE-AXIS RATE TABLE*, Ideal Aerosmith. [Online]. Available: http://www.ideal-aerosmith.com/downloads/docs/1270VS_Series_Data_Sheet.pdf

[43] W. Slater, N. Tiwari, T. Lovelly, and J. Mee, "Total ionizing dose radiation testing of nvidia jetson nano gpus," 09 2020, pp. 1–3.

[44] "Telos obc," Orb Astro, 2021. [Online]. Available: https://orbastro.com/subsystems/telos-obc/

[45] A. Merstallinger, M. Sales, E. Semerad, and B. Dunn, "Assessment of cold welding between separable contact surfaces due to impact and fretting under vacuum," *ESA Scientific and Technical Memoranda*, 11 2009.